UNIVERSIDADE FEDERAL DO RIO GRANDE DO SUL

CENTRO DE BIOTECNOLOGIA

PROGRAMA DE PÓS-GRADUAÇÃO EM BIOLOGIA CELULAR E MOLECULAR

# Sociobiologia de *Cryptococcus* spp.: de comunidades estruturadas à dinâmica de populações

WILLIAM LOPES

Tese submetida ao Programa de Pós-Graduação em Biologia Celular e Molecular do Centro de Biotecnologia da Universidade Federal do Rio Grande do Sul como requisito parcial para obtenção do título de Doutor em Ciências.

Orientadora: Profa. Dra. Marilene Henning Vainstein

Co-orientador: Prof. Dr. Kildare Rocha de Miranda

Porto Alegre, agosto de 2021

CIP - Catalogação na Publicação

Lopes, William
Sociobiologia de Cryptococcus spp.: de comunidades estruturadas à dinâmica de populações / William Lopes. -- 2021.
122 f.
Orientadora: Marilene Henning Vainstein.

Coorientadora: Kildare Rocha Miranda.

Tese (Doutorado) -- Universidade Federal do Rio Grande do Sul, Centro de Biotecnologia do Estado do Rio Grande do Sul, Programa de Pós-Graduação em Biologia Celular e Molecular, Porto Alegre, BR-RS, 2021.

1. Interações microbianas. I. Vainstein, Marilene Henning, orient. II. Miranda, Kildare Rocha, coorient. III. Título.

Elaborada pelo Sistema de Geração Automática de Ficha Catalográfica da UFRGS com os dados fornecidos pelo(a) autor(a).

Este trabalho foi desenvolvido no Laboratório de Fungos de Importância Médica e Biotecnológica, situado no Centro de Biotecnologia da Universidade Federaldo Rio Grande do Sul, e no Gore Laboratory: Ecological Systems Biology, situado no Department of Physics do Massachusetts Institute of Technology. Este trabalho contou com fomento do Conselho Nacional de Desenvolvimento Científico e Tecnológico (CNPq) e da Coordenação de Aperfeiçoamento de Pessoal de Nível Superior (CAPES).

# AGRADECIMENTOS

Esta é uma seção popular em qualquer tese; não há regras em relação à estrutura. Sendo assim, quero expressar meus agradecimentos de forma pessoal e clara, como se o estivesse fazendo presencialmente a todas as pessoas que foram fundamentais ao longo desses quatro anos.

À minha orientadora *Marilene Vainstein*, que me proporcionou uma formação fundamentada no amplo exercício da liberdade de pensar, questionar e experimentalmente testar as minhas hipóteses. Princípios que são fundamentais na formação de um cientista independente. Obrigado por abraçar comigo as minhas aspirações de carreira e iluminá-las com sábios conselhos e orientação.

Ao *Jeff Gore*, do GoreLab – Physics of Living Systems do MIT pela orientação que recebi e por lapidar meus interesses e minha visão sobre ciência; além de proporcionar um ambiente multidisciplinar com vasto amparo intelectual, acolhimento e amizade. Também agradeço aos colegas e amigos: *Simon Lax*, *Martina Dal Bello*, *Anthony Ortiz*, e em especial *Daniel Amor*, por tornarem o meu trabalho e estudo em uma fantástica experiência.

Ao *Kildare Miranda*, do Centro Nacional de Biologia Estrutural e Bioimagem da UFRJ pelas discussões e por possibilitar o início do meu contato com

microscopia. Estendo os agradecimentos às amigas *Rachel Rachid* e *Marcia Attias*, excelentes e inspiradoras microscopistas.

Ao *Augusto Schrank* – resumir agradecimentos a alguém que reúne múltiplos valores admiráveis requer mais habilidade do que sintetizar ideias complexas em uma curta conclusão. O *Augusto* é o último nível da empatia. Fonte de inspiração. *Cheers*, meu amigo.

Aos amigos que se tornaram membros da minha família: *Rafael Schneider* e *Diego Ricci*. Obrigado pelos ouvidos, sábios conselhos e incentivo. Vida longa e larga.

Ao *Lestat Ali*, meu namorado e pesquisador favorito. Obrigado pela dedicação incondicional e por tantos ensinamentos. Dividir a vida contigo é ter uma vida completa.

Aos meus pais: *Elizete Neli Lopes* e *José Francisco Lopes*. O infinito amor de vocês é constante provisão de força e perseverança na minha vida. Desejo para mim os mesmos valores e princípios que vejo em vocês. Obrigado por tudo. Amo vocês.

# SUMÁRIO

# LISTA DE ABREVIATURAS

**AN** – Fossa Nasal Anterior, do inglês, *Anterior Nares*

**ASL** – Líquido de Superfície das Vias Aéreas, do inglês, *Airway Surface Liquid*

**CF** – Fibrose Cística, do inglês, *Cystic Fibrosis*

**ECM** – Matriz Extracelular, do inglês, *Extracellular Matrix*

**GXM** – Glucuronoxilomanana, do inglês, *Glucuroxylomannan*

**NF** – Nasofaringe, do inglês, *Nasopharynx*

**RMpH** – Modulação Relativa de pH, do inglês, *Relative Modulation of pH*

**RY** – Rendimento Relativo, do inglês, *Relative Yield*

**SEM** – Microsopia Eletrônica de Varredura, do inglês, *Scanning Electron Microscopy*

**URT** – Trato Respiratório Superior, do inglês, *Upper Respiratory Tract*

# LISTA DE FIGURAS

# RESUMO

Microrganismos podem alternar comportamentos individual e coletivo em resposta a interações positivas ou negativas. Em patógenos, muitas dessas interações influenciam importantes determinantes de virulência, como: formação de biofilme, plasticidade fenotípica e secreção de metabólitos tóxicos. Esta tese explora as interações do patógeno humano *Cryptococcus* spp. por meio de quatro estudos, cada um evidenciando aspectos complementares em sociobiologia. O estudo (*i*) demonstrou que a organização geométrica das células na etapa inicial da formação de biofilme é um requisito importante para o desenvolvimento de ultraestrutura madura. Em (*ii*) diferentes morfotipos capsulares foram identificados e classificados por modelos computacionais. O estudo (*iii*) abordou as interações interespecíficas entre *Cryptococcus neoformans* e a bactéria *Serratia marcescens.* Nessa competição, um interessante padrão foi observado: a bactéria migrou em direção ao fungo impactando a viabilidade celular e determinantes de virulência de *C. neoformans*. Em (*iv*) as interações inter-reinos de *C. neoformans* foram estudadas em um nível maior de complexidade: uma comunidade composta por 8 microrganismos relevantes no trato respiratório foi utilizada para explorar a dinâmica e montagem de populações. Os resultados demonstraram a existência de estados alternativos de equilíbrio dominados por importantes patógenos, bem como os mecanismos que governam essas comunidades.

## ABSTRACT

Microorganisms modulate their behavior both individually and collectively in response to interactions with other microorganisms. For pathogens in particular, such interactions influence key virulence factors such as biofilm formation, phenotypic plasticity, and toxin secretion. This thesis explores the interactions of the human pathogen *Cryptococcus* spp. in four studies, each focusing on a complementary aspect of microbial sociobiology**.** The first study (*i*) demonstrated that the geometric organization of cells in the initial step of biofilm formation is an important requirement for the development of mature ultrastructures. In the second study (*ii*), different capsular morphotypes were identified and classified by computational modeling. The third study (*iii*) focused on the interspecies interactions between *Cryptococcus neoformans* and the bacteria *Serratia marcescens*. An interesting phenomenon was observed in those competitions: the bacteria consistently migrated toward the fungus, impacting the latter's viability and virulence factors. Finally, in study (*iv*), the cross– kingdom interactions of *C. neoformans* were examined at a higher degree of complexity: a set of eight microorganisms relevant to the respiratory tract, including *C. neoformans*, was used to investigate population dynamics and community assembly. The results revealed the existence of alternative stable states dominated by important pathogens, in addition to the mechanisms that govern such communities.

# 1 INTRODUÇÃO

## 1.1 Sociomicrobiologia

As interações microbianas emergem em múltiplas escalas de complexidade, e por consequência o sucesso da colonização demonstra padrões sociais de cooperação. A ideia de microrganismos exercendo sociabilidade pode ser recebida com desconfiança, no entanto colaborações interdisciplinares têm aprofundado experimentalmente as evidências de comportamento social em microrganismos, tanto na natureza quanto no hospedeiro[1]. Quanto ao conceito, um comportamento é social quando há consequências para ambos os componentes da interação[1, 2]. Nessa perspectiva, até mesmo uma população clonal pode demonstrar padrões sociais. Essa constatação é observada quando o consumo de nutrientes pela comunidade afeta o desenvolvimento individual; levando à emergência de competições por exploração como resposta à escassez de recursos[3]. Há também interações intraespecíficas que são positivas; a comunidade pode cooperar para modificar o seu entorno quando as condições são adversas[4]. No eixo da microbiologia integrativa, autores têm demonstrado que além dos microrganismos serem sociais, eles também enfrentam dilemas na tomada de decisões[5] e manifestam padrões de estratégia evolutiva em seus comportamentos[6]. Algumas dessas estratégias já foram caracterizadas molecularmente[7, 8].

Populações clonais podem apresentar variabilidade fenotípica. No laboratório essas variações são evidenciadas em experimentos simples, como a medição de células cultivadas em diferentes condições ambientais ou até mesmo a variabilidade observada entre diferentes replicatas da mesma condição. Alguns estudos demonstram que a estocasticidade na expressão gênica pode resultar em múltiplos fenótipos em uma mesma população clonal [9, 10]. As principais vantagens adaptativas que emergem dessa heterogeneidade estão usualmente associadas a estratégias de sobrevivência da população, como: (*i*) resposta à incerteza, quando populações apresentam diferentes fenótipos para garantir sua propagação caso o ambiente mude inesperadamente. Essa estratégia inclui microrganismos cuja população é composta por *persisters* ou fenótipos dormentes. Dessa forma, a chance de sobrevivência é maior caso a população sofra um estresse catastrófico[11]; (*ii*) divisão de trabalho, demonstrado em *Salmonella typhimurium* em que subpopulações fenotipicamente diferentes atuam em conjunto durante a infecção e aumentam o sucesso de colonização[12-14].

**1.2 Comunidades microbianas estruturadas**

Microrganismos podem formar estruturas multicelulares funcionais, como biofilmes. Comunidades estruturadas na forma de biofilme são revestidas por uma matriz extracelular de composição diversa. Em bactérias e leveduras as principais

etapas da formação de biofilme incluem: (1) adesão inicial, (2) colonização da superfície, (3) formação de microcolônias, (4) maturação e (5) dispersão (Figura 1).

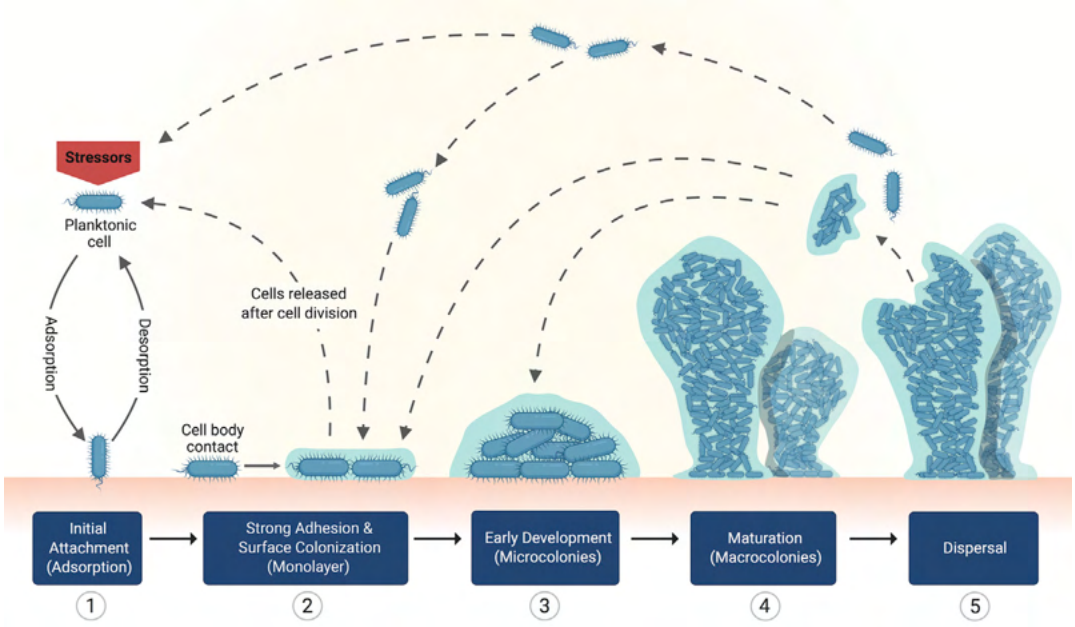


**Figura 1**| Representação geral da formação de biofilme. Essa representação abrange a maior parte dos microrganismos, porém, múltiplos processos podem acontecer ao mesmo tempo e alguns deles podem ser marcados por particularidades de uma espécie, como a ultraestrutura na fase de maturação[15].

A matriz do biofilme apresenta duas funções principais: proteção contra agentes antimicrobianos e estratificação dos microrganismos em processos de divisão de trabalho e colaboração social[16-19]. A ultraestrutura observada em biofilmes resulta das interações dentro da comunidade[20, 21]. Um exemplo é a presença de canais bem definidos em biofilme de *Bacillus subtilis* que fornecem um sistema para transporte líquido e regulação de térmica (Figura 2).

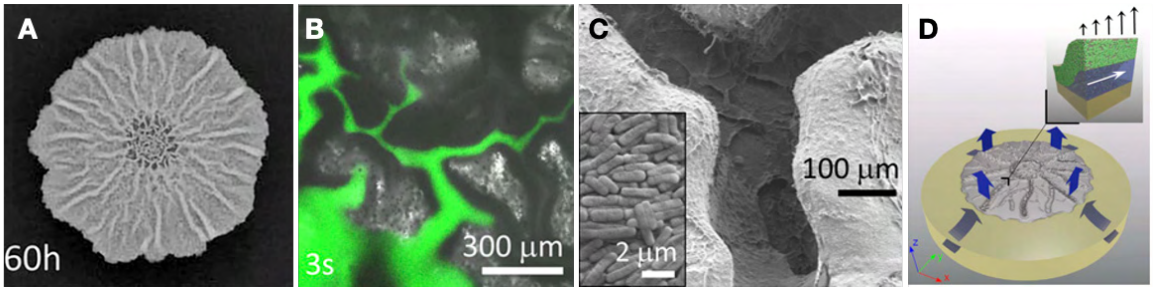


**Figura 2**| Caracterização de canais em biofilme de *B. subtilis*. (A) Biofilme de *B. subtilis* em meio sólido após 60 h. (B) Imagens de microscopia após micro–injeção de marcador fluorescente nos canais do biofilme. (C) Microscopia eletrônica de varredura. (D) Ilustração da evaporação que ocorre na superfície do biofilme e promove regulação térmica. Modificado de Wilking, *et al*.[22]

### 1.3 Dinâmica de comunidades

O nível mais complexo das interações microbianas ocorre na microbiota de um hospedeiro, onde as comunidades que estão em equilíbrio passam a integrar o ambiente de forma funcional[23]. Essa associação é evidenciada no trato respiratório; interações interespecíficas positivas e negativas promovem resistência à colonização por patógenos[24]. Há concretas evidências de que alterações na microbiota resultam em uma variedade de doenças [25]. Dessa forma, a caracterização das interações microbianas é fundamental para entender como ocorre a regulação estrutural de uma comunidade e os fatores que podem impactar a sua resiliência.

A dinâmica de comunidades microbianas pode ser determinada laboratorialmente através de experimentos em microcosmos: ambientes controlados que mimetizam propriedades importantes de um sistema. Uma das estratégias é iniciar pela unidade fundamental das interações interespecíficas, os pares de microrganismos[26]. Nessa abordagem cada espécie em um par compete

duas vezes: como residente (maior abundância relativa, por ex. 95%) ou invasor (~5%). As competições são propagadas até que o estado de equilíbrio seja atingido, ou seja, não ocorram flutuações nas abundâncias relativas. Os regimes em equilíbrio podem ser três: exclusão competitiva se o vencedor não depender da abundância inicial; coexistência se ambas as espécies forem detectadas no estado de equilíbrio; ou bistabilidade se o vencedor da competição for o microrganismo em maior abundância inicial, possibilitando que o sistema apresente dois estados alternativos de equilíbrio [27] (Figura 3).

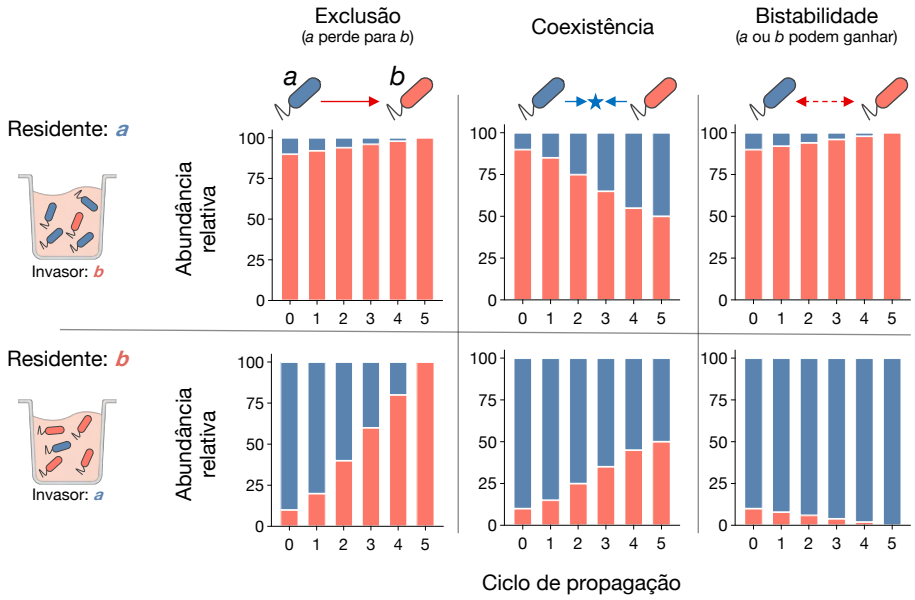


**Figura 3**| Regimes de interações microbianas. Cada microrganismo em um par é competido duas vezes: como residente (maior abundância relativa) ou invasor. Os co-cultivos são propagados até o equilíbrio para determinação da abundância relativa final. Os regimes podem ser três: (A) exclusão, se vencedor não depender da abundância inicial; (B) coexistência entre as duas espécies independentemente da abundância inicial e (C) Bistabilidade, em que dois estados alternativos de equilíbrio podem ser atingidos dependendo da abundância inicial de cada espécie.

Após avaliar todos os regimes possíveis, as interações entre pares podem ser combinadas para construir uma rede que permite extrair dados quantitativos, fazer predições estruturais e entender a dinâmica de comunidades mais complexas. A predição de comunidades a partir de competições em pares de espécies pode ser realizada com uma precisão de até 90%[28]. Essa predição apresenta limitações quando as espécies apresentam bistabilidade ou dependem de sua densidade populacional para melhor desempenho (efeito Allee)[29].

### 1.4 Modelo de estudo: *Cryptococcus* spp.

Durante os avanços acerca do microbioma, as comunidades fúngicas receberam pouca atenção em comparação às comunidades bacterianas[30]. Existe atualmente o entendimento de que as interações bacterianas–fúngicas têm efeitos importantes sobre a saúde humana, ainda que pouco exploradas[31-34]. A maior parte dos estudos, utilizando *Candida albicans*, têm mostrado uma miríade de mecanismos que impactam a virulência e sobrevivência desse modelo em comunidades microbianas mistas[35, 36]. Relativamente poucos estudos têm explorado interações entre bactérias e *Cryptococcus* spp., e até esse momento a dinâmica dessas interações em comunidades complexas não foi descrita[37].

As leveduras *Cryptococcus neoformans* e *Cryptococcus gattii* são os agentes etiológicos criptococose (Figura 4). A infecção ocorre após a inalação e posterior tráfego do fungo pela cavidade nasal seguida de deposição no trato respiratório,

onde pode causar pneumonia. Dependendo do estado imunológico do hospedeiro, a levedura se dissemina até o sistema nervoso central onde frequentemente causa meningoencefalite, manifestação mais grave da doença que geralmente ocasiona o óbito[38, 39]. A criptococose se destaca com uma incidência estimada de 230.000 casos por ano com cerca de 80% de letalidade em regiões onde o tratamento é escasso[40]. Interessantemente, há evidências de que variações fenotípicas em isolados de *Cryptococcus* spp. estão relacionadas com o progresso da doença[41].

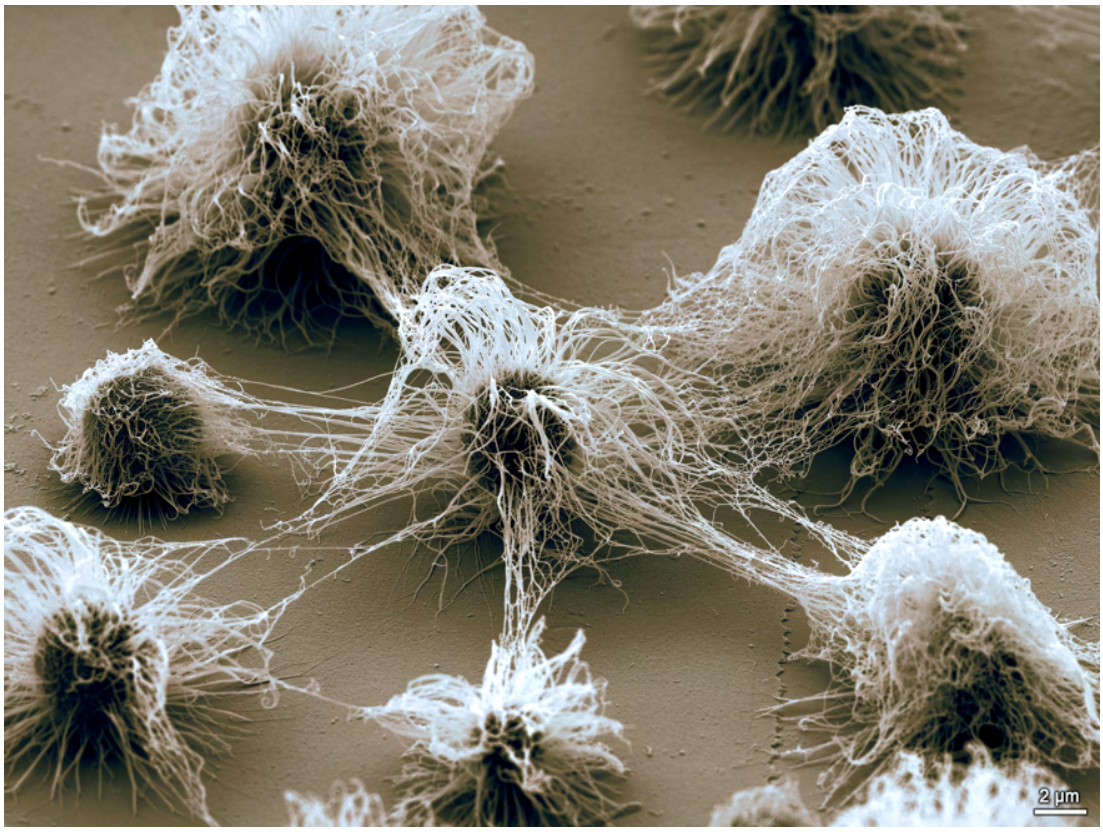


**Figura 4**|Imagem de microscopia eletrônica de varredura de isolado clínico de *Cryptococcus gattii.* Destaca-se a presença da cápsula polissacarídica do fungo em disposição geométrica com as células adjacentes.

A formação de biofilme por *C. neoformans* vem sendo frequentemente relatada em dispositivos médicos, incluindo: cateteres ventriculares utilizados para aliviar a pressão intracraniana em casos de meningite[42-44], fístulas para hemodiálise[45], válvulas cardíacas artificiais[46] e prótese de quadril[47, 48]. Além disso, foi demonstrado que criptococomas são estruturas semelhantes a biofilmes, revestidos por polissacarídeos[49].

Casos de co-infecção em humanos já foram descritos entre *C. neoformans* e bactérias, incluindo *Klebsiella pneumoniae* e *Streptococcus pneumoniae.* Em alguns casos a abordagem terapêutica padrão para tratamento da criptococococose foi menos eficaz e as infecções apresentaram sítios de infecção diferentes dos esperados na patogênese da criptococose [50-54].

Nesse contexto, *C. neoformans* é um modelo importante para estudar a amplitude das interações que ocorrem em comunidades formadas por indivíduos da mesma espécie e comunidades mistas, incluindo: (*i*) ultraestrutura e dinâmica de formação de biofilme; (*ii*) detecção de diversidade morfológica em população clonal; (*iii*) interação competitiva entre bactéria e fungo e, (*iv*) regulação e montagem de comunidades do trato respiratório.

# 2 OBJETIVOS

A presente tese teve por objetivo explorar as interações populacionais de *Cryptococcus* spp., a fim de avaliar padrões associados à sociobiologia em comunidades clonais e mistas.

## 2.1 Objetivos específicos

– Explorar a organização ultraestrutural e geométrica de biofilmes formados por *Cryptococcus* spp.

– Utilizar *machine learning* na detecção de populações morfologicamente diferentes.

– Explorar o espectro de interação entre *Cryptococcus* e bactérias ambientais, com ênfase em interações competitivas.

– Elucidar a dinâmica populacional de *Cryptococcus* e bactérias presentes na cavidade nasal e identificar parâmetros de regulação da estrutura de comunidades clinicamente relevantes.

# 3 RESULTADOS

Os resultados desta tese estão distribuídos em quatro capítulos.

**3.1 Capítulo I:** Geometrical Distribution of *Cryptococcus neoformans* Mediates Flower–Like Biofilm Development.

Publicado na Frontiers in Microbiology, 2017.

frontiers in Microbiology

ORIGINAL RESEARCH
published: 19 December 2017
doi: 10.3389/fmicb.2017.02534

# Geometrical Distribution of *Cryptococcus neoformans* Mediates Flower-Like Biofilm Development

*William Lopes[1†], Mendeli H. Vainstein[2,3†], Glauber R. De Sousa Araujo[4], Susana Frases[4], Charley C. Staats[1], Rita M. C. de Almeida[2,5], Augusto Schrank[1], Lívia Kmetzsch[1] and Marilene H. Vainstein[1*]*

[1] Centro de Biotecnologia, Universidade Federal do Rio Grande do Sul, Porto Alegre, Brazil, [2] Departamento de Física, Instituto de Física, Universidade Federal do Rio Grande do Sul, Porto Alegre, Brazil, [3] Physics of Living Systems, Department of Physics, Massachusetts Institute of Technology, Cambridge, MA, United States, [4] Instituto de Biofísica Carlos Chagas Filho, Universidade Federal do Rio de Janeiro, Rio de Janeiro, Brazil, [5] Instituto Nacional de Ciência e Tecnologia – Sistemas Complexos, Universidade Federal do Rio Grande do Sul, Porto Alegre, Brazil

Microbial biofilms are highly structured and dynamic communities in which phenotypic diversification allows microorganisms to adapt to different environments under distinct conditions. The environmentally ubiquitous pathogen *Cryptococcus neoformans* colonizes many niches of the human body and implanted medical devices in the form of biofilms, an important virulence factor. A new approach was used to characterize the underlying geometrical distribution of *C. neoformans* cells during the adhesion stage of biofilm formation. Geometrical aspects of adhered cells were calculated from the Delaunay triangulation and Voronoi diagram obtained from scanning electron microscopy images (SEM). A correlation between increased biofilm formation and higher ordering of the underlying cell distribution was found. Mature biofilm aggregates were analyzed by applying an adapted protocol developed for ultrastructure visualization of cryptococcal cells by SEM. Flower-like clusters consisting of cells embedded in a dense layer of extracellular matrix were observed as well as distinct levels of spatial organization: adhered cells, clusters of cells and community of clusters. The results add insights into yeast motility during the dispersion stage of biofilm formation. This study highlights the importance of cellular organization for biofilm growth and presents a novel application of the geometrical method of analysis.

**Keywords: biofilm, cryptococcus, scanning electron microscopy, geometrical, fungi**

OPEN ACCESS

***Edited by:***
*Joshua D. Nosanchuk, Albert Einstein College of Medicine, United States*

***Reviewed by:***
*Erin E. McClelland, Middle Tennessee State University, United States*
*Helene Eisenman, Baruch College (CUNY), United States*

***Correspondence:**
*Marilene H. Vainstein*
*mhv@cbiot.ufrgs.br*

[†] *These authors have contributed equally to this work.*

***Specialty section:***
*This article was submitted to Fungi and Their Interactions, a section of the journal Frontiers in Microbiology*

***Received:*** *14 October 2017*
***Accepted:*** *06 December 2017*
***Published:*** *19 December 2017*

***Citation:***
*Lopes W, Vainstein MH, De Sousa Araujo GR, Frases S, Staats CC, de Almeida RMC, Schrank A, Kmetzsch L and Vainstein MH (2017) Geometrical Distribution of Cryptococcus neoformans Mediates Flower-Like Biofilm Development. Front. Microbiol. 8:2534. doi: 10.3389/fmicb.2017.02534*

## INTRODUCTION

Microorganisms have been traditionally analyzed using planktonic microbial cells; however, this lifestyle is not necessarily related with the growth of microbes in their most prevalent habitat. Recent approaches in confocal microscopy and molecular biology have provided evidence that biofilm formation represents the most common mode of microbial growth in nature (Costerton et al., 1995; Jabra-Rizk et al., 2004; Ramage et al., 2009; Martinez and Casadevall, 2015) and is a response to ecological competition in the environment (Oliveira et al., 2015). A wide range of microorganisms are able to switch from a planktonic to a colonial lifestyle in the form of a biofilm, creating aggregated communities that are enclosed by an extracellular matrix (ECM) (Costerton et al., 1995).

Microbial biofilms are now recognized as highly structured and dynamic communities, in which phenotypic diversification allows microorganisms to adapt to diverse environments under different conditions (Watnick and Kolter, 2000; Parsek and Fuqua, 2004; Drescher et al., 2016; Gulati and Nobile, 2016; Sheppard and Howell, 2016). Importantly, biofilms can be composed of thousands of cells encased in a matrix and attached to a surface, but they can also contain as few as tens of cells arranged as small clusters or aggregates (Stacy et al., 2016). Open channels interspersing the microcolonies allow water and nutrients to reach their interior and contribute to the nutrition and formation of mature biofilms, possibly mimicking a primitive circulatory system. Waste products might also be removed through this system (Flemming and Wingender, 2010).

Cells growing within biofilms exhibit unique phenotypic features compared to their planktonic counterparts, with the increased resistance to antimicrobial agents provided by biofilms being the more drastic example (Martinez and Casadevall, 2006a; Clatworthy et al., 2007; Lewis, 2008; Ramage et al., 2009). Biofilm formation in the environment and in the host can be induced by sub-lethal concentrations of antibiotics or secondary metabolites, respectively (Kumar and Ting, 2013; Oliveira et al., 2015). In this context, biofilm formation is an important feature of *Cryptococcus neoformans* because it is an environmentally ubiquitous fungal pathogen that causes cryptococcosis, a lethal disease with a worldwide distribution related to bioclimatic conditions as well as to soil characteristics and land use (Cogliati et al., 2017). Almost 200,000 deaths per year are estimated to be due to cryptococcal meningitis (Rajasingham et al., 2017). The major virulence factor of this fungus is the polysaccharide capsule that surrounds the cell wall and is responsible for fungal attachment to surfaces and subsequent biofilm formation (Martinez et al., 2010; de S Araújo et al., 2016). The *C. neoformans* capsule is composed mainly of glucuronoxylomannan (GXM), a polysaccharide generated intracellularly and exported to the extracellular space via vesicle-mediate secretion (Rodrigues et al., 2007). GXM is also a constituent of the cryptococcal biofilm ECM (Martinez and Casadevall, 2005; Park et al., 2009).

*C. neoforman*s can form biofilms on medical devices, including ventriculoatrial shunt catheters (used to manage intracranial hypertension), peritoneal dialysis fistulae, cardiac valves and prosthetic joints (Walsh et al., 1986; Braun et al., 1994; Banerjee et al., 1997; Johannsson and Callaghan, 2009; Shah et al., 2015). On biotic surfaces, after traversing the blood brain barrier in meningoencephalitis, *C. neoformans* has the ability to form biofilm-like structures known as cryptococcomas (Aslanyan et al., 2017).

Although previous studies using confocal microscopy provided initial insights into cryptococcal biofilm structure, conventional scanning electron microscopy (SEM) techniques do not preserve the mature biofilm ultrastructure (Martinez and Casadevall, 2005, 2007). The highly hydrated matrix is greatly deformed and the cell samples undergo distortion and may present artifacts. Also, *C. neoformans* capsule is sensitive to dehydration and is easily disrupted during routine sample preparation (Edwards et al., 1967; Sakaguchi, 1993). As a consequence, considerable effort is currently being spent on the development of new methods and instrumentation for its visualization. By applying an adapted protocol for SEM, we characterized the underlying geometrical structure of cell distribution during biofilm formation. The degree of order was numerically quantified and we revealed a correlation between higher levels of biofilm formation and more ordered underlying structures. Order/disorder are very relevant in physical systems. In crystals, for example, deformations can only occur near defects due to the high energetic cost of their occurrence elsewhere. Besides, some phase transitions are defect mediated. Moreover, in the last decades the interplay among defects, geometry and statistical physics has been highlighted (Nelson, 2002). Here we propose the application of parameters designed to measure order in physical systems (Nelson and Halperin, 1979; Aeppli and Bruinsma, 1984; Okabe et al., 2000; Bernard and Krauth, 2011; Borba et al., 2013) to the microbial populations. We also investigated the details of the ultrastructural organization of cryptococcal biofilms and show that cryptococcal cells aggregate with a specific ordered structure favoring biofilm formation as compared to disorganized conglomerates.

## MATERIALS AND METHODS

### Microorganisms

*C. neoformans* var. *neoformans* B3501 strain, serotype D (ATCC 34873), is a strong biofilm former on different surfaces (Martinez and Casadevall, 2005). This serotype has an increased risk of infections for patients with skin lesions (Dromer et al., 1996). *C. neoformans* var. *grubii* strain H99 serotype A (ATCC 208821) is responsible for the vast majority of central nervous system infections, particularly in HIV infected patients. The acapsular *cap67* mutant was obtained by chemical mutagenesis of B3501 (Fromtling et al., 1982). *C. neoformans* var. *grubii* strain H99 was employed as a recipient for creating the *grasp* hypocapsular mutant involved in unconventional protein secretion (Kmetzsch et al., 2011). All of the strains were kept frozen in glycerol and subcultured at the time of the experiment. Standard biosecurity safety procedures been carried out according to our institution guidelines (www.cbiot.ufrgs.br/index.php/manual/).

### Quantification of *Cryptococcus neoformans* Biofilm Formation by XTT

Cells were grown for 24 h at 30°C, in 25 ml of *Sabouraud* broth media in a rotary shaker at 150 rpm. Then, the cells were collected by centrifugation at 3,000 g for 5 min, washed three times with phosphate-buffered saline pH 7.2 (PBS), counted using a hemacytometer and suspended at $10^7$ cells/ml in DMEM—Dubelcco's modified eagle media high glucose (GIBCO, USA) at pH 7.4. After that, 500 μl of the suspension were added into individual wells of polystyrene 24-well plates (Greiner Bio-One, AUS) containing sterile glass coverslips and incubated at 37°C for 48 h. Following incubation, wells were washed in triplicate with PBS to remove any planktonic cells. Then, 300 μl of XTT salt solution (1 mg/ml in PBS) and 24 μl of menadione solution (1 mM in acetone; Sigma-Aldrich) were added to each well. Microtiter plates were incubated at 37°C for 5 h. Mitochondrial dehydrogenases in live cells reduce XTT

tetrazolium salt to XTT formazan, resulting in a colorimetric change, which was measured in a microtiter reader at 492 nm (SpectraMax i3). Microtiter wells containing only culture media but no *C. neoformans* cells were used as negative controls.

## Scanning Electron Microscopy Preparation

An improved protocol developed for visualization of *C. neoformans* planktonic cells by electron microscopy was recently described (de S Araújo et al., 2016). Here, we modified a few parameters in order to preserve the ultrastructure of the biofilm stages. Briefly, after the incubation period (4 h for adhesion or 48 h for mature biofilm) as previously described, the wells containing the coverslips were washed three times with PBS. After washing, cryptococcal adhered cells were fixed with 500 µl of 2.5% glutaraldehyde type 1 (Sigma Aldrich, USA) diluted in 0.1 M sodium cacodylate buffer pH 7.2 and for 15 min at room temperature. Then, the wells were washed three times in 0.1 M sodium cacodylate buffer pH 7.2 containing 0.2 M sucrose and 2 mM $MgCl_2$ with the aid of two pipettors, which were used for addition and concurrent removal to avoid air exposure. Adhered cells were dehydrated in a series of freshly made solutions of graded ethanol (30, 50 and 70%, for 5 min/step, then 95% and twice 100%, for 10 min/step). The dehydration was closely monitored to prevent biofilm matrix and capsule polysaccharide extraction. Samples were then subjected to critical point drying (EM CPD 300, Leica) immediately after dehydration, mounted on metallic stubs, sputter-coated with a 15–20 nm gold-palladium layer and visualized in a scanning electron microscope (Carl Zeiss EVO® MA10 or EVO® −50 HV Carl, Oberkochen, Germany), operating at 10 kV. Microscopic fields were selected by random scanning and photo documented. The experiment was performed in three independent replicates.

## Time-Lapse Microscopy

*C. neoformans* B3501 cells were prepared as described above and suspended at $10^6$ cells/ml in DMEM. After that, 1 ml of the suspension was added into individual wells of glass and incubated for 4 h at 37°C. Following incubation, wells were washed in triplicate with PBS to remove planktonic cells. Then, 1 ml of DMEM was replaced and the wells incubated for 48 h at 37°C on an Espectral FV 1000 system. Time-lapse imaging was performed at 30–60 s intervals.

## Geometric Analysis

The strains were allowed to grow for 4 h (adhesion stage) in the conditions described above. Following the incubation, the wells were washed three times and prepared for SEM. Images were treated with the software ImageJ (version1.48k, Java 1.8.0_65 (64-bit); National Institutes of Health, USA, [http://imagej.nih.gov/ij]) to extract information for further statistical analysis. An ellipse was fitted to each of the particles in the image and its area was calculated. Since only the center coordinates of each ellipse are necessary for the analysis of the neighboring cells network, we represent particles with circles of fixed radius such that their areas are equal to the average ellipse area. Once the centers are defined, it is possible to establish the nearest neighbors of each cell $n_i$ by means of a Delaunay triangulation and Voronoi tessellation using Fortune's algorithm (Fortune, 1987) with the software voronoi (version 1, Steve J. Fortune, Bell Laboratories, USA [http://ect.bell-labs.com/who/sjf/voronoi.tar]) With this information, it is possible to obtain the number of nearest neighbors and distance distributions, allowing one to calculate average parameters that quantify order in the spatial distribution of cells for each sample image.

To calculate the local variance in the number of neighbors $\mu_2^i$, first the average number of neighbors was calculated for the sample

$$n = \langle n_i \rangle = \frac{1}{N}\sum_{i=1}^{N} n_i, \tag{1}$$

where $N$ is the number of cells whose distance to any image border is not within 5% of the system size. Cells close to the border were not taken into account to calculate bulk properties. The local variance was defined as

$$\mu_2^i = (n_i - n)^2, \tag{2}$$

and the global variance was defined as its average

$$\mu_2 = \mu_2^i = \frac{1}{N}\sum_{i=1}^{N} \mu_2^i. \tag{3}$$

Following Borba et al. (2013) we calculate the local order parameter

$$\psi_6^i = \frac{1}{n_i}\sum_{j=1}^{n_i} cos\left(6\theta_{ijk}\right), \tag{4}$$

where $\theta_{ijk}$ are the angles formed by the two line segments joining site $i$ and two of its consecutive neighbors (**Figure 1**). A given set of points (an image) can then be characterized by the average value of this quantity

$$\psi_6 = \langle \psi_6^i \rangle = \frac{1}{N}\sum_{i=1}^{N} \psi_6^i. \tag{5}$$

For a triangular lattice of points, every site will have $\psi_6^i = 1$, since every site has six neighbors and six angles equal to 60°. Therefore, $\psi_6 = 1$ characterizes a perfect hexagonal symmetry (Borba et al., 2013). On the other hand, for a set of randomly distributed points, a value of $\psi_6$ close to 0 is expected.

In order to analyze the probability of generating a given value of $\psi_6$ from a random distribution of points, we generated 1,000 sets of randomly distributed non-overlapping disks with areas equal to the average area of a cell in a box of the same size as that of the image. For such an ensemble with $N_e$ images (sets of points), one can calculate the average of $\psi_6$ and its standard deviation. Then, it is possible to apply a Student-$t$ test to evaluate the possibility that the values of $\psi_6$ for experimental configurations of cells present the same distribution as those for a random configuration generated by the deposition of non-overlapping disks. The one-tailed test for samples with unequal variance was calculated using LibreOffice (version 4.2.8.2 Build

ID: 420m0 (Build: 2); LibreOffice, The Document Foundation, [http://www.libreoffice.org]). The $p$-values of the test were obtained for the 3 pairs of data: (a) 5 samples of B3501 with 1,000 sets of non-overlapping disks ($p \approx 3.7 \times 10^{-7}$); (b) 5 samples of H99 with 1,000 sets of non-overlapping disks ($p \approx 0.35$); (c) 5 samples of B3501 with 5 samples of H99 ($p \approx 1.1 \times 10^{-6}$). In Figure S1 we show the corresponding network for a set of randomly distributed non-overlapping disks and the distribution of $\psi_6$ for 1,000 random sets.

# RESULTS

## Biofilm Formation and Analysis of Cellular Adhesion Geometry

To characterize the underlying geometric structure of cell distribution in the initial steps of biofilm formation (after incubation for 4 h), SEM images were examined. This analysis considered the wild type strains *C. neoformans* B3501 and H99, the hypocapsular *grasp* mutant (Kmetzsch et al., 2011) and the acapsular *cap67* mutant (Fromtling et al., 1982). To take into account differences in adhesion of the cells to the substrate, we analyzed conditions differing only in the presence or not of poly-L-lysine (PLL). Pre-treatment with PLL increases the number of adhered cells, as expected, but did not influence the cell organization (**Figure 2**).

To classify the spatial distribution of cells, we used four measures: average number of nearest neighbors $n$ and its variance $\mu_2$, intercellular distances, and the average degree of hexagonal order $\psi_6$. This last measure has been applied to study the liquid-hexatic transition (Nelson and Halperin, 1979; Bernard and Krauth, 2011) and also to the study of nanoporous alumina arrays in which case the ordering and organization are crucial for engineering applications (Borba et al., 2013). Among the

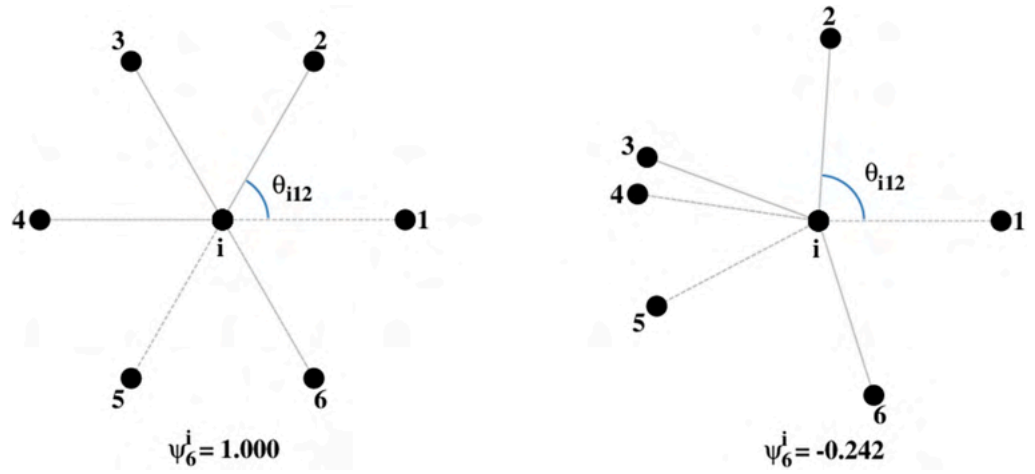


**FIGURE 1 |** Values of $\psi_6^i$ for a site in a triangular lattice (**left**) and for a random distribution of neighbors (**right**).

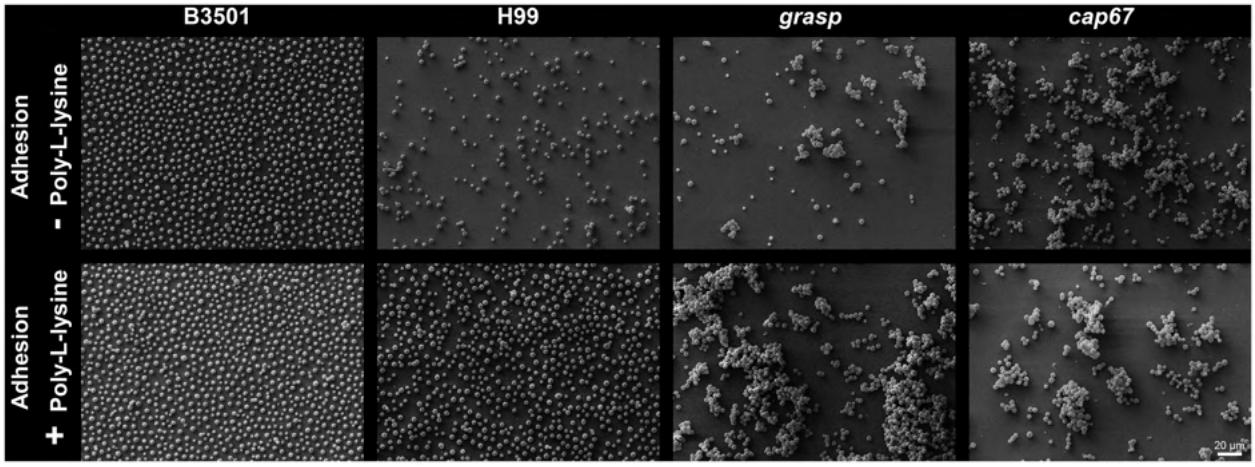


**FIGURE 2 |** Geometric distribution of cells in the initial steps of biofilm formation, after incubation for 4 h. *C. neoformans* B3501, H99, hypocapsular *grasp* mutant and acapsular *cap67* mutant strains adhered in non-covered glass coverslips **(Top)** and PLL covered glass coverslips **(Bottom)**.

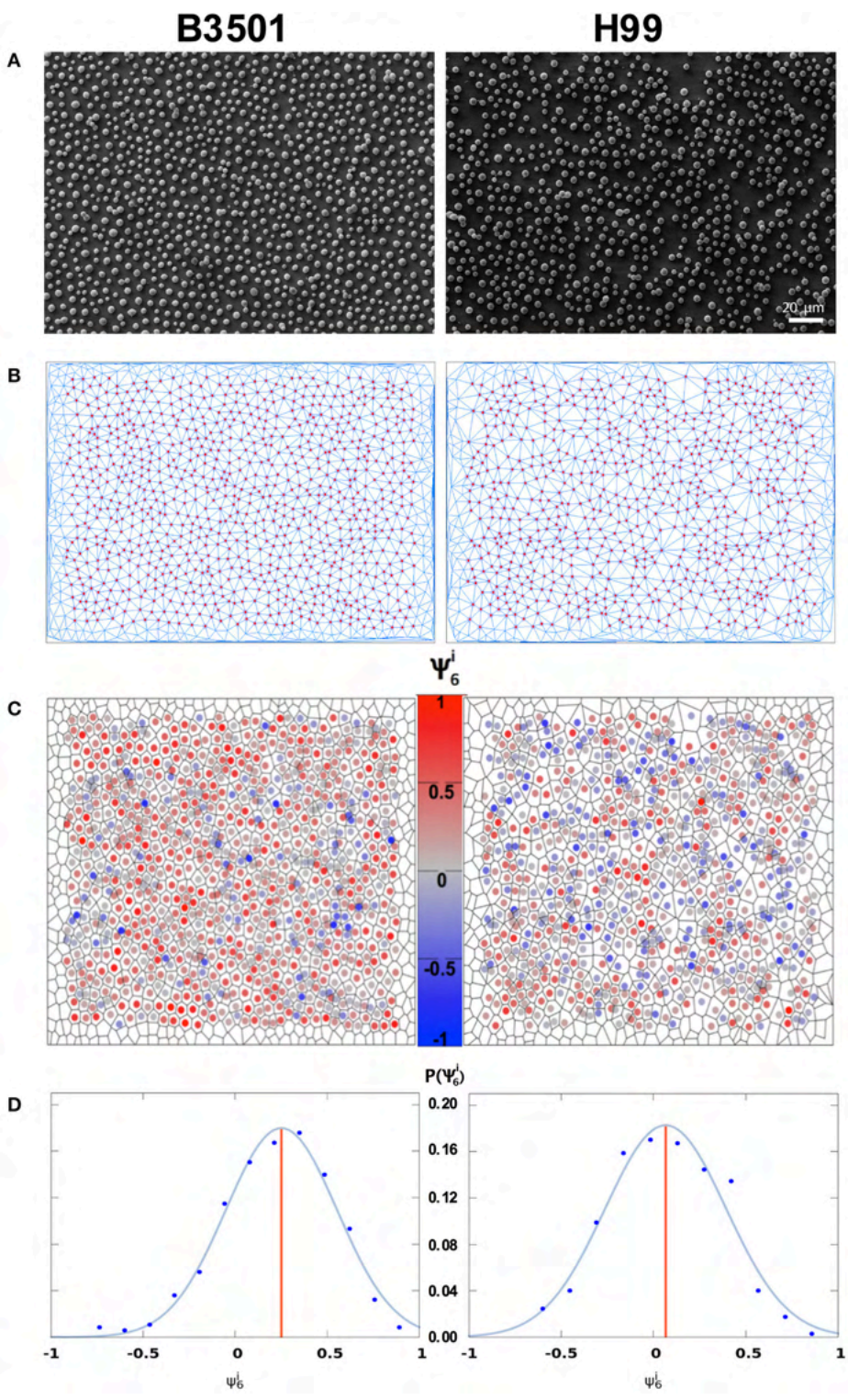


**FIGURE 3 |** Analysis of the local order parameter, $\psi_6^i$, for samples with poly-L-lysine. Left column *C. neoformans* B3501. Right column *C. neoformans* H99. **(A)** SEM image of cryptococcal cells after 4 h of adhesion. **(B)** Network of adhered cells; nearest neighbors were obtained by Delaunay triangulation (blue line segments). Red circles represent cell centers in the bulk of the sample. Vertices without circles near the borders represent cells that were discarded from the analysis (distance to the border within 5% of system size) to minimize border effects. **(C)** Voronoi diagram of the sample. The color code represents $\psi_6^i$. **(D)** Distribution of $\psi_6^i$. The blue curve is a Gaussian fit to the data points, grouped into bins. The red vertical line displays the average value $\psi_6$ of the local order parameter $\psi_6^i$ (Left: $\psi_6 = 0.22$, total number of cells in the image $N_{tot} = 1066$, number of analyzed cells $N = 837$, average number of neighbors $n = 6.01$. Right: $\psi_6 = 0.06$, $N_{tot} = 885, N = 699, n = 6.01$).

parameters used, $\psi_6$ was the one with more conclusive results (Table S1).

The variance of the number of nearest neighbors $\mu_2$ (Equation 2) was found to be low, in the range 0.7–2.1, indicating that the majority of cells have a number of nearest neighbors very close or equal to the average $n = 6$ (see Figure S2 for the local values $\mu_2^i$). This fact reinforces that it is adequate to use $\psi_6$, a measure appropriate for hexagonal symmetry. For its quantification, we first measure the local order parameter $\psi_6^i$ (Equation 4), that indicates how isotropically arranged the nearest neighbors of the i$^{th}$ cell are. If the cells are found in a perfect triangular lattice, all sites have six nearest neighbors and the lines joining the i$^{th}$ cell with two of its consecutive neighbors form an angle of 60°. In this case of perfect hexagonal symmetry, the average of $\psi_6^i$ over the whole sample will attain its maximum value $\psi_6 = 1$. For a random distribution of cells, with angles differing from one another, the local values $\psi_6^i$ will be smaller and their average, $\psi_6$, will be negative and close to zero (**Figure 1**). In the case of partial ordering, one finds intermediate values $0 < \psi_6 < 1$. In **Figures 3A,B**, we present the Delaunay triangulation (Okabe et al., 2000), that determines the network of nearest neighbors, combined with SEM of the adhesion stage of biofilm formation with PLL biofunctionalization for B3501 and H99 (wild types). Acapsular *cap67* mutant and hypocapsular *grasp* mutant were not analyzed since they organize in 3D aggregates.

In **Figure 3C**, cell color is related to $\psi_6^i$. It also shows the Voronoi diagram (Okabe et al., 2000), which separates the figure into polygons such that every point in a polygon is closer to the cell inside it than to any other cell. The distribution of $\psi_6^i$ for each image is presented in **Figure 3D** with a Gaussian fit to the data. The red vertical line represents the average value $\psi_6$.

The quantification of biofilm formed after 48 h of incubation was based on 2,3-bis(2-methoxy-4-nitro-5-sulfophenyl)-5-[(phenylamino)carbonyl]-2H-tetrazolium-hydroxide (XTT) reduction assay measurements which determines the absorbance ($A_{(492\ nm)}$) of metabolic activity and correlates with biofilm formation and fungal cell number. We found a correlation ($r^2 = 0.98$, **Figure 4**) between higher levels of biofilm formation [$A_{(492\ nm)}$] and more orderly underlying structures $< \psi_6 >$, where the angled brackets represent an average over 5 images in the early phase of biofilm formation, since the first layer of cells on a substrate is not necessarily characteristic of a random deposition. For instance, *C. neoformans* strain B3501, known as a strong biofilm producer has $< \psi_6 > = 0.20$ and $A_{(492\ nm)} = 1.38$, while strain H99, a weak biofilm producer, has $< \psi_6 > = -0.04$ and $A_{(492\ nm)} = 0.44$ without PLL (**Figure 5**).

Special attention should be given to these two strains in the presence of PLL; the better-known biofilm producer B3501 has a significantly more orderly disposal than H99, with an approximately equal number of cells (**Figure 2**). These results endorse that the difference in biofilm formation is not due simply to different numbers of cells due to the low adhesion of H99 in the absence of PLL. For both mutants *cap67* and *grasp*, it was not possible to calculate $\psi_6$ due to the formation of cell

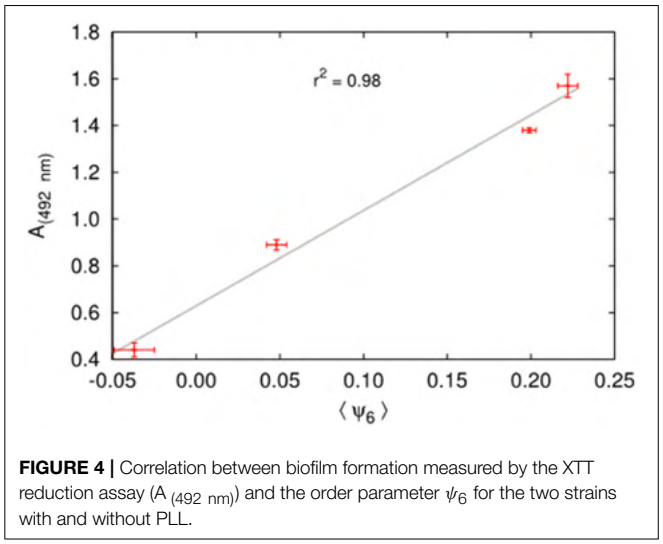


**FIGURE 4 |** Correlation between biofilm formation measured by the XTT reduction assay ($A_{(492\ nm)}$) and the order parameter $\psi_6$ for the two strains with and without PLL.

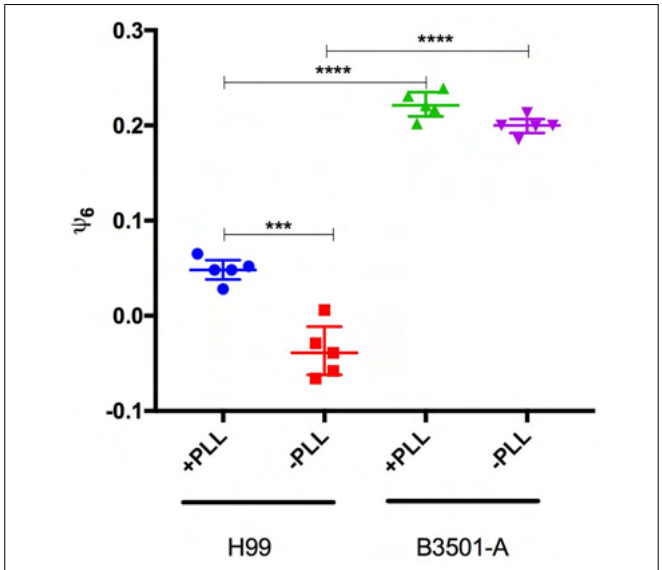


**FIGURE 5 |** Poly-L-lysin influence on $\psi_6$ is strain dependent. $\psi_6$ is determined for five independent images of *C. neoformans* H99 and B3501 incubated in plates treated or not with Poly-L-Lysin. Data is presented as symbols and are also represented by the Median and inter-quartile ranges. Statistically significant differences were marked (***$p < 0.001$; ****$p < 0.0001$) according to ANOVA test followed by Tukeys multiple comparison test.

**TABLE 1 |** Values of $\psi_6$ for 5 samples of each of the strains B3501 and H99 (without PLL).

| Biological replicate | $\psi_6$ values of *C. neoformans* strains | |
|---|---|---|
| | B3501 | H99 |
| 1 | 0.213 | −0.058 |
| 2 | 0.200 | −0.029 |
| 3 | 0.200 | −0.058 |
| 4 | 0.185 | −0.039 |
| 5 | 0.199 | 0.006 |

agglomerates that result in 3D structures. Nevertheless, this does not weaken the conclusion that a non-random disposal with a regular distance and number of neighbors between cells is important for biofilm formation, given that the cells are closely packed together in these agglomerates.

High values of $\psi_6$ for *C. neoformans* B3501 in the range 0.18–0.21 (without PLL, Table S1) for the 5 biological replicates analyzed are indeed representative of a non-random distribution since a Student-*t* test to evaluate the possibility that such values arise from a random deposition of non-overlapping disks with the same average area as the cells yields a *p*-value $p \approx 3.7 \times 10^{-7}$ (Figure S1). For the five samples of *C. neoformans* H99, we obtained $p \approx 0.35$ when comparing its $\psi_6$ values to those of the randomly deposited non-overlapping disks. The same test applied comparing *C. neoformans* B3501 with *C. neoformans* H99 yielded $p \approx 1.1 \times 10^{-6}$. Therefore, it is plausible to conclude that the *C. neoformans* H99 samples present an essentially random distribution, whereas *C. neoformans* B3501 do not (**Table 1**).

The orderly distribution of cells even during the detachment stage of biofilm is a process that occurs dynamically (**Figure 6**, Movie S1). From the snapshots, it can be seen that new cells that flow into the already populated region do so by following almost the same paths and tend to maintain a more or less regular distance from other cells. This suggests that the ordering stems from some interaction between the cells: this behavior is similar to equally charged spheres (not in electrolyte solutions), which tend to auto-organize due to the electrical repulsion among themselves (**Figure 5**). The nature of such interaction, however, remains a point of further investigation (since the typical distance between the cells is considerably larger than the Debye length of an electrolyte solution as the cellular medium). On the other hand, our results also suggest that this effective repulsion may depend on the capsule integrity since both mutants with capsular defects tend to agglomerate into compact clusters of cells.

## *C. neoformans* Biofilms Are Organized in Flower-Like Clusters

We believe that the organized geometrical structure is an important factor for the next steps of biofilm formation. The strain B3501 was used for ultrastructure analysis of biofilm due to its significantly more orderly disposal during adhesion stage (**Figure 2**) and strong biofilm formation (Martinez and Casadevall, 2007). The applied protocol allowed the detailed observation of preserved cryptococcal biofilms by SEM. Our findings contrast with available data of confocal and optical microscopy in which resolution and detail are limited, but converge in biofilm thickness in the range of 50–76 μm, as well its complexity (Martinez and Casadevall, 2006a,b, 2007; Robertson and Casadevall, 2009). The images showed the ECM embedding cells organized into biofilm clusters with both amorphous and organized flower-like structures of the mature

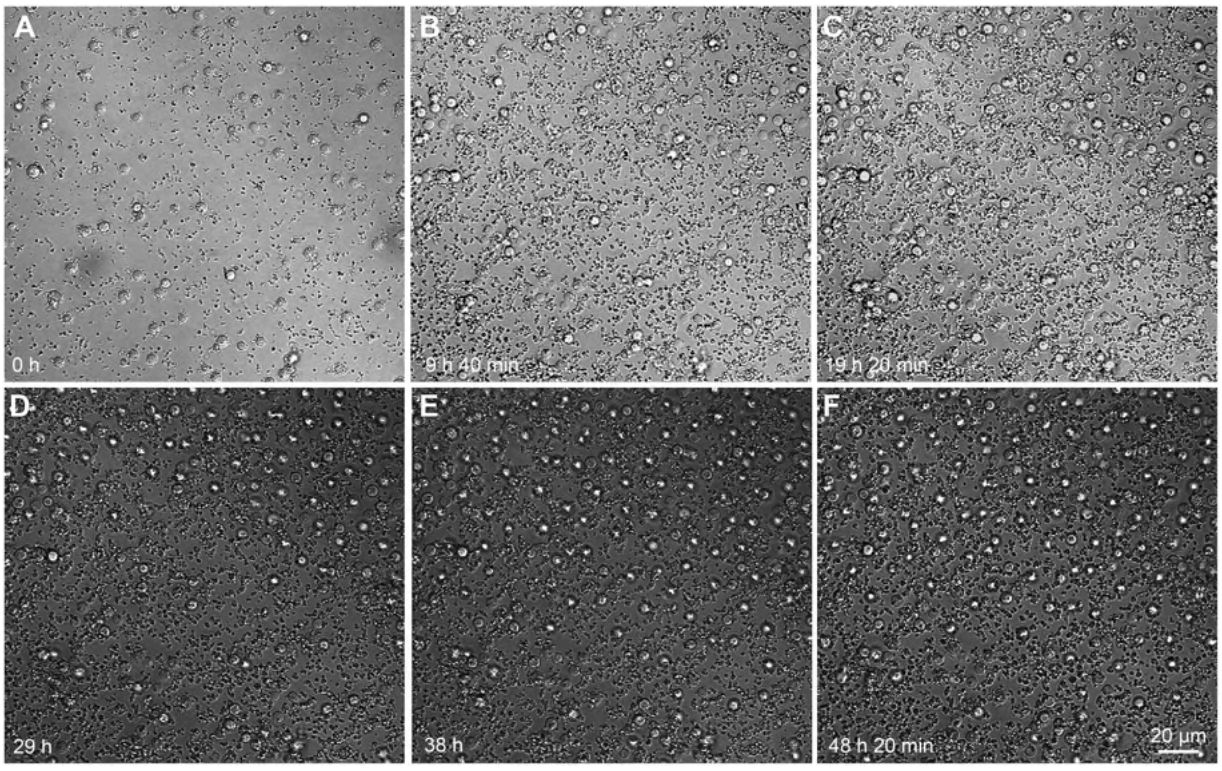


**FIGURE 6 |** Time-lapse microscopy of *C. neoformans* B3501 flow during various stages of biofilm formation. Initial steps of biofilm formation **(A–C)**. From 24 h onwards, cells enter the vision field from the top **(D)** and auto-organize **(E–F)**. Cells tend to follow similar trajectories. Snapshots from the Movie S1.

biofilm (**Figures 7A–D**). The vertical growth seems to dominate cluster expansion with regions of high ECM densities. Isolated yeast cells were found both attached to the surface and cluster-associated (**Figures 7A,C,D**).

Interestingly, an unexpected phenotype of a few cells located at cluster boundaries, resembling bridges and involved in anchoring the clusters, can be observed. These cells are elongated and interconnect surface substrate and clusters (**Figures 8A–C**). We found ECM micro channels displaying a well-designed structure associated with cryptococcal cells (**Figure 8D**). For some soil bacteria, the presence of ECM micro channels are required for cell alignment and advancement on surfaces (Berleman et al., 2016).

## Cryptococcal Biofilms Form a Social Community of Clusters

Even within a community composed of genetically identical microbial cells, there exists high heterogeneity in morphology and physiology of its sub-populations (Lidstrom and Konopka, 2010). Wang et al. (2013), discovered that *C. neoformans* responds in a paracrine manner to a secreted protein responsible for colony communication and morphology (Wang et al., 2013).

To synchronize social microbial behavior, extracellular signals must disseminate across the community and reach adjacent cells. Here, we speculate the existence of a hierarchical biofilm organization composed of a cluster community. The SEM images show that small clusters (**Figures 9B–D**) are adjacent to the mature biofilm cluster (**Figure 9A**). We hypothesize that a feedback response of mature clusters signaling leads to the formation of small aggregates surrounded by ECM. The clustering process may implement a secondary signaling for functional or phenotypic switch in a paracrine manner, as supported by Wang et al. (2013). This process seems to trigger an autoinducer activity by stimulating neighboring cells to phenocopy the mature cluster.

# DISCUSSION

The hallmarks of this study were the use of a numerical measure to quantify the geometrical order of the first layer of adhered cells in the process of biofilm formation as well as the detection of well-shaped ultrastructure of *C. neoformans* biofilms. To verify the relation between cellular order and biofilm production, we analyzed *C. neoformans* H99 and the mutants *grasp* and *cap67*, and the usual model *C. neoformans* B3501. Once we showed that there is indeed a correlation between increased order and increased biofilm production, we focused on the standard strain to further study the ultrastructure.

This analysis was made possible by the introduction of a modified protocol for SEM visualization of microbial biofilms,

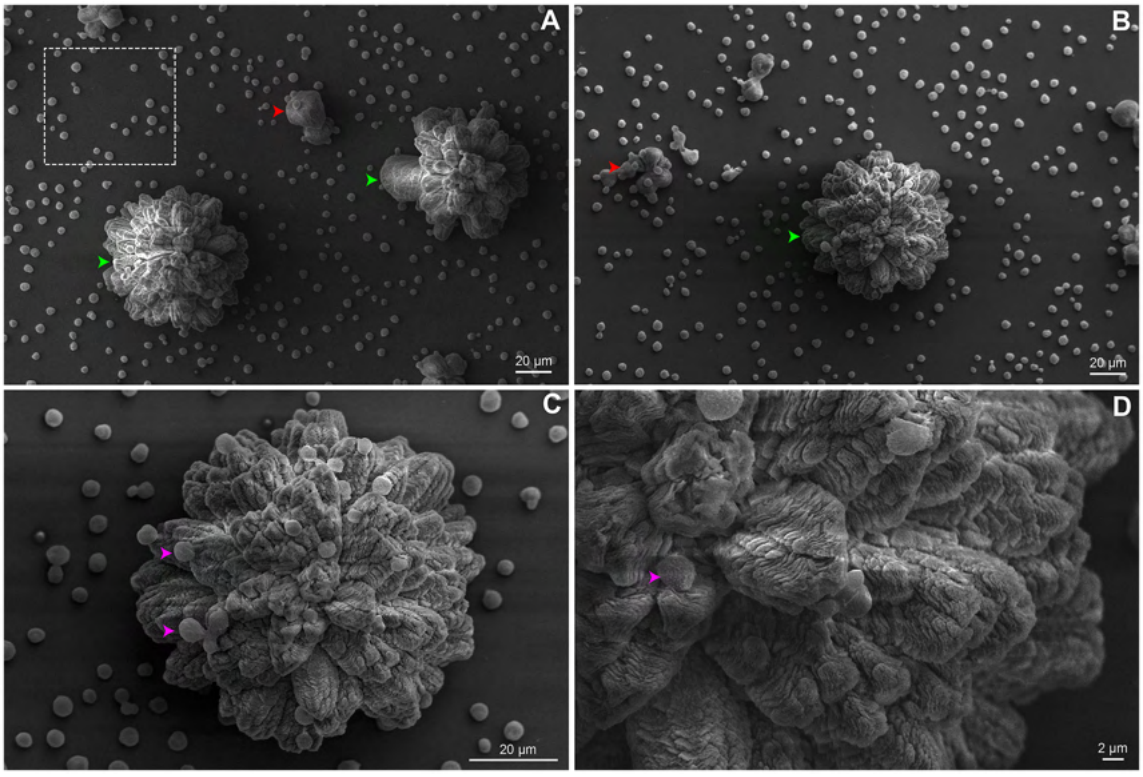


**FIGURE 7 |** SEM of *C. neoformans* B3501 displaying flower-like clusters. Biofilm presented complex structure and spatial organization. **(A)** The dotted square indicates cryptococcal cells attached to the surface. **(A,B)** Biofilm clusters with amorphous and asymmetrical structure (red arrows) and mature biofilm with flower-like shapes (green arrows). Flower-like cluster shown in higher magnification **(C,D)** with embedded cells in the ECM (pink arrows).

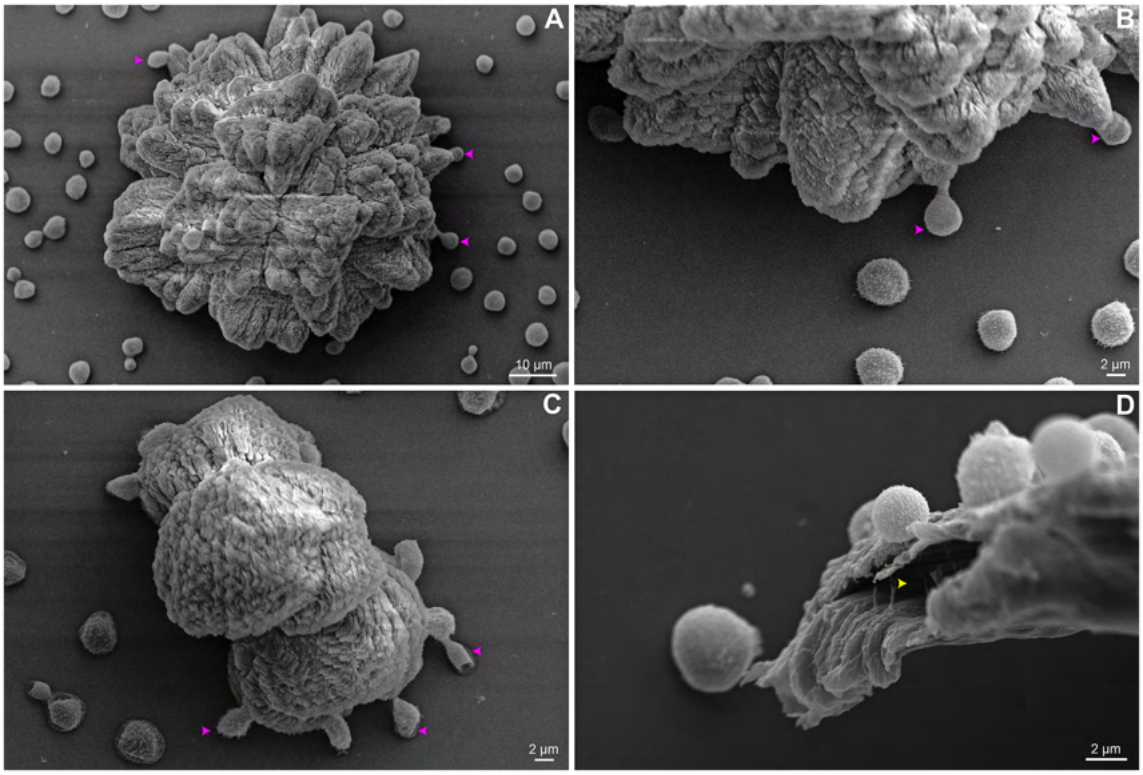


**FIGURE 8 |** SEM of *C. neoformans* B3501 showing phenotypic cell change and biofilm channel. Anchoring cells (pink arrows) are observed located at the base of some flower-like **(A,B)** and amorphous **(C)** clusters boundaries. Micro channels (yellow arrow) are found associated with cells **(D)**.

due to the fact that standard protocols greatly distort the matrix. To minimize artifacts, a shortened time of fixation and careful dehydration is optimal for ultrastructural SEM analysis (Joubert et al., 2015). The ultrastructure preservation was achieved by combining appropriated techniques, a reduced period of incubation during SEM preparation and good grade reagents.

Distinct levels of spatial organization were observed: adhered cells, clusters of cells, as well as the community of clusters. The affinity of attachment to different surfaces is strongly related to the presence of the cryptococcal capsule. In fixed *C. neoformans* cells, the fibers surrounding the cell (capsule filaments) directly stretch and link cells to surface, promoting attachment (de S Araújo et al., 2016).

Cryptococcal biofilm formation seems to be driven by a communication system via adhesion/matrix protein signaling (Wang et al., 2013) and directional proliferation of the original adhered cells. Cfl1, the first prominent ECM secreted protein of *C. neoformans*, is highly expressed in subpopulations located at the periphery of a mating community and is concentrated in the extracellular matrix boundary. This protein orchestrates yeast-hypha morphotype transition, cell adhesion, and virulence. This suggests that Cfl1 possibly serves as a signal regulating morphotype transition in the cells enclosed or adjacent to the ECM (Wang et al., 2012, 2013; Wang and Lin, 2015).

We hypothesize that the reversible cell attachment is mediated by capsule interactions and the orderly distribution of cells, as described above. As the capsule is primarily responsible for the high negative zeta potential of *C. neoformans* cells, variations in the structure of GXM could also influence the Zeta potential. However, zeta potential determinations of *C. neoformans* H99 and B3501 strains did not reveal major differences (Kozel and Gotschlich, 1982; Nosanchuk and Casadevall, 1997; Cordero et al., 2011). In this way, we assume that biofilm formation capability is a serotype-dependent process and is influenced by either biological or environmental factors. Based on this, the resulting patterns observed for H99 and B3501 strains cannot be explained by charge distribution. The ordering reported is due to an effective repulsion among cells, the nature of which remains a mystery. It may be due to chemical sensing or excluded volume that hinders the free motion of cells (Movie S1), in which cells flow following similar paths and tend to adhere at an approximately constant distance from one another.

Our data supports that once irreversible attachment occurs, cryptococcal cells may form a narrow ECM layer around the cell body where cells rapidly proliferate, but the surface-attached and peripheral anchored cryptococcal cells may restrict their expansion to the plane. As initial small clusters proliferate, their shape increasingly becomes anisotropic. At this point, the biofilm consists of several layers of cells grouped into clusters resembling extremely organized flower-like patterns. After maturation, cells may detach as microcolonies or as isolated

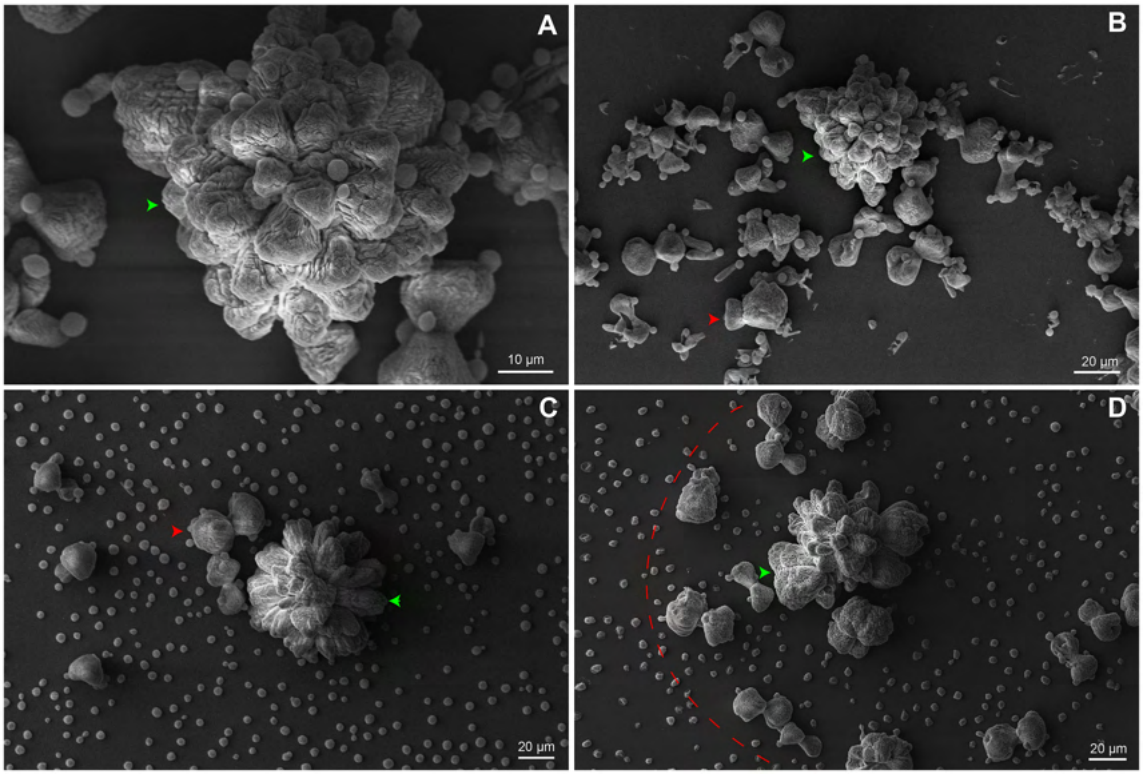


**FIGURE 9 |** SEM of *C. neoformans* B3501 organized in a community of clusters. **(A)** Higher magnification image of a mature biofilm. **(B–D)** Small amorphous clusters (red arrows and dotted arc) surround the mature biofilm (green arrow).

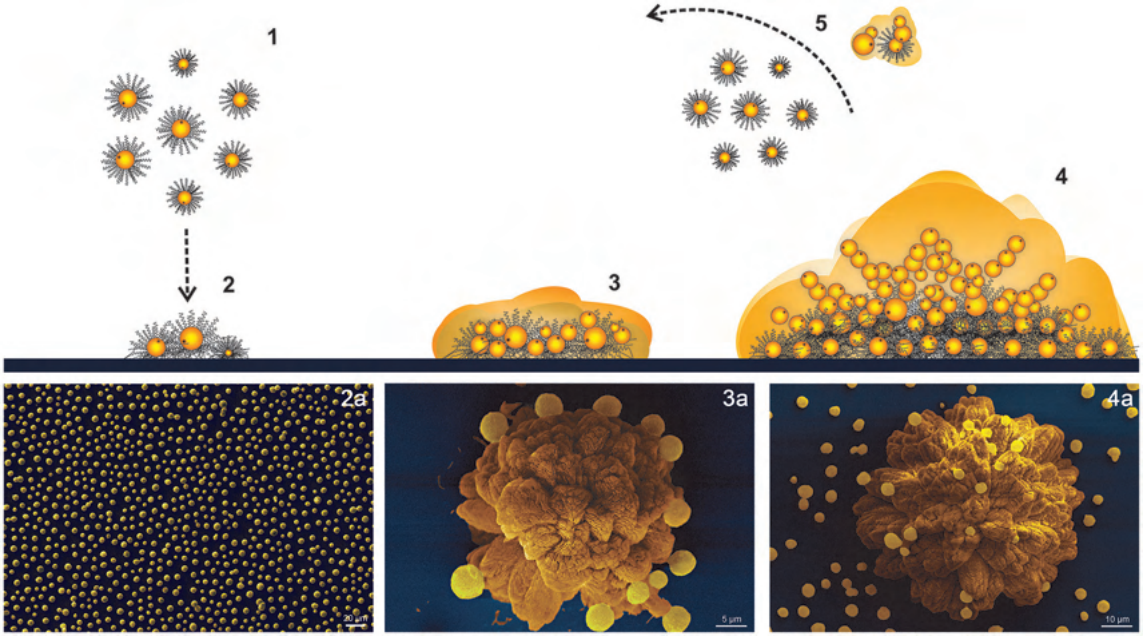


**FIGURE 10 |** Scheme of *C. neoformans* B3501 biofilm formation. (1,2) Adhesion of planktonic cells follows an approximately hexagonal distribution. (3) Cluster expansion and shaping. (4) Flower-like mature biofilm. (5) Detachment of microcolonies or planktonic cells. (a) SEM of biofilm development stages.

planktonic cells, which auto-organize following an approximately hexagonal distribution. Cells tend to follow similar trajectories and may initiate the process again (**Figure 10** and Movie S1).

Yan et al. (2016) discovered that the cluster ultrastructure of *Vibrio cholerae* biofilm results from the combination of expansion and confinement of surface-attached cells that generates an effective anisotropic stress. Such stress overpowers the cell-to-surface adhesion force for cells at the cluster center, causing these cells to realign in the vertical direction and forcing the transition from 2D expansion to 3D growth (Yan et al., 2016). Moreover, if selection pressure is high, it has been shown that clusters of *Pseudomonas aeruginosa* have higher fitness than isolated cells because cells at the top of the clusters have better access to nutrients (Kragh et al., 2016). Cluster morphogenesis results from a great number of variables capable of shaping the ultrastructure. Physical and demographic processes are demonstrated to act as key factors in biofilm architectures (Hödl et al., 2014). Cryptococcal cells are likely most susceptible to the hydrodynamics constraints due to low motility. In contrast, more motile microorganisms may escape these constraints and develop biofilm morphogenesis related to cellular migration and biofilm coalescence (Hödl et al., 2014).

Mathematical studies have related that biofilm architecture depends on the availability of nutrients, carbon and oxygen, uptake processes linked to hydrodynamics and diffusion limitation of substrate transport through the biofilm. More generally, metabolic capabilities, genotypic and phenotypic adaptations could result in different behaviors within the biofilm, allowing organisms to choose between a number of strategies (Klapper and Szomolay, 2011; Klapper, 2012).

Interestingly, for *V. cholerae* the presence of low cell number in cluster biofilm results in increased volume when compared to biofilms with a larger population. The hypothesis is that the significant changes in cell–cell spacing between small and large clusters in biofilms are due to strong temporal variation in ECM composition or production levels per cell (Drescher et al., 2016). In agreement, the flower-like clusters of *C. neoformans* present a high volume of ECM and relatively low cell concentration, as supported by our findings. For instance, the shunting procedures used to treat cryptococcal meningitis hypertension are risk associated and have historically discouraged surgeons due to its complications (Liu et al., 2014; Cherian et al., 2016) since it can provide a surface for cryptococcal attachment. It is common knowledge that uropathogenic strains of *Escherichia coli* can successfully adhere to and colonize the kidney, despite the presence of high flow rates. Since kidney tubules are narrow ($<50\,\mu m$), bacterial attachment patterns at even very small spatial scales can easily block them, increasing the severity of kidney infection (Melican et al., 2011).

The architectural flower-like cluster organization observed in serotype D B3501 strain might provide the yeast cells with a protected niche against antifungals, host defenses, environmental predators and dehydration. Physical differences in *C. neoformans* serotypes A and D biofilms may reflect the predilection of some serotype D strains for peripheral tissue (e.g., skin) whereas the structure of serotype A biofilms may select these strains in tissues such as the lungs (Abdulkareem et al., 2015). As demonstrated, cryptococcal cells may detach from the biofilm in an organized manner. It is plausible to assume that organization may be needed for the successful dissemination to the host. In fact, researchers showed that *Candida albicans* detached cells from biofilms are more metabolically active than planktonic cells (Uppuluri et al., 2010).

Upon this scenario, special treatment of the devices or the use of materials that hinder the initial organization may be used clinically to avoid the development of infection, by disrupting the initial organization. Moreover, the introduction of an objective measure of order ($\psi_6$) obtained from an image may facilitate the analysis of whether a given surface is prone to biofilm formation.

Continued studies are required to provide a greater understanding of the importance to investigate the complications of cryptococcal meningoencephalitis associated to the spatial distribution of clusters, as well as new methods of imaging for helping the development of new anti-biofilm targets.

## AUTHOR CONTRIBUTIONS

WL and GD: did the laboratory and MEV experiments; MeV and RdA: conceived the geometrical analysis; MeV: was responsible for the calculations and implementation of the geometrical analysis; WL, MeV, SF, CS, RdA, AS, LK, and MaV: did data analysis and interpretation; WL, MeV, SF, CS, RdA, AS, LK, and MaV: conceived the experiments and wrote the manuscript.

## FUNDING

This work was supported by Conselho Nacional de Desenvolvimento Científico e Tecnológico (CNPq 420276/2016-5). MeV was supported by a Senior fellowship from Coordenação de Aperfeiçoamento de Pessoal de Nível Superior (CAPES) in MIT (88881.119772/2016-01).

## ACKNOWLEDGMENTS

We thank Dr. Kildare Miranda and Rachel Rachid from CENABIO-UFRJ for their support and Dr. Marcio L. Rodrigues from FIOCRUZ/UFRJ for carefully reading the manuscript and for valuable comments. We thank Centro de Microscopia e Microanálise from UFRGS for the support.

## SUPPLEMENTARY MATERIAL

The Supplementary Material for this article can be found online at: https://www.frontiersin.org/articles/10.3389/fmicb.2017.02534/full#supplementary-material

## REFERENCES


Abdulkareem, A. F., Lee, H. H., Ahmadi, M., and Martinez, L. R. (2015). Fungal serotype-specific differences in bacterial-yeast interactions. *Virulence* 6, 652–657. doi: 10.1080/21505594.2015.1066962

Aeppli, G., and Bruinsma, R. (1984). Hexatic order and liquid density fluctuations. *Phys. Rev. Lett.* 53, 2133–2136. doi: 10.1103/PhysRevLett.53.2133

Aslanyan, L., Sanchez, D., Valdebenito, S., Eugenin, E., Ramos, R., and Martinez, L. (2017). The crucial role of biofilms in *Cryptococcus neoformans* survival within macrophages and colonization of the central nervous system. *J. Fungi* 3:10. doi: 10.3390/jof3010010

Banerjee, U., Gupta, K., and Venugopal, P. (1997). A case of prosthetic valve endocarditis caused by *Cryptococcus neoformans* var. neoformans. *J. Med. Vet. Mycol.* 35, 139–141. doi: 10.1080/02681219780001031

Berleman, J. E., Zemla, M., Remis, J. P., Liu, H., Davis, A. E., Worth, A. N., et al. (2016). Exopolysaccharide microchannels direct bacterial motility and organize multicellular behavior. *ISME J.* 10, 2620–2632. doi: 10.1038/ismej.2016.60

Bernard, E. P., and Krauth, W. (2011). Two-step melting in two dimensions: first-order liquid-hexatic transition. *Phys. Rev. Lett.* 107:155704. doi: 10.1103/PhysRevLett.107.155704

Borba, J. R., Brito, C., Migowski, P., Vale, T. B., Stariolo, D. A., Teixeira, S. R., et al. (2013). Quantitative characterization of hexagonal packings in nanoporous alumina arrays: a case study. *J. Phys. Chem. C* 117, 246–251. doi: 10.1021/jp308542d

Braun, D. K., Janssen, D. A., Marcus, J. R., and Kauffman, C. A. (1994). Cryptococcal infection of a prosthetic dialysis fistula. *Am. J. Kidney Dis.* 24, 864–867. doi: 10.1016/S0272-6386(12)80683-4

Cherian, J., Atmar, R. L., and Gopinath, S. P. (2016). Shunting in cryptococcal meningitis. *J. Neurosurg.* 125, 177–186. doi: 10.3171/2015.4.JNS15255

Clatworthy, A. E., Pierson, E., and Hung, D. T. (2007). Targeting virulence: a new paradigm for antimicrobial therapy. *Nat. Chem. Biol.* 3, 541–548. doi: 10.1038/nchembio.2007.24

Cogliati, M., Puccianti, E., Montagna, M. T., De Donno, A., Susever, S., Ergin, C., et al. (2017). Fundamental niche prediction of the pathogenic yeasts *Cryptococcus neoformans* and *Cryptococcus gattii* in Europe. *Environ. Microbiol.* 19, 4318–4325. doi: 10.1111/1462-2920.13915

Cordero, R. J., Pontes, B., Guimarães, A. J., Martinez, L. R., Rivera, J., Fries, B. C., et al. (2011). Chronological aging is associated with biophysical and chemical changes in the capsule of *Cryptococcus neoformans*. *Infect. Immun.* 79, 4990–5000. doi: 10.1128/IAI.05789-11

Costerton, J. W., Lewandowski, Z., Caldwell, D. E., Korber, D. R., and Lappin-Scott, H. M. (1995). Microbial biofilms. *Annu. Rev. Microbiol.* 49, 711–745. doi: 10.1146/annurev.mi.49.100195.003431

de S Araújo, G. R., Fontes, G. N., Leão, D., Rocha, G. M., Pontes, B., Sant'anna, C., et al. (2016). *Cryptococcus neoformans* capsular polysaccharides form branched and complex filamentous networks viewed by high-resolution microscopy. *J. Struct. Biol.* 193, 75–82. doi: 10.1016/j.jsb.2015.11.010

Drescher, K., Dunkel, J., Nadell, C. D., Van Teeffelen, S., Grnja, I., Wingreen, N. S., et al. (2016). Architectural transitions in *Vibrio cholerae* biofilms at single-cell resolution. *Proc. Natl. Acad. Sci. U.S.A.* 113, E2066–E2072. doi: 10.1073/pnas.1601702113

Dromer, F., Mathoulin, S., Dupont, B., Letenneur, L., and Ronin, O. (1996). Individual and environmental factors associated with infection due to *Cryptococcus neoformans* serotype D. French Cryptococcosis Study Group. *Clin. Infect. Dis.* 23, 91–96. doi: 10.1093/clinids/23.1.91

Edwards, M. R., Gordon, M. A., Lapa, E. W., and Ghiorse, W. C. (1967). Micromorphology of *Cryptococcus neoformans*. *J. Bacteriol.* 94, 766–777.

Flemming, H. C., and Wingender, J. (2010). The biofilm matrix. *Nat. Rev. Microbiol.* 8, 623–633. doi: 10.1038/nrmicro2415

Fortune, S. (1987). A sweepline algorithm for Voronoi diagrams. *Algorithmica* 2:153. doi: 10.1007/BF01840357

Fromtling, R. A., Shadomy, H. J., and Jacobson, E. S. (1982). Decreased virulence in stable, acapsular mutants of *Cryptococcus neoformans*. *Mycopathologia* 79, 23–29. doi: 10.1007/BF00636177

Gulati, M., and Nobile, C. J. (2016). *Candida albicans* biofilms: development, regulation, and molecular mechanisms. *Microbes Infect.* 18, 310–321. doi: 10.1016/j.micinf.2016.01.002

Hödl, I., Mari, L., Bertuzzo, E., Suweis, S., Besemer, K., Rinaldo, A., et al. (2014). Biophysical controls on cluster dynamics and architectural differentiation of microbial biofilms in contrasting flow environments. *Environ. Microbiol.* 16, 802–812. doi: 10.1111/1462-2920.12205

Jabra-Rizk, M. A., Falkler, W. A., and Meiller, T. F. (2004). Fungal biofilms and drug resistance. *Emerg. Infect. Dis.* 10, 14–19. doi: 10.3201/eid1001.030119

Johannsson, B., and Callaghan, J. J. (2009). Prosthetic hip infection due to *Cryptococcus neoformans*: case report. *Diagn. Microbiol. Infect. Dis.* 64, 76–79. doi: 10.1016/j.diagmicrobio.2009.01.005

Joubert, L.-M., Ferreira, J., and Stevens, D. (2015). *Aspergillus fumigatus* biofilms: a comparison of processing techniques for scanning electron microscopy of fungal mycelium and extracellular matrix. *Microsc. Microanal.* 21, 935–936. doi: 10.1017/S1431927615005474

Klapper, I. (2012). Productivity and equilibrium in simple biofilm models. *Bull. Math. Biol.* 74, 2917–2934. doi: 10.1007/s11538-012-9791-4

Klapper, I., and Szomolay, B. (2011). An exclusion principle and the importance of mobility for a class of biofilm models. *Bull. Math. Biol.* 73, 2213–2230. doi: 10.1007/s11538-010-9621-5

Kmetzsch, L., Joffe, L. S., Staats, C. C., De Oliveira, D. L., Fonseca, F. L., Cordero, R. J., et al. (2011). Role for Golgi reassembly and stacking protein (GRASP) in polysaccharide secretion and fungal virulence. *Mol. Microbiol.* 81, 206–218. doi: 10.1111/j.1365-2958.2011.07686.x

Kozel, T. R., and Gotschlich, E. C. (1982). The capsule of *cryptococcus neoformans* passively inhibits phagocytosis of the yeast by macrophages. *J. Immunol.* 129, 1675–1680.

Kragh, K. N., Hutchison, J. B., Melaugh, G., Rodesney, C., Roberts, A. E., Irie, Y., et al. (2016). Role of multicellular aggregates in biofilm formation. *MBio* 7:e00237. doi: 10.1128/mBio.00237-16

Kumar, A., and Ting, Y. P. (2013). Effect of sub-inhibitory antibacterial stress on bacterial surface properties and biofilm formation. *Colloids. Surf. B Biointerfaces* 111, 747–754. doi: 10.1016/j.colsurfb.2013.07.011

Lewis, K. (2008). Multidrug tolerance of biofilms and persister cells. *Curr. Top. Microbiol. Immunol.* 322, 107–131. doi: 10.1007/978-3-540-75418-3_6

Lidstrom, M. E., and Konopka, M. C. (2010). The role of physiological heterogeneity in microbial population behavior. *Nat. Chem. Biol.* 6, 705–712. doi: 10.1038/nchembio.436

Liu, L., Zhang, R., Tang, Y., and Lu, H. (2014). The use of ventriculoperitoneal shunts for uncontrollable intracranial hypertension in patients with HIV-associated cryptococcal meningitis with or without hydrocephalus. *Biosci. Trends* 8, 327–332. doi: 10.5582/bst.2014.01070

Martinez, L. R., and Casadevall, A. (2005). Specific antibody can prevent fungal biofilm formation and this effect correlates with protective efficacy. *Infect. Immun.* 73, 6350–6362. doi: 10.1128/IAI.73.10.6350-6362.2005

Martinez, L. R., and Casadevall, A. (2006a). *Cryptococcus neoformans* cells in biofilms are less susceptible than planktonic cells to antimicrobial molecules produced by the innate immune system. *Infect. Immun.* 74, 6118–6123. doi: 10.1128/IAI.00995-06

Martinez, L. R., and Casadevall, A. (2006b). Susceptibility of *Cryptococcus neoformans* biofilms to antifungal agents *in vitro*. *Antimicrob. Agents Chemother.* 50, 1021–1033. doi: 10.1128/AAC.50.3.1021-1033.2006

Martinez, L. R., and Casadevall, A. (2007). *Cryptococcus neoformans* biofilm formation depends on surface support and carbon source and reduces fungal cell susceptibility to heat, cold, and UV light. *Appl. Environ. Microbiol.* 73, 4592–4601. doi: 10.1128/AEM.02506-06

Martinez, L. R., and Casadevall, A. (2015). Biofilm Formation by *Cryptococcus neoformans*. *Microbiol. Spectr.* 3, 1–11. doi: 10.1128/microbiolspec.MB-0006-2014

Martinez, L. R., Mihu, M. R., Han, G., Frases, S., Cordero, R. J., Casadevall, A., et al. (2010). The use of chitosan to damage *Cryptococcus neoformans* biofilms. *Biomaterials* 31, 669–679. doi: 10.1016/j.biomaterials.2009.09.087

Melican, K., Sandoval, R. M., Kader, A., Josefsson, L., Tanner, G. A., Molitoris, B. A., et al. (2011). Uropathogenic *Escherichia coli* P and Type 1 fimbriae act in synergy in a living host to facilitate renal colonization leading to nephron obstruction. *PLoS Pathog.* 7:e1001298. doi: 10.1371/journal.ppat.1001298

Nelson, D. (2002). *Defects and Geometry in Condensed Matter Physics*. Cambridge: Cambridge University Press.

Nelson, D. R., and Halperin, B. I. (1979). Dislocation-mediated melting in two dimensions. *Phys. Rev. B* 19, 2457–2484. doi: 10.1103/PhysRevB.19.2457

Nosanchuk, J. D., and Casadevall, A. (1997). Cellular charge of *Cryptococcus neoformans*: contributions from the capsular polysaccharide, melanin, and monoclonal antibody binding. *Infect. Immun.* 65, 1836–1841.

Okabe, A., Boots, B., Sugihara, K., Chiu, S. N. and Kendall, D. G. (2000). "Definitions and basic properties of voronoi diagrams," in *Spatial Tessellations: Concepts and Applications of Voronoi Diagrams, 2nd Edn.,* Hoboken, NJ: John Wiley & Sons, Inc.

Oliveira, N. M., Oliveria, N. M., Martinez-Garcia, E., Xavier, J., Durham, W. M., Kolter, R., et al. (2015). Biofilm formation as a response to ecological competition. *PLoS Biol.* 13:e1002191. doi: 10.1371/journal.pbio.1002191

Park, B. J., Wannemuehler, K. A., Marston, B. J., Govender, N., Pappas, P. G., and Chiller, T. M. (2009). Estimation of the current global burden of cryptococcal meningitis among persons living with HIV/AIDS. *AIDS* 23, 525–530. doi: 10.1097/QAD.0b013e328322ffac

Parsek, M. R., and Fuqua, C. (2004). Biofilms 2003: emerging themes and challenges in studies of surface-associated microbial life. *J. Bacteriol.* 186, 4427–4440. doi: 10.1128/JB.186.14.4427-4440.2004

Rajasingham, R., Smith, R. M., Park, B. J., Jarvis, J. N., Govender, N. P., Chiller, T. M., et al. (2017). Global burden of disease of HIV-associated cryptococcal meningitis: an updated analysis. *Lancet Infect. Dis.* 17, 873–881. doi: 10.1016/S1473-3099(17)30243-8

Ramage, G., Mowat, E., Jones, B., Williams, C., and Lopez-Ribot, J. (2009). Our current understanding of fungal biofilms. *Crit. Rev. Microbiol.* 35, 340–355. doi: 10.3109/10408410903241436

Robertson, E. J., and Casadevall, A. (2009). Antibody-mediated immobilization of *Cryptococcus neoformans* promotes biofilm formation. *Appl. Environ. Microbiol.* 75, 2528–2533. doi: 10.1128/AEM.02846-08

Rodrigues, M. L., Nimrichter, L., Oliveira, D. L., Frases, S., Miranda, K., Zaragoza, O., et al. (2007). Vesicular polysaccharide export in *Cryptococcus neoformans* is a eukaryotic solution to the problem of fungal trans-cell wall transport. *Eukaryotic Cell* 6, 48–59. doi: 10.1128/EC.00318-06

Sakaguchi, N. (1993). Ultrastructural study of hepatic granulomas induced by *Cryptococcus neoformans* by quick-freezing and deep-etching method. *Virchows Arch B Cell Pathol.* 64, 57–66. doi: 10.1007/BF02915096

Shah, N. B., Shoham, S., and Nayak, S. (2015). *Cryptococcus neoformans* prosthetic joint infection: case report and review of the literature. *Mycopathologia* 179, 275–278. doi: 10.1007/s11046-014-9847-0

Sheppard, D. C., and Howell, P. L. (2016). Biofilm exopolysaccharides of pathogenic fungi: lessons from bacteria. *J. Biol. Chem.* 291, 12529–12537. doi: 10.1074/jbc.R116.720995

Stacy, A., Mcnally, L., Darch, S. E., Brown, S. P., and Whiteley, M. (2016). The biogeography of polymicrobial infection. *Nat. Rev. Microbiol.* 14, 93–105. doi: 10.1038/nrmicro.2015.8

Uppuluri, P., Chaturvedi, A. K., Srinivasan, A., Banerjee, M., Ramasubramaniam, A. K., Köhler, J. R., et al. (2010). Dispersion as an important step in the *Candida albicans* biofilm developmental cycle. *PLoS Pathog.* 6:e1000828. doi: 10.1371/journal.ppat.1000828

Walsh, T. J., Schlegel, R., Moody, M. M., Costerton, J. W., and Salcman, M. (1986). Ventriculoatrial shunt infection due to *Cryptococcus neoformans*: an ultrastructural and quantitative microbiological study. *Neurosurgery* 18, 373–375. doi: 10.1227/00006123-198603000-00025

Wang, L., and Lin, X. (2015). The morphotype heterogeneity in *Cryptococcus neoformans*. *Curr. Opin. Microbiol.* 26, 60–64. doi: 10.1016/j.mib.2015.06.003

Wang, L., Tian, X., Gyawali, R., and Lin, X. (2013). Fungal adhesion protein guides community behaviors and autoinduction in a paracrine manner. *Proc. Natl. Acad. Sci. U.S.A.* 110, 11571–11576. doi: 10.1073/pnas.1308173110

Wang, L., Zhai, B., and Lin, X. (2012). The link between morphotype transition and virulence in *Cryptococcus neoformans*. *PLoS Pathog.* 8:e1002765. doi: 10.1371/journal.ppat.1002765

Watnick, P., and Kolter, R. (2000). Biofilm, city of microbes. *J. Bacteriol.* 182, 2675–2679. doi: 10.1128/JB.182.10.2675-2679.2000

Yan, J., Sharo, A. G., Stone, H. A., Wingreen, N. S., and Bassler, B. L. (2016). *Vibrio cholerae* biofilm growth program and architecture revealed by single-cell live imaging. *Proc. Natl. Acad. Sci. U.S.A.* 113, E5337–E5343. doi: 10.1073/pnas.1611494113

**Conflict of Interest Statement:** The authors declare that the research was conducted in the absence of any commercial or financial relationships that could be construed as a potential conflict of interest.

*Supplementary Material*

# Geometrical distribution of *Cryptococcus neoformans* Mediates Flower-Like Biofilm Development

**William Lopes[1#], Mendeli H. Vainstein[2#], Glauber R. de S. Araújo[3], Susana Frases[3], Charley C. Staats[1], Rita M. C. de Almeida[2, 4], Augusto Schrank[1], Lívia Kmetzsch[1], Marilene H. Vainstein[1*]**

***Correspondence**

Marilene Henning Vainstein

mhv@cbiot.ufrgs.br

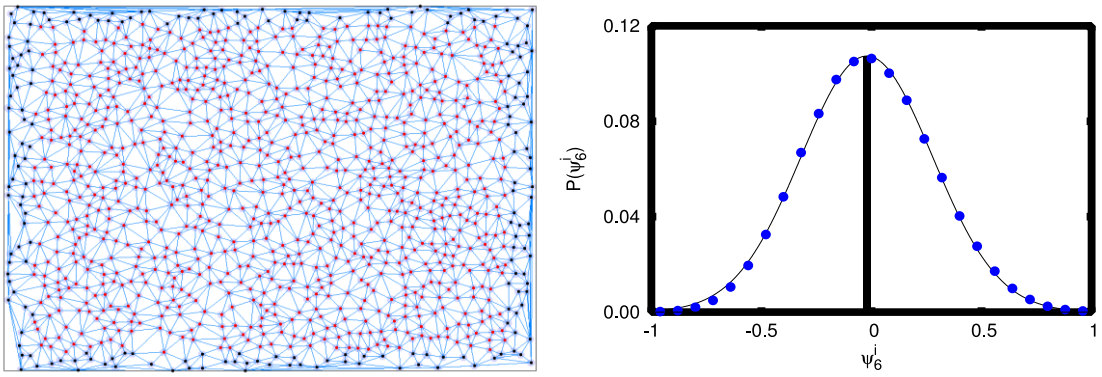


**Figure S1** Set of randomly distributed non-overlapping disks and distribution of $\psi_6$ for 1000 random sets. A) Blue line segments compose the Delaunay triangulation network for a randomly distributed set of disks, which are not allowed to overlap (the minimum distance between 2 disks is $2R$, where the disk radius is $R \approx 7.6$ pixels, corresponding to the average cell radius of Fig. 2A). To minimize border effects, disks lying close to a boundary (a distance within 5% of the figure length) were discarded

(black dots) for the calculation of $\psi_6$ ($\psi_6 \approx 0.0096$, N = 867, $N_{tot}$ = 1064). B) Distribution of $\psi_6$ for 1000 independent samples with the same parameters: the vertical line corresponds to the average $\langle\psi_6\rangle \approx -0.013816$. The dimensions of the box are $L_x = 1024$ and $L_y = 768$ pixels, equal to those of the image in Fig 2A.

*Supplementary Material*

# Geometrical distribution of *Cryptococcus neoformans* Mediates Flower-Like Biofilm Development

**William Lopes[1#], Mendeli H. Vainstein[2#], Glauber R. de S. Araújo[3], Susana Frases[3], Charley C. Staats[1], Rita M. C. de Almeida[2, 4], Augusto Schrank[1], Lívia Kmetzsch[1], Marilene H. Vainstein[1*]**

***Correspondence**

Marilene Henning Vainstein

mhv@cbiot.ufrgs.br

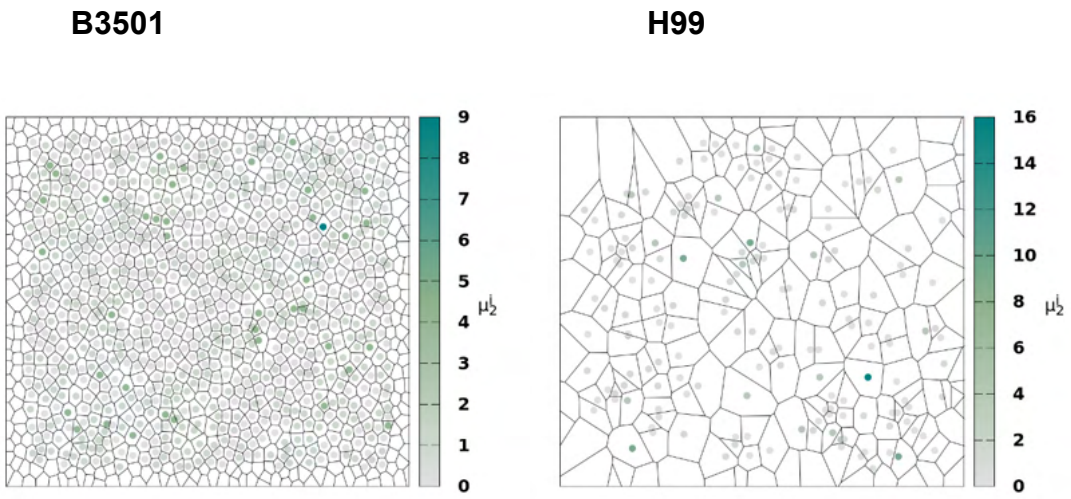


**Figure S2** Analysis of the variance of the number of nearest neighbors, $\mu_2^i$, for samples without Poly-L-lysine. Left: *C. neoformans* B3501. Right: *C. neoformans* H99.

**3.2 Capítulo II:** Scanning electron microscopy and machine learning reveal heterogeneity in capsular morphotypes of the human pathogen *Cryptococcus* spp. Publicado na Scientific Reports, 2020.

SCIENTIFIC REPORTS
nature research

OPEN

# Scanning electron microscopy and machine learning reveal heterogeneity in capsular morphotypes of the human pathogen *Cryptococcus* spp.

William Lopes[1,6], Giuliano N. F. Cruz[2,6], Marcio L. Rodrigues[3,4], Mendeli H. Vainstein[5], Livia Kmetzsch[1], Charley C. Staats[1], Marilene H. Vainstein[1] & Augusto Schrank[1*]

**Phenotypic heterogeneity is an important trait for the development and survival of many microorganisms including the yeast *Cryptococcus* spp., a deadly pathogen spread worldwide. Here, we have applied scanning electron microscopy (SEM) to define four *Cryptococcus* spp. capsule morphotypes, namely Regular, Spiky, Bald, and Phantom. These morphotypes were persistently observed in varying proportions among yeast isolates. To assess the distribution of such morphotypes we implemented an automated pipeline capable of (1) identifying potentially cell-associated objects in the SEM-derived images; (2) computing object-level features; and (3) classifying these objects into their corresponding classes. The machine learning approach used a Random Forest (RF) classifier whose overall accuracy reached 85% on the test dataset, with per-class specificity above 90%, and sensitivity between 66 and 94%. Additionally, the RF model indicates that structural and texture features, e.g., object area, eccentricity, and contrast, are most relevant for classification. The RF results agree with the observed variation in these features, consistently also with visual inspection of SEM images. Finally, our work introduces morphological variants of *Cryptococcus* spp. capsule. These can be promptly identified and characterized using computational models so that future work may unveil morphological associations with yeast virulence.**

The methodological advances achieved during the last decade allowed the study of phenotype heterogeneity in clonal cells. Particularly, the use of microorganism models has challenged the classical view of the phenotype determinacy based on the genotype and environmental context[1–5].

It is generally accepted that phenotypic heterogeneity leads to an increase in fitness and diversity independently of genetic mutations[6]. In this regard, microbial populations benefit from the ability to switch morphotypes and create resilient subpopulations better equipped to adapt and survive in diverse environmental and host niches. This morphotype heterogeneity is evident in a wide range of characteristics, many of which are fundamental to microbial virulence[7].

A central requisite in such studies is the use of powerful detection methods and the application of statistics[8,9]. In particular, image analysis is a common task within the machine learning field[10,11]. Yet, the literature on classification of electron microscopy-derived images for biological applications is notably sparse. As such, most algorithmic implementations focus on simpler methods for image data generation[12].

The human pathogenic yeasts belonging to the *Cryptococcus* complex have been consistently used as a model for the study of pathogenicity and for the development of better therapeutic approaches. Infections caused by this

[1]Centro de Biotecnologia, Universidade Federal do Rio Grande do Sul, Porto Alegre, Rio Grande do Sul, Brazil. [2]BiomeHub, Florianópolis, Santa Catarina, Brazil. [3]Instituto Carlos Chagas, Fiocruz, Curitiba, Paraná, Brazil. [4]Instituto de Microbiologia Paulo de Góes (IMPG), Universidade Federal do Rio de Janeiro (UFRJ), Rio de Janeiro, Rio de Janeiro, Brazil. [5]Departamento de Física, Instituto de Física, Universidade Federal do Rio Grande do Sul, Porto Alegre, Rio Grande do Sul, Brazil. [6]These authors contributed equally: William Lopes and Giuliano N. F. Cruz. *email: argusto@gmail.com

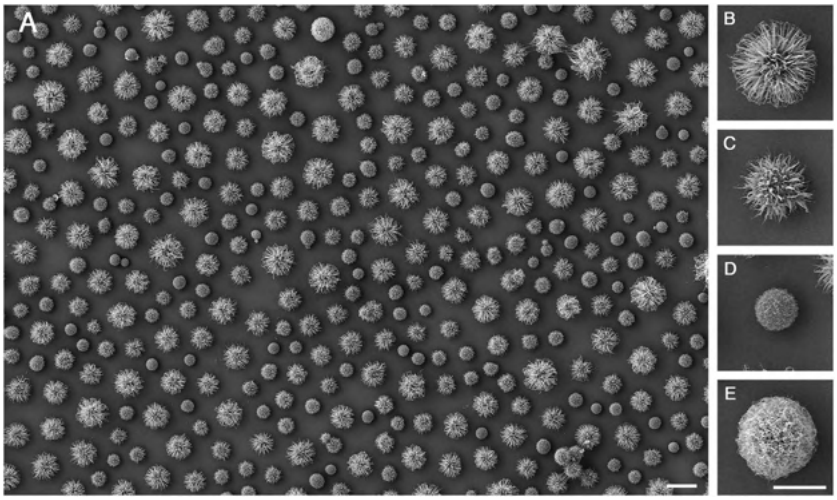


**Figure 1.** Morphological diversity of the cryptococcal capsule based on SEM analysis of a clinical isolate of *C. gattii*. (**A**) SEM image showing the coexistence of different morphotypes, which were classified on the basis of morphological characteristics including fiber abundance, capsule thickness, size and apparent texture. The capsular morphotypes were named regular (**B**), spiky (**C**), bald (**D**), and phantom (**E**). Scale bars: 10 μm (**A**) and 5 μm (**B**–**E**).

yeast kill 180,000 people around the world every year[13]. In addition, the treatment of cryptococcosis is unaffordable in most in developing countries[14,15].

An important trait for cryptococcal virulence is the presence of a polysaccharide capsule, which has been well described at the molecular and functional levels[16,17]. Capsular morphology includes a huge heterogeneity among distinct isolates and even in clonal isolates. This cellular diversity has been exploited in terms of drug resistance and pathogenic potential[18–20].

The study of phenotype heterogeneity is hampered by the lack of proper detection methods and statistical analyses. In order to further explore this morphotype diversity, we implemented an automated image analysis pipeline. This machine learning approach is capable of detecting and classifying capsular morphotypes, being applicable to cell type quantification in microscopy-based experiments. While not a high-throughput technique per se, SEM does yield vast amounts of complex data. Here, we describe the adaptation of one algorithmic implementation for the analysis and classification of *Cryptococcus* spp. capsular morphotypes captured using scanning electron microscopy (SEM). Our model substantially increases data analysis efficiency and provides a template for future machine learning applications within microbiology.

## Results

***Cryptococcus* spp. exhibit distinct capsule morphotypes under scanning electron microscopy.** The analysis of *Cryptococcus* spp. morphology by SEM revealed different capsular morphotypes within clonal microbial cultures (Fig. 1A). From the visual observations, we named four different morphotypes which persistently appeared in varying proportions among different yeast isolates. These morphotypes were defined as regular (Fig. 1B), spiky (Fig. 1C), bald (Fig. 1D) and phantom (Fig. 1E).

**Image segmentation with ebimage.** *Cryptococcus* SEM raw images (N = 11, total cells = 811) were processed using the EBImage package available from Bioconductor[12]. Shortly, the pipeline segments images based on pixel intensity spatial distributions. Background is separated from potentially cell-derived entities. Objects comprised of too few pixels were discarded, and remaining instances were visually classified as their respective cellular morphotypes, artifacts, or unidentified (cells of unknown morphology), Fig. 2.

For each identified object, features such as pixel intensity, moment (*e.g.* eccentricity), shape and texture were extracted using the corresponding commands from the EBImage package[12]. Over 50 features per cell were obtained, the majority of which were invariant to cell position and/or rotation.

**Visualizing overall profiles with principal component analysis.** The final data matrix obtained was composed of over 800 cells (rows) and over 50 features (columns). In order to verify whether there were clear groupings among the observations, exploratory analysis was performed through Principal Component Analysis (PCA)[21]. This procedure achieves dimensionality reduction by projecting the data matrix into a new subspace, composed of linearly independent vectors (Principal Components – PCs), which can be treated as new, uncorrelated features. These new features are ordered decreasingly in terms of total explained variance and hence can be used to visualize global tendencies of the original data in lower dimensional space.

Figure 3 shows the PCA for the SEM images. Each axis is a Principal Component (PC) with its corresponding proportion of explained variance. Each point in the plot represents a single cell, and the colors represent the cell morphotypes. Points that lay closer together have similar overall profiles across all original features, while distant observations in the chart tend to be distinct in nature. The data captured the differences among the capsular

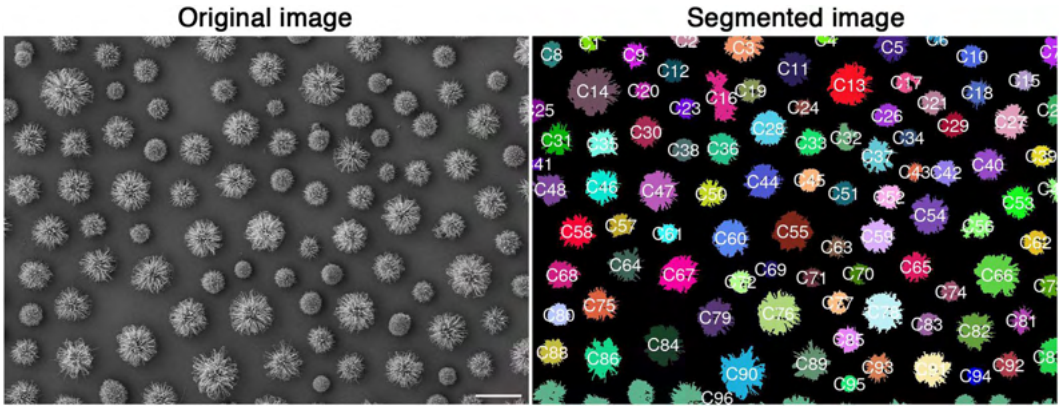


**Figure 2.** Illustration of image segmentation from a SEM image. The colors were randomly chosen to represent the distinct objects detected by EBImage. Unique identifiers are assigned to each object, and those were used for posterior manual labeling. Note that most cells are well distinguished, although marginal objects tend to be merged together, as illustrated by C96 at the very bottom. These merged cells, as well as other non-cellular objects, were all treated as artifacts. Cells that were not displayed entirely in the field of view such that no visual classification was possible were considered unidentified. Scale bar: 10 μm.

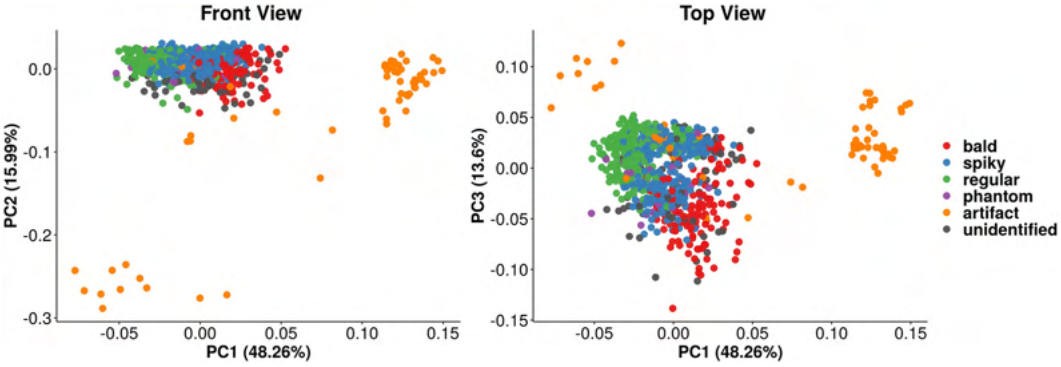


**Figure 3.** PCA of SEM image data. Each point represents a single cell, each color represents a given label: bald (red), regular (green), spiky (blue), phantom (purple), artifact (orange) or unidentified (grey). The left chart shows PC1 and PC2, resembling a "front view" of PCA. Bald, spiky, and regular cells show grouping patterns, although artifacts differ greatly. Unassigned cells appeared well distributed all over labeled cells, which indicates they may belong to any morphotype. The right chart shows a "top view", confirming the previous observations.

morphotypes, although clustering is hindered by partial overlap. This was further tested using a non-parametric version of multivariate ANOVA, which is capable of testing whether groups of observations show significantly different centroids[22]. Considering only those objects with actual cell morphotype labels, PERMANOVA revealed significant overall differences across cell types ($P < 0.001$). Also, the artifact observations were placed distant from all the labeled cells, indicating that their profiles differed in great extent. Finally, unidentified objects appeared distributed throughout the regions populated by labeled cells, which suggests they display cell-like properties and probably correspond to actual cells that failed to be manually classified into their corresponding morphotypes.

**Cellular morphotypes significantly differ in shape, moment, pixel intensity, and texture.** To further investigate morphological differences across identified cells, we used robust methodologies to compare basic (pixel-intensity related), shape, moment (eccentricity), and texture features across morphotypes. Figure 4 illustrates how the cells differ. The red lines connect the means, and pairwise comparisons were performed using Wilcoxon test. Although significant differences were often observed, note how pixel intensities do not seem to differ as much as contrast. Not surprisingly, mean radius seems to vary coordinately with major axis size.

As there were over 50 features to compare, we adapted a common analysis strategy from the genomics literature. Using robust regression, we estimated the means of each cell morphotype for all features. After multiple-comparison correction of P- values, non-significant regression coefficients were set to zero and contrasts were used to compose the estimated expectations. Translation- and rotation-variant features were left aside, as these represent positioning rather than cell type morphology. The scaled estimates were used to construct the heatmap shown in Fig. 5. We observed greater differences among shape and Haralick features, suggesting shape and texture are major components of morphological differentiation, consistent with visual inspection.

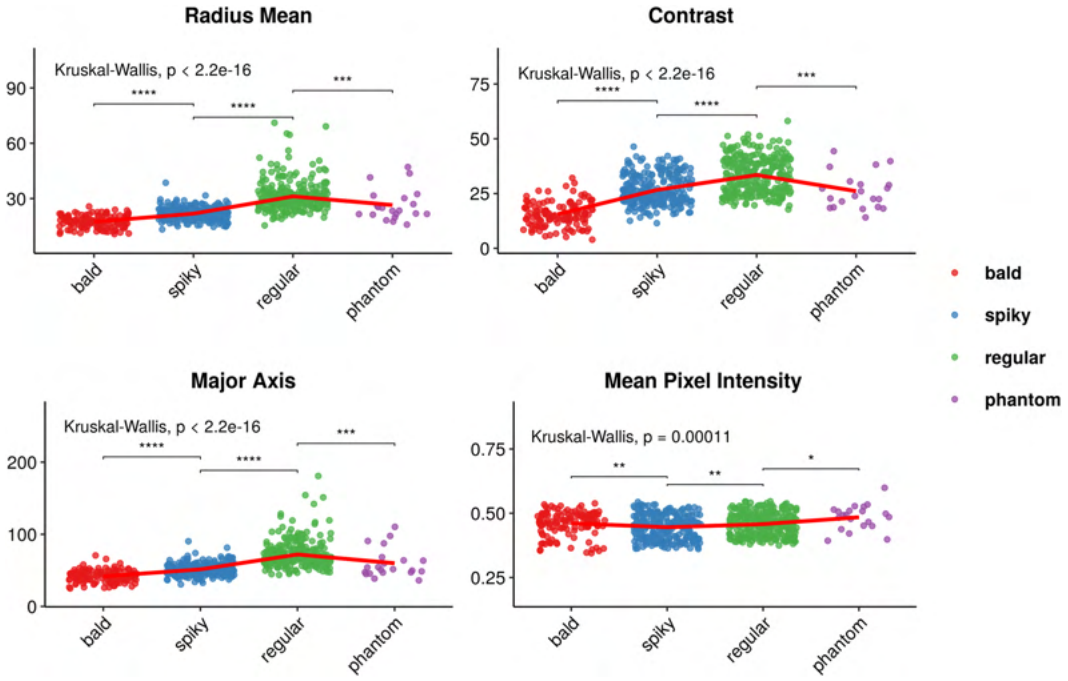


**Figure 4.** Capsular morphotypes differ significantly in mean radius, major axis size, mean pixel intensity, and contrast. Each point represents a single cell, and a small noise was added to each position to avoid overlap. Differences in shape (mean radius) tend to correlate with differences in moments (major axis), but also with texture (contrast). Pixel intensities (basic feature) differed significantly, but effect sizes do not seem to be nearly as large. The types of the features are named as defined in the EBImage R package. Red lines connect the means. Overall and pairwise comparisons computed with Kruskal-Wallis and Wilcoxon tests, respectively. $^{*}p <= 0.05$; $^{**}p <= 0.01$; $^{***}p <= 0.001$; $^{****}p <= 0.0001$.

**Machine learning predicts cellular morphotype.** In order to assess the degree with which the identified morphotypes were differentiable, we performed supervised classification using a Random Forest (RF). We split the cells into training and test sets with representative proportions of target labels (capsular morphotypes). Seventy five percent of the data were assigned to the training set. Using repeated 10-fold cross validation, we applied the Rborist algorithm (from within the Caret R package interface) to perform grid search on hyperparameters that were relevant for classification optimization[23,24]. The optimized parameters included the number of randomly selected predictors considered at each split within each tree (known as *mtry* or *predFixed*) and the minimal node size (*minNode*) considered for all trees in the RF model.

At this stage, the random forest was built of over 2,000 decision trees. Each tree splits the data into recursive partitions in a way that minimizes a function of node impurity, often the Gini index or Entropy[10]. By considering an aleatory subset of predictors at each split ("random"), the algorithm yields many uncorrelated trees. Among this aggregation of trees ("forest"), the majority vote for each observation is taken as its actual class. Supplementary Fig. S1 depicts the classification performance as a function of the number of randomly selected predictors for 10 different values of minimum node size. Using the training set, the top-performing hyperparameter values observed were 11 randomly selected predictors at each split and 7 as the minimum node size.

Once the RF classifier was built, we used it to predict the morphotype classes in the test set. This included the three cell types (bald, regular, and spiky), as well as artifacts and unassigned (unidentified) cells. This approach allowed for cell identification in the presence of unwanted objects, which are inherent to (and a current challenge for) high- throughput image segmentation[25]. Phantom cells were not included in as the sample size was considered too small for predictive modeling. The results are shown in Fig. 6. The overall accuracy was computed as the proportion of total correct predictions, settling at 85%. The model presented highly specific predictions for all classes (mean 96%, standard deviation 3.5%), while sensitivity varied more broadly (mean 86%, standard deviation 12.2%). Bald cells yielded the lowest sensitivity value (66%), while the greatest sensitivities were reported for regular cells, unidentified objects, and artifacts (93%, 94%, and 94%, respectively). All target classes showed specificities above 91%. Balanced accuracy (mean 91%, standard deviation 6.9%) was computed as the average between sensitivity and specificity for each group, ranging between 81% (bald) and 97% (artifact).

One of the main challenges for the predictive performance is the bias from manual labeling. This manual process is often affected by image-to-image variability, which itself can also be a source of bias. One way to overcome this issue is to increase the number of images analyzed. Nevertheless, such a procedure also relies on operator availability. Here, we used the so-called confusion matrix[23], a cross-tabulation of observed and predicted classes, to observe error tendencies from our model (Fig. 7). Columns represent the predicted morphotypes and rows represent the references. The correct predictions are in the principal diagonal, which represents the sensitivity values as the numbers shown are the relative proportions from row-wise calculations.

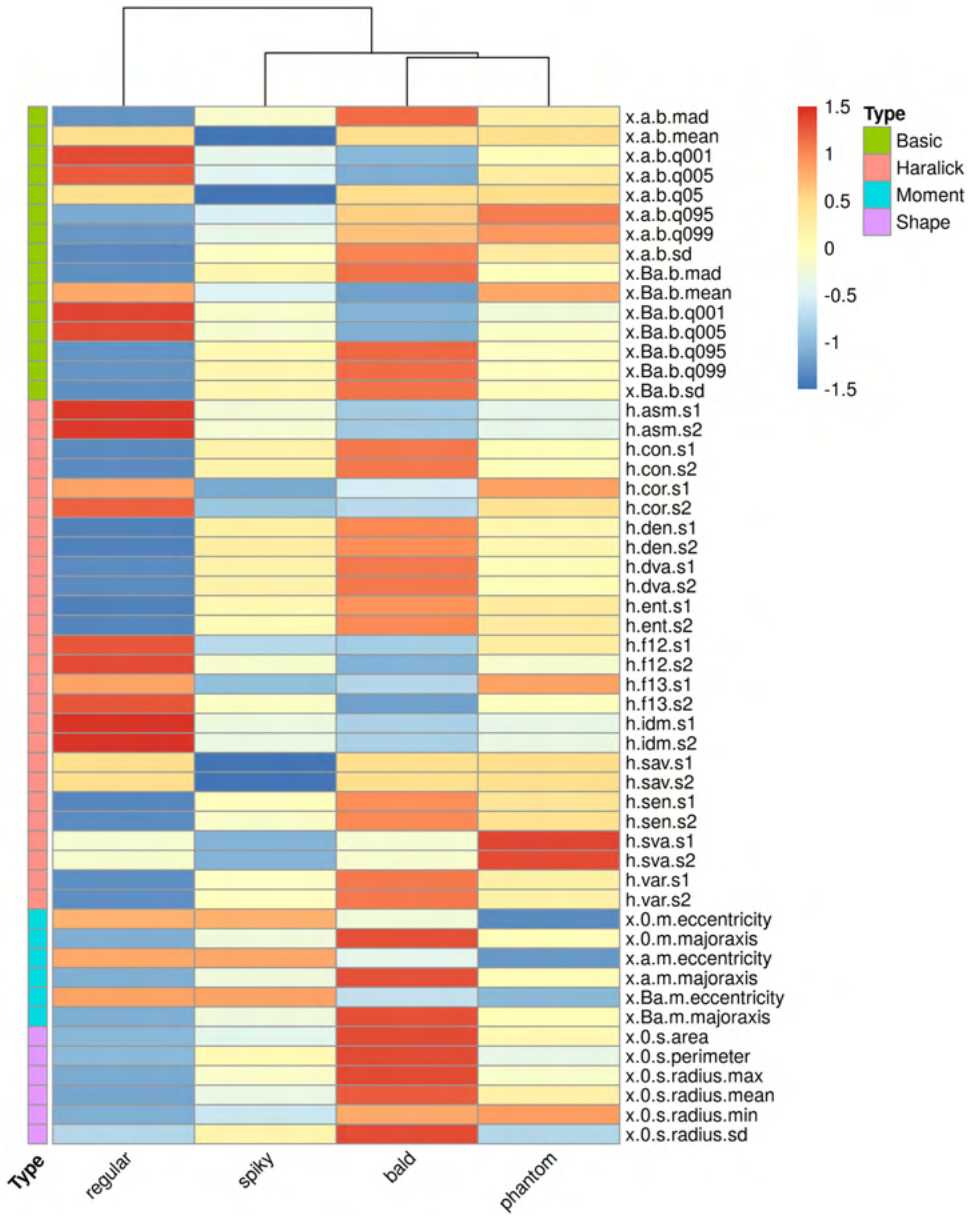


**Figure 5.** Capsular morphotypes differ significantly in intensity, shape, moment, and texture. We estimated the expected value (mean) for each cell morphotype across all features using robust regression. The scaled values are represented as color intensities, i.e., the greater the intensity, the greater a given cell type differs from the cross-group average for the corresponding feature. Non-significant regression coefficients were set to zero and in these cases the resulting color corresponds to the baseline (estimate for regular morphotypes). Near-zero values mean the cell morphotype was close to the cross-group average.

From the confusion matrix, it was clear that many bald cells are mislabeled as spiky, and many spiky as regular. These were the main errors leading to the two lowest sensitivity values observed (66% and 83%, for bald and spiky cells, respectively). These results may be affected by biases in visual labeling as these are often misinterpreted by the human eye. Also, unwanted objects (artifacts and unidentified) were mostly detected as such.

To further investigate the sources of error, the same results were plotted in Fig. 8 as a heatmap of class probabilities. As expected, unequal probabilities yield mostly correct predictions, and the classification challenges exposed by the confusion matrix were generally represented by cells with similar probabilities of morphotype assignment and, therefore, difficult to visually differentiate (*e.g.* bald versus spiky). These results indicate that manual labeling may be a major issue in predictive modeling of *Cryptococcus* spp. morphotypes using SEM images. However, such an effect may be resolved, for instance, with greater sample sizes. Nonetheless, it was clear that the pipeline showed satisfactory performances for object detection and classification, thereby enabling automated cellular morphotype analysis in SEM-derived *Cryptococcus* spp. images.

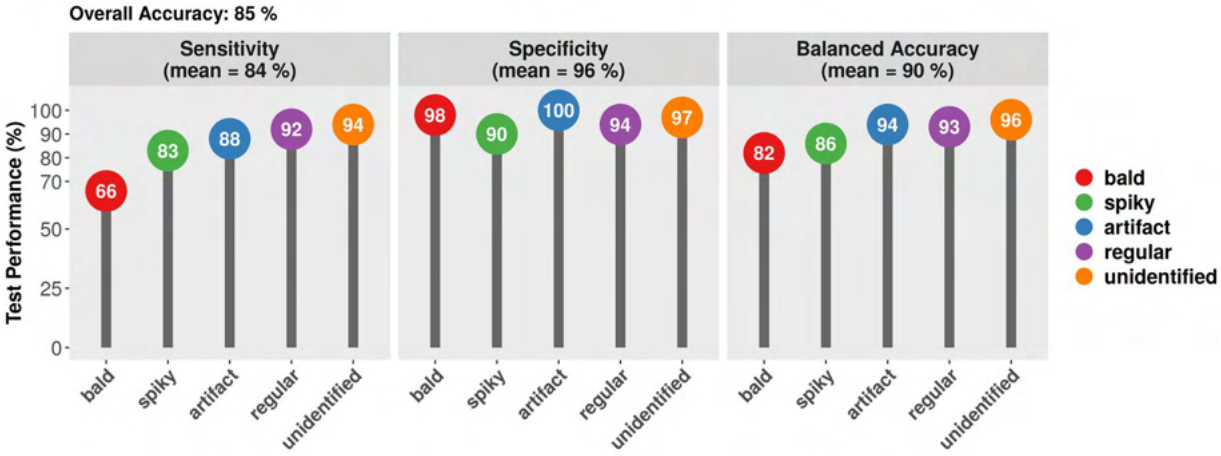


**Figure 6.** Random Forest prediction performance. Bald (red), spiky (green), regular (blue), artifact (purple) or unidentified (orange) morphotypes are shown. Performance values were sensitivity (left panel), specificity (middle panel), and average (balanced accuracy, right panel).

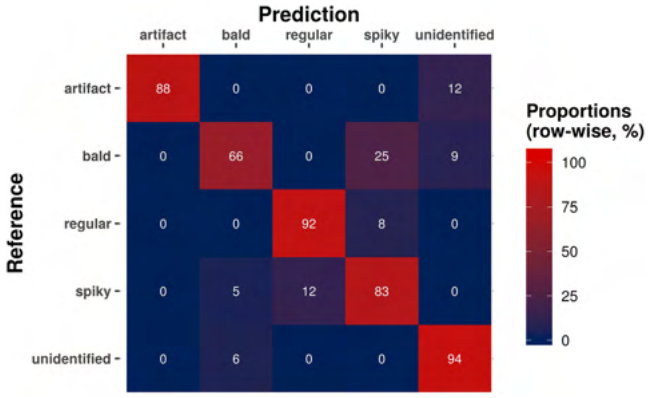


**Figure 7.** Cross-tabulation of observed and predicted values from RF classifier on the test set (confusion matrix). Proportions were calculated on a row-wise basis so that the principal diagonal shows the sensitivity values for each class, *i.e.*, the proportion of cells labeled in each class and detected as such. For example, 92% of regular cells were correctly classified, while 8% were mistakenly predicted as spiky.

**Image labeling with predicted morphotypes.** A drawback from random forest analysis, however, is the lack of interpretability[26]. Even though a given tree can be visualized from the resulting RF, this is not representative of the ensemble model. In order to overcome this issue, we plotted the actual predictions over the subjects of study. Figure 9 shows the original images along with the predicted annotations. The gray labels represented the correct predictions, while the red labels represented classification errors with the actual class within parentheses. The annotated objects were sparse as most observations were used for model building (comprising the training set). The visualization, hence, was constructed over the test set solely (N = 202). The green lines highlighted the detected objects from the automated segmentation procedure.

**Variable importance.** A useful application of random forest classifier is to infer variable importance, i.e., to estimate how important a given feature is for the overall classification task. For instance, features that cause major decreases in the Gini index, a measurement of node impurity, tend to show higher importance. Figure 10 shows such a measurement for all features considered during model building. Feature names describe source (*e.g.* pixel intensities or objects' binary masks), type (*e.g.* "s" for shape, "h" for haralick), and label (*e.g.* "radius.max" stands for maximum radius). For instance, to compute "binary - s.radius.sd", the EBImage package uses the binary mask generated from objects' segmentation (1 = foreground, 0 = background) and calculates the standard deviation of a set of radius measurements obtained for a given object.

Among the features with highest mean decrease in the Gini index, moment and shape features were notably prevalent - followed by Haralick features. This observation suggests that objects' structural characteristics had the highest influence on classification. Texture measurements also showed persistently high values, while basic features were less frequent among the most relevant variables. Indeed, the 5-quantile of pixel intensities, as measured after top hat transformation (top hat – b.q005), appeared among the 5 with the greatest mean decrease in Gini index. Feature cumulative information is what builds the random forest classifier, so assessment of individual predictors would not be representative. Still, each variable may leave clues about the partitions that the many

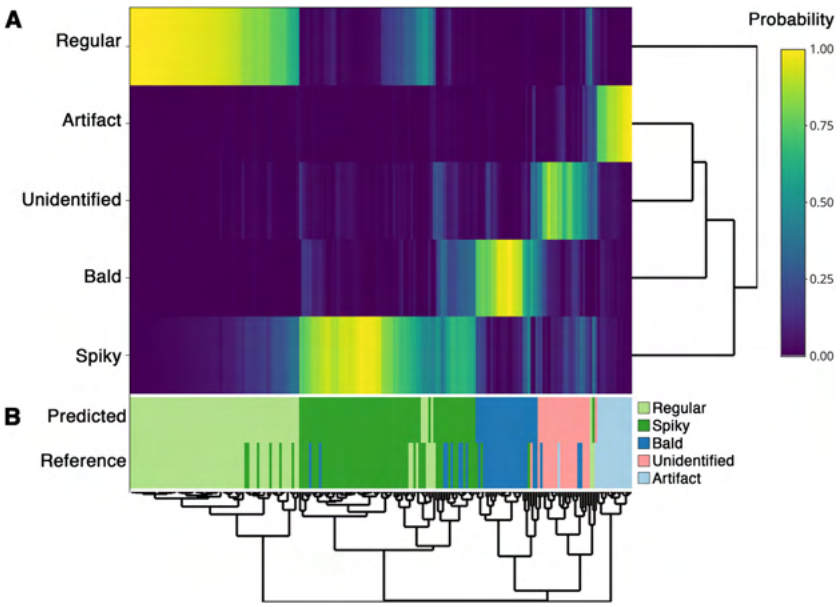


**Figure 8.** Heatmap of class probabilities obtained from the RF model. (**A**) The predicted probabilities are represented in the first five rows. (**B**) The predicted classes and reference labels are displayed on the remaining two rows. Most mismatches between predicted and reference rows (classification errors) occurred among objects difficult to differentiate even visually. This observation indicates that biases from manual labeling might be a significant challenge for classification accuracy.

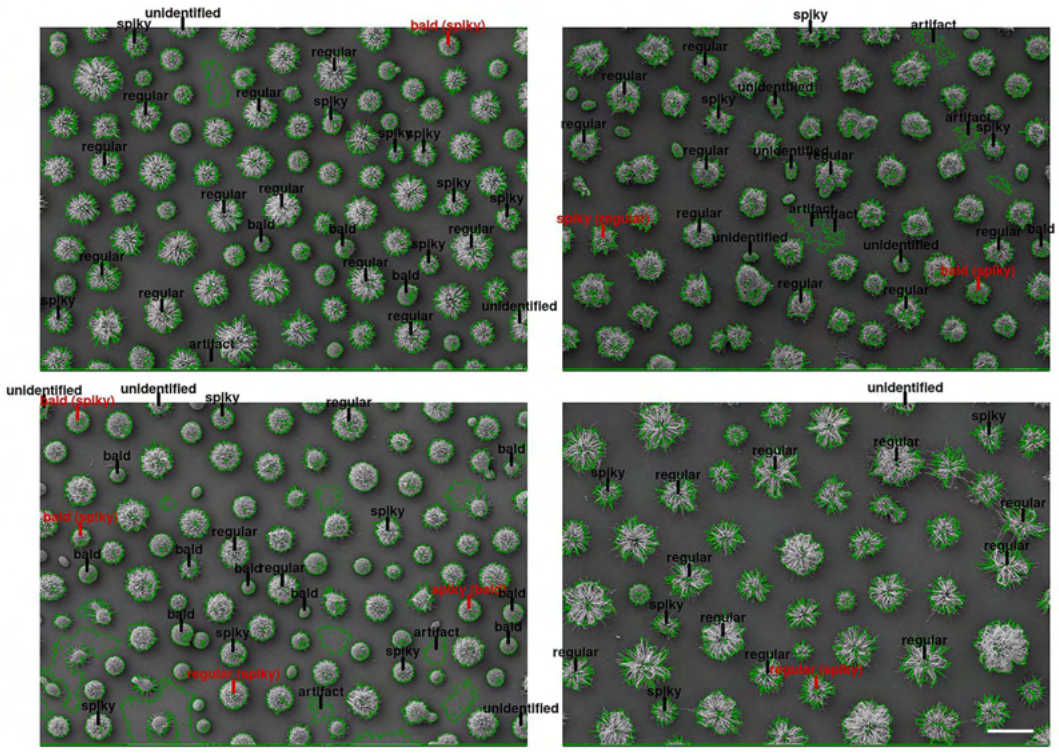

**Figure 9.** Original images with classification annotations. The predicted classes were mapped to their corresponding objects and drawn on top of the original images. Objects detected in the segmentation step are highlighted in green. Correct predictions are shown in gray, while misclassifications appear in red (with correct label in parentheses). Scale bar: 10 μm.

decisions trees produce at each recursive split. A Principal Coordinate Analysis was performed to yield a glimpse into the classification mechanism performed by the RF algorithm (see Supplementary Fig. S2). The actual relationships, distributions, and correlations for five of the most relevant features are detailed in Supplementary Fig. S3.

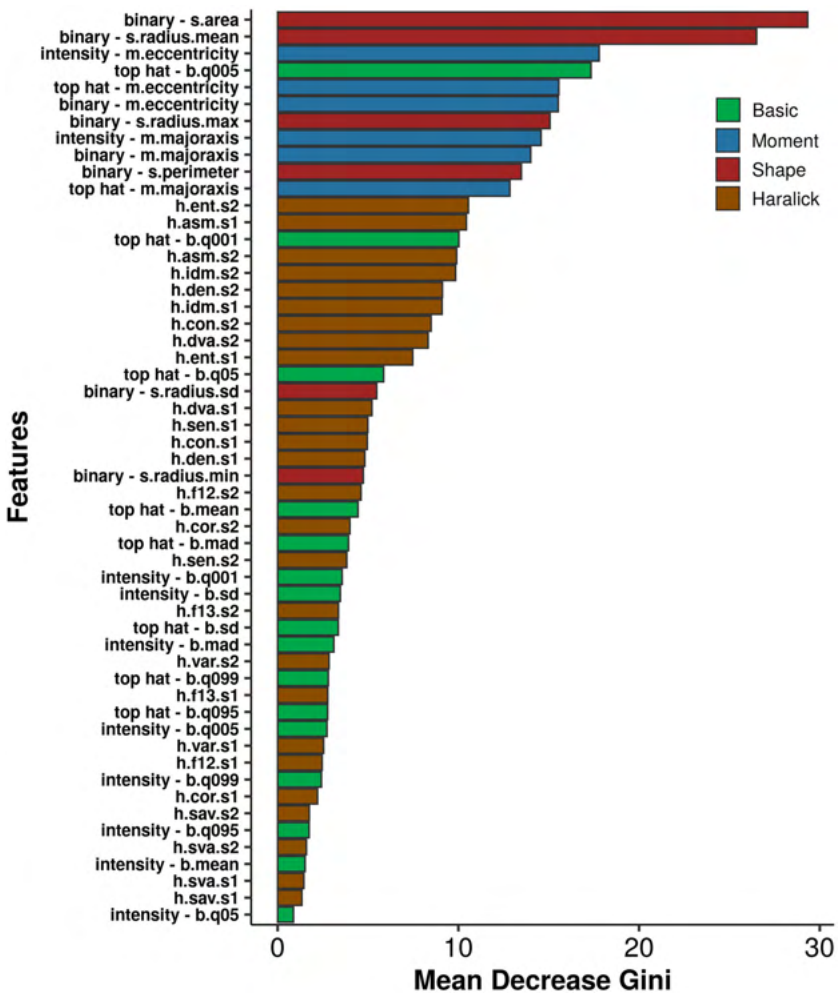


**Figure 10.** Feature importance and the mean decrease in the Gini index. Features are colored by type and may be calculated from three different sources: pixel intensities, segmentation-derived binary masks (*i.e.* images encoded as matrices in which identified objects are represented by 1, while background is coded as 0), and morphological top-hat transformations of pixel intensities.

## Discussion

Image analysis is a common task in machine learning, being especially valuable for biomedical applications[25]. Most research efforts, however, have been focused on technologies effortlessly adaptable to high-throughput processing, *e.g.*, light and fluorescence microscopy techniques[27–29]. While not as scalable, SEM produce high-resolution images for detailed phenotypic characterization at the single-cell level, shedding light onto otherwise obscure microbial diversity profiles[30]. Still, proper characterization relies on reproducible observation of cellular morphotypes, which encouraged the study herein presented.

*C. gattii* and *C. neoformans* are deadly pathogens with major mortality impacts worldwide[13]. The heterogeneity of its morphotypes has been demonstrated to be clinically relevant both in terms of virulence and drug resistance[18]. Here, we extensively characterized distinct capsule morphotypes and constructed a random forest classifier to predict such morphotypes in SEM-derived images. Based on the EBImage R package, the pipeline properly identified objects that potentially represented actual cells, differentiating these from the image background. After cell segmentation, feature extraction, and manual labeling, the cells showed significantly different shapes, moments, textures, and pixel intensity patterns. The differences detected were sufficient to yield reasonable predictions of cell subtypes using machine learning algorithm.

Model assessment revealed that class prediction was partially hampered by morphotypes difficult to differentiate visually, even for experienced operators. Nonetheless, random forest achieved satisfactory predictive performance through model tuning using grid search across relevant hyperparameters. The algorithm is known to reduce prediction variance as in bagging[26]. Although both techniques rely on ensembles of decision trees, RF de-correlates the generated trees by selecting a randomly-chosen subset of original features at each split. Suited for multi-class problems, our model was able not only to identify cell morphotypes, but also artifacts that remained from cell segmentation and even cells that could not be visually classified, *e.g.*, cells that were only partially displayed in the image frame. Furthermore, random forest models have the advantage of generating

estimates for variable importance. Our pipeline produced over 50 features of different types. In partial accordance with visual intuition, the decrease in Gini index, caused by variable permutations, indicated that structural features are most relevant for class prediction, followed by texture - although pixel intensities yielded important characteristics as well.

Finally, concerns may be risen regarding the biological meaning of the presented morphotypes. It is still unknown whether polysaccharide serotype and capsular morphotypes are correlated. However, the reported variation of capsular architecture within a single serotype of *C. gattii* argues against this hypothesis[31]. This highlights the importance of further investigation of capsular populations across genotypes and serotypes of *Cryptococcus* spp.

In conclusion, this study has applied computational tools to investigate clinically-relevant microbial morphotypes detected by SEM. We described *Cryptococcus* spp. capsular morphotypes in terms of shape, moments, texture, and pixel intensities. We also demonstrate these cellular morphotypes can be accurately predicted using machine learning techniques, which also gave insight into which features were most relevant for describing cell differences. It is clear that regular, bald, spiky, and phantom cells comprise significantly divergent morphotypes. It remains to be investigated, however, to which extent these cellular variations may affect virulence potential, drug susceptibility, and clinical practice.

## Materials and Methods

**Cryptococcal strains and growth conditions.** A total of 11 isolates (*C. gattii* strains: R265, WM 161 and 7 clinical isolates; *C. neoformans* strains: 2 clinical isolates) were included in this study. Cells were grown for 24 h at 30 °C in 25 mL of YPD broth in a rotary shaker at 150 rpm. The cells were counted using a hemocytometer and, to induce capsule formation, suspended at $10^5$ cells/mL in capsule-inducing minimal medium (3 µM thiamine, 15 mM glucose, 10 mM $MgSO_4$, 29.4 mM $KH_2PO_4$ and 13 mM glycine) following incubation for 72 h at 37 °C with 5% $CO_2$.

**Sample preparation for SEM image acquisition.** Capsule-induced cells were collected by centrifugation at 3,000 g for 5 min, washed three times in PBS and fixed (2.5% glutaraldehyde type 1 in 0.1 M sodium cacodylate buffer) for 1 h. Then, cells were washed in post-fixative solution (0.1 M sodium cacodylate buffer, 0.2 M sucrose and 2 mM $MgCl_2$), and adhered onto coverslips coated with 0.01% poly-L-lysine, for 30 min. The coverslips containing cryptococcal adhered cells were dehydrated in solutions of graded ethanol (30, 50 and 70%, for 5 min/step, then 95% and twice 100%, for 10 min/step). Samples were subjected to critical point drying (Critical Point Dryer CPD030 - Balzers), mounted on metallic stubs, coated with a 15–20 nm gold layer, and visualized in a scanning electron microscope (Zeiss Auriga), operating at 5–10 kV.

**Image pre-processing and object identification.** Based on the EBImage R package, we defined an automated segmentation pipeline capable of properly separating actual cell-associated pixels from background noise[12]. For preprocessing, all 11 images were primarily set to grayscale mode and 1024 × 724 pixels. Adaptive thresholding was performed using linear filtering. The local calculated background was removed from the original images for the construction of binary masks: in which 1 represents an object-associated pixel (foreground), and 0 represents the background, for each position in the image matrices. However, as the objects in these binary images often presented holes and blurred separations, they were propagated towards more lenient, fully filled binary masks through Voronoi tessellation[32]. Segmented objects with less than 1000 pixels were considered as obvious artifacts and hence assigned to the background.

**Feature extraction.** The identified objects proceeded to feature extraction, which included basic (*e.g.* intensity mean and standard deviation), shape (*e.g.* area, max radius, mean radius), and moment (*e.g.* eccentricity) variables. Texture was analyzed using gray-scale co-occurrence matrices as in EBImage's implementation of original Haralick features[12,33]. Variable names were coded as follows: *x.s.y.z* in which *x* is a placeholder, *s* is the feature source (*e.g.* binary mask or original image), *y* is the type (*e.g.* basic, shape), and *z* is the actual feature name (*e.g.* mean, area, radius). The feature type is identified as "s", "b", "m", and "h" for shape, basic, moment, and Haralick features, respectively. Feature source varied among "0", "a", and "Ba" for binary mask, original images, and top-hat transformed images, respectively. Note that only translation- and rotation-invariant features were kept for model construction to avoid spatial biases - *i.e.* cells being classified based on position-related characteristics. The final data set was comprised of 811 cells and 54 features.

The identified objects were manually labeled as regular (N = 285), bald (N = 129), or spiky (N = 261) morphotypes. Borderline cells detected by the pipeline were labeled as unidentified when manual labeling was hampered (N = 74). Also, as the high-throughput image processing yields artifacts, these were also labeled accordingly and considered for modeling (N = 62).

**Random forest classifier.** The labeled objects were then used to train a random forest (RF) model for morphotype classification. The optimization process was performed using the interface available from the Caret R package[23]. The RF algorithm chosen was the implementation from the Rborist R package, which allows for parallelism and fast optimization (within Caret) of two of the most relevant hyperparameters: minimal node size and number of randomly selected predictors at each split[24]. The optimal values were 9 and 10, respectively. The original data set was split into training and testing sets in a way that original class distributions were retained - using the sample.split function from Catools R package. All modeling optimization was carried out using repeated 10- fold cross validation (10 times) performed entirely on the training data set. Random Forests were constructed with 2000 trees each. The phantom capsular morphotypes were left aside as their total count was considered too low for model fitting (less than 3% of total cells).

**Statistical analysis.** Non-parametric comparisons were performed using Kruskal-Wallis and Wilcoxon tests. Robust regression was carried out using M estimator as implemented in the MASS R package[34]. Benjamini-Hochberg procedure was used for multiple comparisons correction of P-values. An alpha level of 0.05 was used as significance threshold in hypothesis testing.

## Code availability

All code and raw data are available at https://github.com/giulianonetto/crypto_classification. The pipeline is capable of (i) identifying potentially cell-associated objects in the SEM-derived images; (ii) computing object-level features; and (iii) classifying these objects into their corresponding classes.

Received: 26 August 2019; Accepted: 16 January 2020;
Published online: 11 February 2020

## References

1. Altamirano, S., Simmons, C. & Kozubowski, L. Colony and Single Cell Level Analysis of the Heterogeneous Response of Cryptococcus neoformans to Fluconazole. *Front. Cell Infect. Microbiol.* **8**, 203, https://doi.org/10.3389/fcimb.2018.00203 (2018).
2. van Boxtel, C., van Heerden, J. H., Nordholt, N., Schmidt, P. & Bruggeman, F. J. Taking chances and making mistakes: non-genetic phenotypic heterogeneity and its consequences for surviving in dynamic environments. *J. R. Soc. Interface* **14**, https://doi.org/10.1098/rsif.2017.0141 (2017).
3. Jin, M. *et al*. Divergent Aging of Isogenic Yeast Cells Revealed through Single-Cell Phenotypic Dynamics. *Cell Syst.* **8**, 242–253.e243, https://doi.org/10.1016/j.cels.2019.02.002 (2019).
4. Hommel, B. *et al*. Titan cells formation in Cryptococcus neoformans is finely tuned by environmental conditions and modulated by positive and negative genetic regulators. *PLoS Pathog.* **14**, e1006982, https://doi.org/10.1371/journal.ppat.1006982 (2018).
5. Axelrod, K., Sanchez, A. & Gore, J. Phenotypic states become increasingly sensitive to perturbations near a bifurcation in a synthetic gene network. *Elife* **4**, https://doi.org/10.7554/eLife.07935 (2015).
6. Grote, J., Krysciak, D. & Streit, W. R. Phenotypic Heterogeneity, a Phenomenon That May Explain Why Quorum Sensing Does Not Always Result in Truly Homogenous Cell Behavior. *Appl. Env. Microbiol.* **81**, 5280–5289, https://doi.org/10.1128/aem.00900-15 (2015).
7. Weigel, W. A. & Dersch, P. Phenotypic heterogeneity: a bacterial virulence strategy. *Microbes Infect.* **20**, 570–577, https://doi.org/10.1016/j.micinf.2018.01.008 (2018).
8. Miranda, K., Girard-Dias, W., Attias, M., de Souza, W. & Ramos, I. Three dimensional reconstruction by electron microscopy in the life sciences: An introduction for cell and tissue biologists. *Mol. Reprod. Dev.* **82**, 530–547, https://doi.org/10.1002/mrd.22455 (2015).
9. Libbrecht, M. W. & Noble, W. S. Machine learning applications in genetics and genomics. *Nat. Rev. Genet.* **16**, 321–332, https://doi.org/10.1038/nrg3920 (2015).
10. Efron, B. & Hastie, T. Computer Age Statistical Inference by Bradley Efron, https://doi.org/10.1017/CBO9781316576533 (2016).
11. Kather, J. N. *et al*. Deep learning can predict microsatellite instability directly from histology in gastrointestinal cancer. *Nat. Med.*, https://doi.org/10.1038/s41591-019-0462-y (2019).
12. Pau, G., Fuchs, F., Sklyar, O., Boutros, M. & Huber, W. EBImage–an R package for image processing with applications to cellular phenotypes. *Bioinforma.* **26**, 979–981, https://doi.org/10.1093/bioinformatics/btq046 (2010).
13. Rajasingham, R. *et al*. Global burden of disease of HIV-associated cryptococcal meningitis: an updated analysis. *Lancet Infect. Dis.* https://doi.org/10.1016/S1473-3099(17)30243-8 (2017).
14. Rodrigues, M. L. Neglected disease, neglected populations: the fight against Cryptococcus and cryptococcosis. *Mem. Inst. Oswaldo Cruz.* **113**, e180111, https://doi.org/10.1590/0074-02760180111 (2018).
15. Rodrigues, M. L. & Albuquerque, P. C. Searching for a change: The need for increased support for public health and research on fungal diseases. *PLoS Negl. Trop. Dis.* **12**, e0006479, https://doi.org/10.1371/journal.pntd.0006479 (2018).
16. de S Araújo, G. R. *et al*. Cryptococcus neoformans capsular polysaccharides form branched and complex filamentous networks viewed by high-resolution microscopy. *J. Struct. Biol.* **193**, 75–82, https://doi.org/10.1016/j.jsb.2015.11.010 (2016).
17. Guess, T. *et al*. Size Matters: Measurement of Capsule Diameter in Cryptococcus neoformans. *J. Vis. Exp.*, https://doi.org/10.3791/57171 (2018).
18. Wang, L. & Lin, X. The morphotype heterogeneity in Cryptococcus neoformans. *Curr. Opin. Microbiol.* **26**, 60–64, https://doi.org/10.1016/j.mib.2015.06.003 (2015).
19. Dambuza, I. M. *et al*. The Cryptococcus neoformans Titan cell is an inducible and regulated morphotype underlying pathogenesis. *PLoS Pathog.* **14**, e1006978, https://doi.org/10.1371/journal.ppat.1006978 (2018).
20. Lopes, W. *et al*. Geometrical Distribution of Cryptococcus neoformans Mediates Flower-Like Biofilm Development. *Front Microbiol* **8**, https://doi.org/10.3389/fmicb.2017.02534 (2017).
21. Jolliffe, I. T. & Cadima, J. Principal component analysis: a review and recent developments. *Philos. Trans. A Math. Phys. Eng. Sci.* **374**, 20150202, https://doi.org/10.1098/rsta.2015.0202 (2016).
22. Oksanen, J. *et al*. (ed Jari Oksanen) (CRAN, 2019).
23. Kuhn, M. Building Predictive Models in R Using the caret Package. *Journal of Statistical Software* **28**, https://doi.org/10.18637/jss.v028.i05 (2008).
24. Seligman, M. (CRAN, 2019).
25. Erickson, B. J., Korfiatis, P., Akkus, Z. & Kline, T. L. Machine Learning for Medical Imaging. *Radiographics* **37**, 505–515, https://doi.org/10.1148/rg.2017160130 (2017).
26. Hastie, T., Tibshirani, R. & Friedman, J. C. *Random Forests*, 587–604 (Springer, New York, NY, 2009).
27. Laufer, C., Fischer, B., Billmann, M., Huber, W. & Boutros, M. Mapping genetic interactions in human cancer cells with RNAi and multiparametric phenotyping. *Nat. Methods* **10**, 427–431, https://doi.org/10.1038/nmeth.2436 (2013).
28. Rivenson, Y. *et al*. Deep learning microscopy. *Optica* **4**, 1437–1443, https://doi.org/10.1364/OPTICA.4.001437 (2017).
29. Wang, H. *et al*. Deep learning enables cross-modality super-resolution in fluorescence microscopy. *Nat. Methods* **16**, 103–110, https://doi.org/10.1038/s41592-018-0239-0 (2019).
30. Lopes, W. *et al*. The duality of a deadly pathogen. *Clin. Microbiol. Infect.* **24**, 1064–1065, https://doi.org/10.1016/j.cmi.2018.07.009 (2018).
31. Rodrigues, J. *et al*. Pathogenic Diversity Amongst Serotype C VGIII and VGIV Cryptococcus Gattii Isolates. *Scientific reports* **5**, https://doi.org/10.1038/srep11717 (2015).
32. Holmes, S. & Huber, W. Modern Statistics for Modern Biology. Susan Holmes, Wolfgang Huber. Ch. 11, 270–308 (Cambridge University Press, 2019).
33. Haralick, R., Shanmugam, K. & Dinstein, I. Textural Features for Image Classification. *IEEE Trans. Systems, Man, Cybern.* **SMC-3**, 610–621, https://doi.org/10.1109/TSMC.1973.4309314 (1973).
34. Venables, W. N., Ripley, B. D. *Modern Applied Statistics with S*. (Springer, 2002).

## Acknowledgements

W.L. was supported by grant from the Brazilian agency Conselho Nacional de Desenvolvimento Científico e Tecnológico (CNPq, 142287/2017–2). M.H.V. was supported by grants from the Brazilian agency Conselho Nacional de Desenvolvimento Científico e Tecnológico (CNPq, 420276/2016-5, and 307191/2016-8). M.L.R. is currently on leave from the position of Associate Professor at the Microbiology Institute of the Federal University of Rio de Janeiro, Brazil. M.L.R. was supported by grants from the Brazilian agency Conselho Nacional de Desenvolvimento Científico e Tecnológico (CNPq, grants 405520/2018-2, 440015/2018-9, and 301304/2017-3) and Fiocruz (grants VPPCB-007-FIO-18-2-57 and VPPIS-001-FIO-18-66). We also acknowledge support from Coordenação de Aperfeiçoamento de Pessoal de Nível Superior (CAPES, finance code 001) and the Instituto Nacional de Ciência e Tecnologia de Inovação em Doenças de Populações Negligenciadas (INCT-IDPN). We thank Centro de Microscopia e Microanálise from UFRGS for the support.

## Author contributions

These authors contributed equally to this work: W.L. and G.N.F.C.; designed the experiments: W.L., G.N.F.C., Me.H.V., Ma.H.V. and A.S.; conceived the experiments: W.L. and G.N.F.C.; analyzed the data and results: W.L., G.N.F.C., A.S., M.L.R., Me.H.V., L.K., C.C.S., Ma.H.V. and A.S.; contributed to the manuscript writing: W.L., G.N.F.C., A.S., M.L.R., Me.H.V., Ma.H.V. and A.S.; directed and supervised the team members: Ma.H.V. and A.S. All authors reviewed and approved the final manuscript.

## Competing interests

The authors declare no competing interests.

## Additional information

**Supplementary information** is available for this paper at https://doi.org/10.1038/s41598-020-59276-w.

**Correspondence** and requests for materials should be addressed to A.S.

**Reprints and permissions information** is available at www.nature.com/reprints.

**Publisher's note** Springer Nature remains neutral with regard to jurisdictional claims in published maps and institutional affiliations.

**Supplementary Information (SI)**

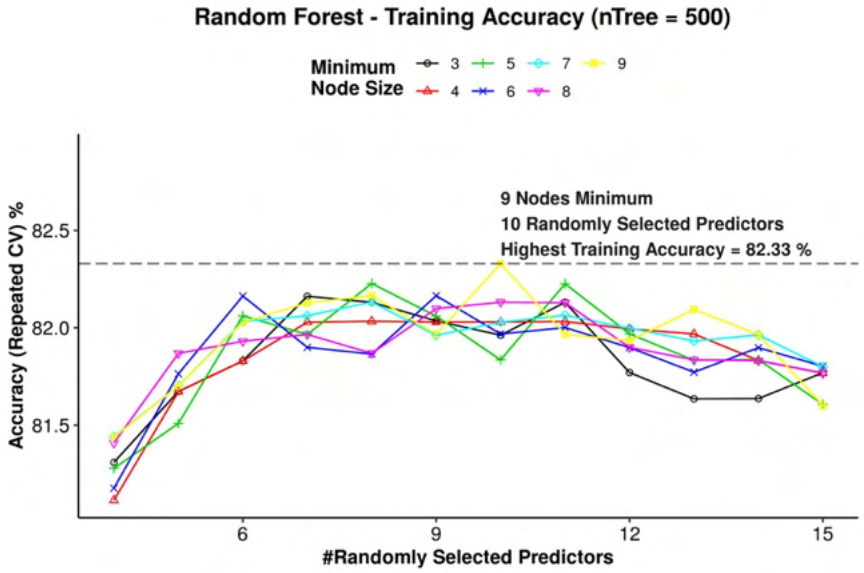


**Supplementary Fig. S1.** Tuning random forest hyperparameters. Accuracy estimations were generated from 10-fold cross-validation repeated 5 times. The training set comprised 75 % of all data. The best performance was achieved considering 11 randomly selected predictors at each split and having 9 as the minimum node size. Tuning procedure was performed using Rborist implementation from within the Caret modeling interface. The dashed line represents the highest accuracy point.

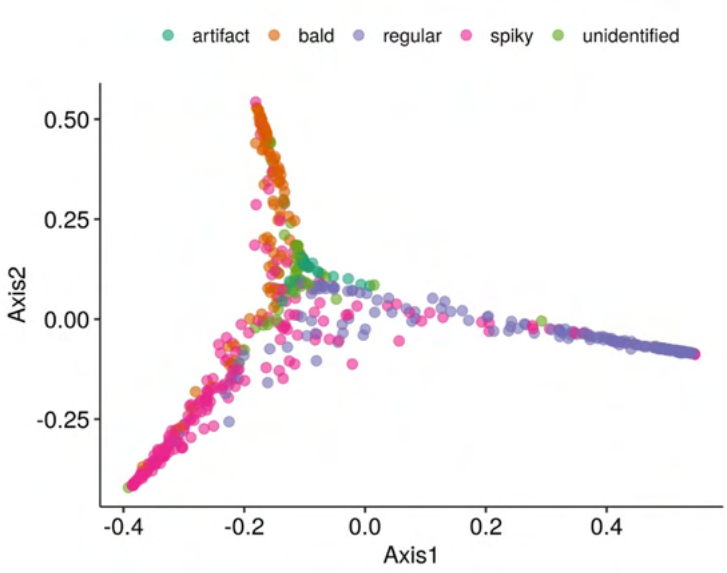


**Supplementary Fig. S2.** Principal Coordinate Analysis (PCoA) derived from sample proximities estimated by RF model. The random forest algorithm yields estimates of observations' proximities. A distance matrix was constructed by subtracting these values from one, serving as input for PCoA (also known as Multidimensional Scaling). The star shape is typical of this analysis (proximity plot). While unidentified objects and artifacts seem gathered in the middle, cell classes tend to form groupings apart from each other. Here we only visualize two dimensions from estimated proximity values - while the model itself considers the actual feature space.

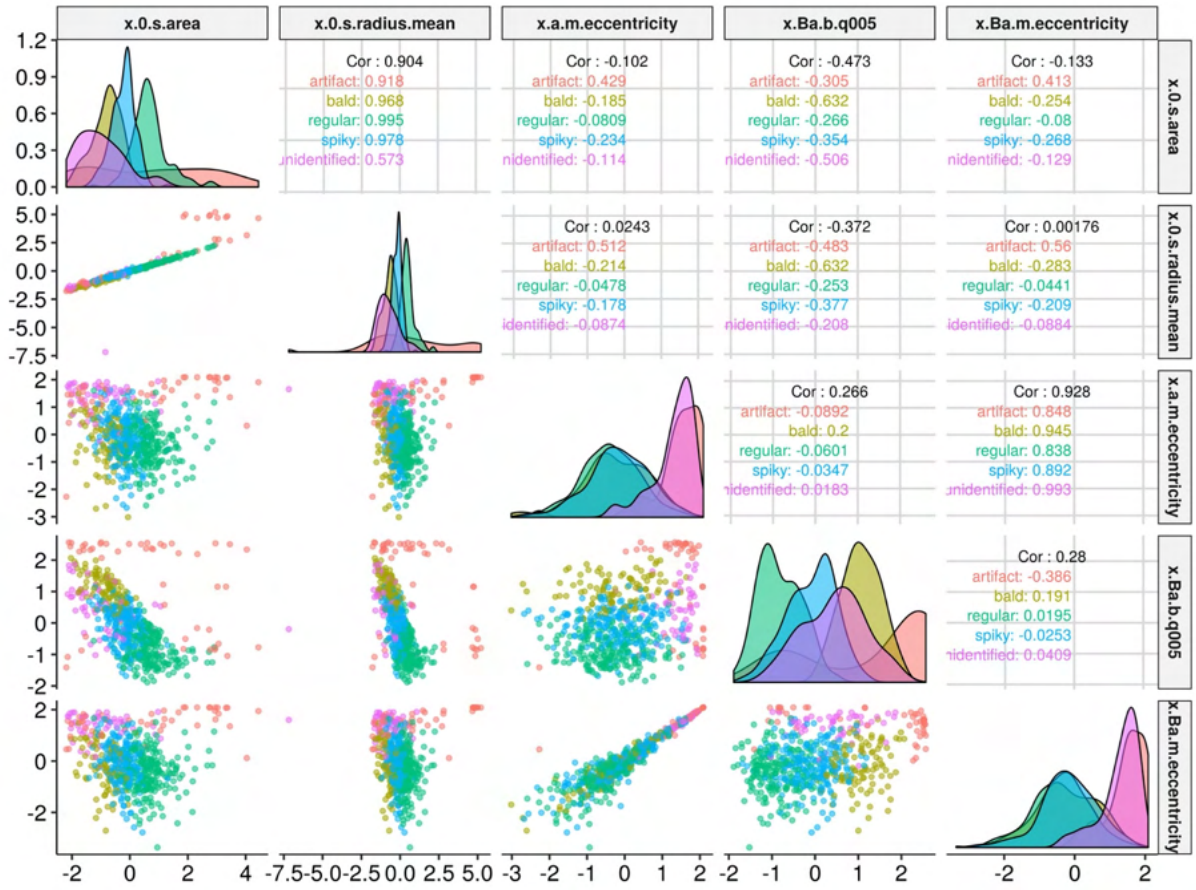


**Supplementary Fig. S3.** Correlations among the five most relevant features and their distributions. As indicated by the mean decrease in the Gini index, the five most important features seem to include shape, moment, and basic characteristics. Note that x.Ba.b.q005, the 5-quantile of pixel intensities after top hat transformation, is the only basic feature among the top 10 variables - others include texture (Haralick) features. Expectedly, objects' area and radius mean are highly correlated, which also happens between eccentricity calculated with reference images (x.a.m.eccentricity) and with the binary mask (x.0.m.eccentricity). However, the correlation values vary across classes. Additionally, notice that two-dimensional scatter plots fail to separate object classes completely - it is the features' cumulative information that is used by the RF algorithm to make predictions.

**3.3 Capítulo III:** The contest of microbial pigeon neighbors: Interspecies competition between *Serratia marcescens* and the human pathogen *Cryptococcus neoformans*.

Publicado na Fungal Biology, 2020.

Fungal Biology 124 (2020) 629–638

Contents lists available at ScienceDirect

Fungal Biology

journal homepage: www.elsevier.com/locate/funbio

# The contest of microbial pigeon neighbors: Interspecies competition between *Serratia marcescens* and the human pathogen *Cryptococcus neoformans*

Laura Haleva [1], William Lopes [1], Vanessa A. Barcellos, Augusto Schrank, Marilene H. Vainstein*

*Centro de Biotecnologia, Universidade Federal do Rio Grande do Sul, Porto Alegre, Rio Grande do Sul, Brazil*

ARTICLE INFO

*Article history:*
Received 24 October 2019
Received in revised form
4 March 2020
Accepted 10 March 2020
Available online 25 March 2020

Corresponding Editor: Steven Bates

*Keywords:*
Antagonism
Bacteria
Biofilm
Interspecies interaction
Yeast

ABSTRACT

In nature, microorganisms often exhibit competitive behavior for nutrients and limited space, allowing them to alter the virulence determinants of pathogens. The human pathogenic yeast *Cryptococcus neoformans* can be found organized in biofilms, a complex community composed of an extracellular matrix which confers protection against predation. The aim of this study was to evaluate and characterize antagonistic interactions between two cohabiting microorganisms: *C. neoformans* and the bacteria *Serratia marcescens*. The interaction of *S. marcescens* with *C. neoformans* expressed a negative effect on biofilm formation, polysaccharide capsule, production of urease, and melanization of the yeast. These findings evidence that competition in mixed communities can result in dominance by one species, with direct impact on the physiological modulation of virulence determinants. Such an approach is key for understating the response of communities to the presence of competitors and, ultimately, rationally designing communities to prevent and treat certain diseases.



## 1. Introduction

Throughout the years, microbiology has focused mainly on the study of single-species cultures. However, in the last decade several works have explored a new paradigm regarding complex communities: the behavioral modulation of organisms when co-cultivated with other species (Friedman and Gore, 2017; James et al., 1995; Nai and Meyer, 2018; Røder et al., 2016). This new approach is based on the fact that microorganisms live in dynamic and diversified groups, rather than alone in the microenvironment. Furthermore, studying monocultures does not allow for a complete understanding about the functions and composition of a community, especially with regards to human pathogens (McCully et al., 2019). Understanding the role of microorganisms and their associations with one another could lead to the identification of new antifungal activities and, subsequently, to new treatment strategies for infection-related diseases.

In nature, microorganisms often exhibit competitive behavior due to scarce nutrients and limited space (Friedman and Gore, 2017). Recent studies have revealed interactions between close constituents of the human skin microbiota, such as *Staphylococcus epidermidis* and *Propionibacterium acnes*, which showed antimicrobial activities (Christensen et al., 2016). Similarly, the probiotic yeast *Saccharomyces boulardii* can display a strong negative effect on *Candida albicans*' ability to form biofilms on plastic surfaces, as well as a significant inhibitory effect on the adhesion of *Candida glabrata* (Krasowska et al., 2009; Tomičić et al., 2016). Antagonistic mechanisms can also be demonstrated upon intercolonial contact, where motile *Bacillus subtilis* cells emerge from the mature biofilm to engulf the competing *Bacillus simplex* colony (Rosenberg et al., 2016).

The human pathogenic yeasts belonging to the *Cryptococcus* complex have been consistently used as a model for the study of pathogenicity and for the development of better therapeutic approaches (Mayer and Kronstad, 2019b). *Cryptococcus neoformans* (*Cn*) that live in soils, on trees and in bird droppings have also been described in interkingdom interactions (Dhamgaye et al., 2015;

* Corresponding author. Centro de Biotecnologia, Universidade Federal do Rio Grande do Sul, Av. Bento Gonçalves, 9500, 91501-970 Porto Alegre, Brazil. Fax: +55 51 3308 7309.
*E-mail address:* mhv@cbiot.ufrgs.br (M.H. Vainstein).
[1] These authors contributed equally to this work.

https://doi.org/10.1016/j.funbio.2020.03.004
1878-6146/

Rella et al., 2012). The soil bacterium *Bacillus safensis* can block several virulence determinants of *Cn*, including the production of melanin and the antiphagocytic polysaccharide capsule (Cordero et al., 2018; Saito and Ikeda, 2005). It has been proved that the lack of capsule formation genetically results in strongly reduced fungal virulence (Kwon-Chung and Rhodes, 1986). *B. safensis* also presented activity against filamentation and biofilm formation in *C. albicans*. Bacterial chitinase activity against fungal cell wall chitin was pointed as a factor that contributes to the antipathogenic effect of *B. safensis* (Mayer and Kronstad, 2017).

*Cn* has several virulence determinants, one being biofilm formation: A complex community of cells that is irreversibly associated with a surface and enclosed in a matrix of primarily polysaccharide material (Martinez and Casadevall, 2015). This attribute of resistance ensures their survival both on biotic and abiotic surfaces (Camacho and Casadevall, 2018), and serves as a barrier against antimicrobials, allowing for the identification of yeast in the pigeon gastrointestinal tract, mainly in urban areas (Chitty et al., 2019). Pigeons have an important role in the dispersion of *Cn* propagules in the environment. Fungal infections occur through the inhalation of spores and may lead to pneumonia and meningoencephalitis in the case of immunocompromised individuals (Camacho and Casadevall, 2018; Nielsen et al., 2007). Cryptococcal meningitis is a neglected infection, which affects approximately 220,000 people per year, causing an estimated 181,000 annual deaths (Rajasingham et al., 2017).

The aim of this work was to evaluate and characterize the antagonistic interactions between *Cn* and *Serratia marcescens* (*Sm*), an environmental microorganism isolated from pigeon excreta at the Parque Farroupilha in the city of Porto Alegre, RS, Brazil. *Sm* is a gram-negative bacteria member of the Enterobacteriaceae family which can cause nosocomial infections, urinary tract infections and respiratory diseases (Mahlen, 2011; Moradigaravand et al., 2016; Szewzyk et al., 1993). We found that the interaction of *Sm* with *Cn* has a negative effect on the virulence determinants of the yeast, including biofilm formation, production of urease and polysaccharide capsule formation. When incubated in contact on solid medium, the fungal colony is completely engulfed by the neighboring bacterial colony and a lower concentration of the fungus can be seen in the contact zone.

## 2. Materials and methods

### 2.1. Strains and culture conditions

*C. neoformans* var. *neoformans* wild-type strain B3501 (serotype D) and *C. neoformans* var. *grubii* wild-type strain H99 (serotype A) were used in this study as wild-type controls. Two mutant strains H99F and B3501F expressing a far-red fluorescent protein TurboFP635 (Katushka) generated in the laboratory were used for biofilm quantification and colony interaction through the detection of fluorescence by Living Image 3.1 Software on IVIS Lumina II. To generate the recombinant strains the 532 bp and 619 bp fragments corresponding to the histone H3 promoter region and terminator region of *C. neoformans* were amplified by PCR. The plasmid pTURBO-FP635-N contains the Katushka coding sequence, which was also amplified. The PCR products were analyzed in an agarose gel (0.8%) and purified using the Illustra GFX PCR DNA and Gel Band Purification Kit (GE Healthcare). These fragments were fused by PCR and cloned in the plasmid pJAF15 using the enzyme infusion according to the clontech protocol. The product was transformed into *Escherichia coli* TG-2 cells. The construct was confirmed by PCR and by cleavage with PvuII and XhoI. Approximately 10 μg of the resulting vector was used to perform biolistic transformation (Toffaletti et al., 1993). Transformants were selected on YPD agar medium supplemented with 200 μg/mL of the antibiotic Hygromycin to select cells containing the Kanamycin resistance marker. Overnight cultures of fungal strains were grown in liquid YPD medium (2% D-glucose, 2% peptone, 1% yeast extract) in a shaking incubator at 30 °C and 180 rpm and the isolated bacteria were grown in liquid LB (1% Bacto-tryptone, 0.5% yeast extract, 1% NaCl) in a shaking incubator at 30 °C and 180 rpm.

### 2.2. Isolation and identification of bacteria

Dry excreta of pigeons were collected at the Parque Farroupilha in Porto Alegre, RS, Brazil (−30.04°S, −51.22°W). Samples were suspended in sterile saline solution, homogenized in vortex and spread in Petri dishes containing Niger seed agar (5% *Guizotia abyssinica*, niger seed, 0.1% D-glucose, 0.1% $KH_2PO_4$, 0.1% creatinine, 1.5% agar) they were then incubated at 30 °C. Afterwards, bacterial colonies were randomly isolated from *Cn*-positive plates based on morphological differences. Subsequently, a screening was performed to evaluate the antibiofilm activity of dual-species (yeast-bacteria) in comparison to the monocultures. The bacteria that showed significant antagonist activity against *Cn* biofilm formation was selected for further investigation and identified by sequencing of 16S rDNA region using universal primers 16F27 (AGA GTT TGA TCM TGG CTC AG) and 16R1492 (TAC GGY TAC CTT GTT ACT T) according to previous protocols (Mulet et al., 2012). The identification was performed by comparing and filtering the sequences using the GenBank BLAST tool from the National Center of Biotechnology Information (NCBI). Matrix-assisted laser desorption ionization-time of flight mass spectrometry (MALDI-TOF MS) analysis was performed at the Hospital de Clínicas of Porto Alegre in order to confirm the results (Patel, 2019; Pavlovic et al., 2012).

### 2.3. Biofilm assays

The impact of interspecies interactions on fungal biofilm formation was evaluated with *Cn* strain B3501, a strong biofilm former, and the selected bacteria *Sm*. Bacterial and fungal inoculums of 24 h at 37 °C were washed twice with phosphate-buffered saline (PBS), resuspended in RPMI-1640 medium (0.52% medium Gibco; 1.73% MOPS buffer; pH 7; sterilized by filtration) and adjusted to the corresponding optical density of $10^7$ cells/mL (Kong et al., 2016). *Sm* and *Cn* were grown individually or mixed (*Cn* and *Sm* 1:1) in a 96-well microtiter plate in quadruplicate at 37 °C for 48 h. The plate was incubated at 60 °C for 1 h; it was then stained with crystal violet and incubated again at 80 °C for 15 min. The wells were then washed and dimethyl sulfoxide (DMSO) was added until the reading of OD at 570 nm (Ravi et al., 2009). To quantify the yeast in mixed biofilm, we repeated the experiment as described above using the fluorescent strain *B3501F* of *Cn*. The emitted fluorescence was measured by SpectraMax i3 (excitation/emission at 588/635 nm).

### 2.4. Capsule formation

For the analysis of polysaccharide capsule formation, *Cn* H99 alone as well as a mixture of *Cn* H99 with *Sm* were adjusted to $10^6$ cells/mL. The volume of 70 μL was added to 2 mL of medium containing 10% fetal calf serum (FCS) and incubated at 30 °C for 72 h under shaking (Mayer and Kronstad, 2017). Next, samples were stained with India ink to enable visualization of the polysaccharide capsule and visualized by optical microscopy (Zeiss Axioskop). Fifty cells of each condition were measured, and cell size measurements were performed using ImageJ 1.48.

### 2.5. Quantification of GXM by ELISA

To verify if there was a defect in capsule attachment to the cell wall of Cn, an enzyme-linked immunosorbent assay (ELISA) was performed for quantification of GXM secreted by *C. neoformans* when co-cultivated with *S. marcescens*. The inoculums of the yeast and the bacteria were washed and incubated in fetal calf serum (FCS) at $2 \times 10^7$ cells/mL for 48 h. After incubation, the cells were centrifuged for 20 min at 8000 rpm, 10 min at 8000 rpm and 10 min at 8000, transferring the samples to new Eppendorf's. In the ELISA plate, 75 μL of a 10 μg/mL solution of pure GXM was added to the first well, while in the others, 50 μL of PBS were added and a serial dilution was performed. The plate was incubated for 1 h at 37 °C and the supernatant was then discarded. It was added 200 μL of PBS + 1% BSA and the plate was incubated overnight at 4 °C to block the reaction. The supernatant was discarded and the plate was incubated for 1 h at 37 °C with 50 μL per well of 1 μg/mL of primary antibody 18B7 in PBS + 1% BSA. Again, the supernatant was discarded and the plate was washed three times with PBS + TWEEN 20 0.05%. The plate was incubated for 1 h at 37 °C with 50 μL per well of 1:2000 of secondary antibody IgG in PBS + TWEEN 20 0.05% + 1% BSA. It was washed three times with PBS + TWEEN 20 0.05% and 50 μL of TMB was added per well. After the wells changed their color, 50 μL of 0.4 M $H_2SO_4$ was added to stop the reaction and read on the spectrophotometer at 450 nm. Concentration of GXM was normalized by the number of the cells.

### 2.6. Cell wall integrity

Cells of *Cn* were visualized on confocal microscopy to verify its effect on the cell wall and capsule. First, the samples were washed, inoculated $1 \times 10^6$ cells/mL in FCS and incubated for 48 h at 37 °C. Cells were fixed with paraformaldehyde 4% for 30 min at 30 °C and washed with PBS. They were centrifuged for 2 min at 6000 rpm and a solution of PBS + 1% BSA was added and the samples were incubated for 30 min at 37 °C. After washing, the samples were incubated with 5 μg/mL of calcofluor at 37 °C for 30 min and then washed again with PBS. The cells were incubated with 10 μg/mL of 18B7 at 37 °C for 30 min and were washed again. They were incubated with secondary antibody IgG at a dilution of 1:200 at 37 °C for 30 min and washed with PBS. Finally, the samples were resuspended in 10 μL of PBS and placed on a slide for visualization in the confocal microscope.

### 2.7. Urease activity

The evaluation of *Cn* urease production during interaction with *Sm* was performed in Urea broth (0.1% peptone, 0.1% D-glucose, 0.5% NaCl, 0.2% $KH_2PO_4$, 2% urea, 0.0012% phenol red, sterilized by filtration). The fungal and bacterial cultures were inoculated in YPD broth and LB broth respectively, at 180 rpm for 24 h. Next, the cultures were adjusted to $OD_{600\ nm} = 1$ and mixed at a ratio 1:1. Mono and co-cultures were incubated on Urea medium at 37 °C with agitation for 6 h. Then, 200 μL were transferred to a new 96-well microplate and measured the $OD_{560\ nm}$ for quantification (Fu et al., 2018). A CFU counting of the cultures was performed to assess cell viability.

### 2.8. Melanin production

To test the effect of *Sm* on the melanin production of *Cn*, overnight cultures were washed with PBS and adjusted to $10^7$ cells/mL. Subsequently, the cultures were mixed together at a ratio 1:1 and 4 μL were inoculated on L-3,4-dihydroxyphenylalanine (0.02% L-DOPA, Sigma, 0.27% D-glucose, 0.246% $MgSO_4$ heptahydrate, 0.4% $KH_2PO_4$, 0.0975% glycine, 3 μM thiamine, sterilized by filtration) agar and incubated at 37 °C for 48 h.

### 2.9. Interspecies interaction in colonies

Cultures of *Sm* and *Cn* were grown at 37 °C for 24 h with shaking (180 rpm). Next, cell concentration was adjusted to $10^7$ cells/mL and the bacterial and fungal inoculums were pipetted onto YPD agar. Inoculums were spotted alone, mixed, or in contact with each other. Plates were incubated at 37 °C for 48 h (McCully et al., 2019). To evaluate the region of contact between the two colonies at the cellular level, the border of the *Cn* colony was sectioned with a coverslip and observed under a microscope.

#### 2.9.1. Scanner-based time-lapse of interspecies interaction

To visualize the development of mixed and direct contact colonies we performed a real time scanner-based time-lapse. Briefly, 5 μL of the inoculums were dropped onto YPD agar surface, followed by the incubation of the plates at 37 °C for 48 h. Colonies growth was automatically photographed every 1 h using the Epson Perfection V800 Photo Scanner. Each experiment was performed thrice.

#### 2.9.2. Fluorescence detection of C. neoformans

To visualize the presence of *Cn* colony when mixed or when in contact with *Sm*, the fluorescent strain H99F was used. After 48 h of incubation at 37 °C, images of the colonies were acquired using the IVIS Lumina II system and analyzed with the Living Image Software.

### 2.10. Scanning electron microscopy of colonies

Ultrastructural analysis was performed by scanning electron microscopy (SEM) of *Cn*–*Sm* colonies grown side by side at 37 °C for 48 h. (SEM) preparation was performed according to Lopes and Vainstein, 2017 with minor modifications (Lopes et al., 2017). After incubation, intact colonies were cut from the agar plates, carefully placed in 12 well microplates and fixed (2.5% glutaraldehyde and 0.1 M cacodilate 7.2 pH) for 1 h at room temperature. The wells were washed twice with a post-fixative solution (0.1 M cacodilate, 2 mM $MgCl_2$ and 0.2 M Sucrose) and subsequently dehydrated in ethanol (30% for 5 min, 50% for 5 min, 70% for 5 min, 95% for 10 min, 100% for 10 min and again 100%). Samples were then subjected to critical point drying immediately after dehydration, mounted on metallic stubs, sputter-coated with a 15–20 nm gold-palladium layer and visualized in a scanning electron microscope (Carl Zeiss EVO MA10) operating at 10 kV. The experiment was performed in three independent replicates.

### 2.11. Percentage of cell survival in fungal and bacterial interaction

To determine the percentage of survival of fungal and bacterial cells after 2 h of co-cultivation, pre-inoculums of *Cn* H99 and *Sm* were washed and adjusted to a final concentration of $10^8$ cells/mL in RPMI-1640 medium. Fungal and bacterial cells were mixed in 2 mL (ratio of 1:1) and incubated at 37 °C under agitation. Non-mixed samples were used as controls. After incubation, yeast and bacterial cells suspension were serially diluted and plated to determine the percentage of survival by CFU assay (Abdulkareem et al., 2015). To quantify *Cn*, 20 μL of suspensions were plated onto YPD agar supplemented with chloramphenicol (0.15 g/L; Sigma) to inhibit bacterial growth and incubated at 30 °C for 48 h; while 20 μL of bacterial cultures were plated on LB agar and supplemented with amphotericin B (0.2 μg/mL) to inhibit fungal growth, and incubated at 37 °C for 24 h (Abdulkareem et al., 2015). Colony forming units (CFU) were counted and the data analyzed.

### 2.12. Statistical analyses

Statistical analyses were performed with the GraphPad software (La Jolla, CA). Group comparisons were submitted to multiple comparison analysis of variance (ANOVA) and paired comparisons were performed with the Student's *t* test. Collection of data for analyses included average values of extracellular urease (absorbance units), capsule size (mm), biofilm formation (absorbance and fluorescence units), and CFU counting.

## 3. Results

### 3.1. Isolation and identification of antagonistic bacteria

Essentially, ecological communities developed a significant survival strategy in the microenvironment that includes protection of cells from hostile agents (Flemming et al., 2016), which allowed the emergence of defensive mechanisms. Therefore, we decided to investigate the effects of microorganisms found in the same niche of *Cn* and their competitive behaviors in the yeast. Pigeon droppings were collected from Parque Farroupilha in Porto Alegre. Afterwards, $1.05 \times 10^4$ CFU per gram of excreta was isolated after 48 h of cultivation in Niger medium. After cultivation, 55 morphologically different colonies were selected. From the isolation of the microorganisms, we performed interaction experiments for screening (Fig. S1). One species was selected for subsequent studies whose antagonistic effects on *C. neoformans* were more expressive for identification. Molecular identification by 16S DNA sequencing and confirmation by MALDI-TOF MS analyses revealed 99% similarity of the environmental microorganism to *S. marcescens* subsp. *Marcescens*.

Through light microscopy and Gram staining, it was possible to compare normal morphologies of *Cn* (Fig. 1A) and *Sm* (Fig. 1B) to the deformed *Cn* cells by the competing bacteria as observed in Fig. 1C.

### 3.2. Suppression of biofilm formation of C. neoformans by S. marcescens

Biofilm constitutes an attached polymicrobial community composed of an extracellular polymeric matrix that confers tolerance to antimicrobials and resistance to predators and other environmental agents (Martinez and Casadevall, 2015). Due to the fact

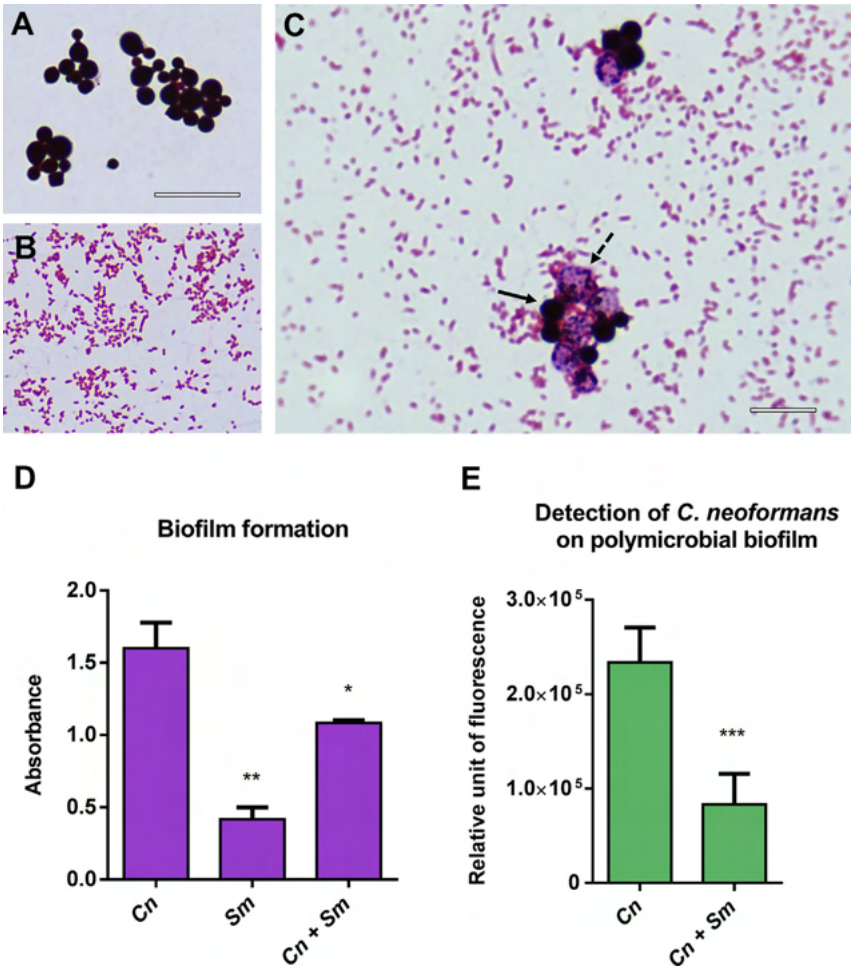


**Fig. 1.** Visualization of the cells of *C. neoformans* and *S. marcescens* and the effect of their interaction on biofilm formation. (A) Light microscopy showing *Cn* and *Sm* cells after 48 h of interaction. Samples were stained by Gram. Monoculture of *C. neoformans*. Scale bar 20 μm. (B) Monoculture of *S. marcescens*. (C) Co-culture of *C. neoformans* and *S. marcescens*. Dashed arrow pointing to cells with morphological alterations and normal arrow pointed to normal fungal cells. Scale bar 10 μm. (D) Quantification of biofilm formation of *Cn* strain B3501 and *Sm* were grown individually or mixed (1:1) in microplate at 37 °C for 48 h and quantified with Crystal Violet method. Results of three independent experiments. (E) Fluorescence detection of *C. neoformans* biofilm co-incubated (1:1) with bacteria using the fluorescent mutant *Cn B3501F*. Experiment was performed three times. *P*-value significance was calculated by Student's *t*-test. Data obtained by SpectraMax i3. ***$P < 0.001$; *$P < 0.05$. (For interpretation of the references to color/colour in this figure legend, the reader is referred to the Web version of this article.)

that targeting virulence determinants may provide new opportunities for antifungal therapy (Clatworthy et al., 2007), we first explored the biofilm formation of *C. neoformans* strain B3501 (strong biofilm-forming) when mixed with *Sm*. Cultures were grown individually or together in RPMI-1640. Association with *Sm* showed a significant decrease on biofilm formation after 48 h of co-cultivation in comparison to the yeast alone (Fig. 1D). This negative outcome was confirmed using the fluorescent mutant H99F which revealed the reduced presence of yeast within the mixed biofilm (Fig. 1E).

### 3.3. *Inhibition of cryptococcal capsule by* S. marcescens

Since *S. marcescens* demonstrated a negative effect on *Cn* biofilm formation, we hypothesized that other virulence-determinant characteristics of yeast pathogenicity would also be attenuated. Given this need to characterize the resulting phenotypes of polymicrobial interactions we investigated polysaccharide capsule production, urease enzyme secretion and melanization. Capsule is considered the most explored determinant of *Cn* (O'Meara and Alspaugh, 2012). It is composed of glucuronoxylomannan (GXM) which is also found in the biofilm matrix and plays a relevant role during the cryptococcal infection (Araújo et al., 2016; Vecchiarelli, 2000). Consequently, this determinant has become an important target in the prevention or treatment of cryptococcosis. Thus, a capsule induction experiment using fetal calf serum (FCS) was performed according to Mayer and Kronstad (2017) protocol . As observed in Fig. 2A–B, a significant decrease in polysaccharide capsule thickness was observed.

### 3.4. *Cell wall integrity*

The integrity of the cell wall of *Cn* was evaluated in order to verify the damage of the bacteria and if there was a defect in the capsule attachment to the cell wall during the interaction. The results of a quantification of GXM assay revealed that the *Cn* culture resulted in the decrease of the secretion of GXM (Fig. 3C). In addition, even though the concentration of the polysaccharide is normalized by the number of cells of *C. neoformans*, the result revealed that there was alteration.

Confocal microscopy was performed to correlate the capsule formation and quantification of GXM assays with an overview of *Cn* cell components by fluorescence. Blue-stained regions (MAb 18B7) represent the capsule, while blue-stained regions (calcofluor) indicate cell wall or capsule polysaccharides. As shown in Fig. 3A–B, the production of capsule of *C. neoformans* was reduced when interacted with the bacteria, as expected according to other experiments, and the cell wall, indicating that the chitinases of *S. marcescens* could influence on integration of calcofluor on cell wall or it could have had a defect in its formation.

### 3.5. *The anti-melanization activity of* S. marcescens

Next, we verified the fungal melanin production under mono and co-cultures. Melanin is a pigment present on cell wall and has physicochemical properties related to protection from antimicrobial molecules and antioxidation (Cordero et al., 2017). *Cn* and *Sm* strains grew alone and in contact with each other on filter-sterilized L-DOPA agar (a melanization-inductive medium) for 48 h. Brown pigmentation in the colonies suggests melanin production. We found that the bacteria caused a reduction on cryptococcal colony melanization, due to the appearance of a light brown color in the center (Fig. 2C).

### 3.6. *Cryptococcal urease is inhibited during interaction with* S. marcescens

After we found the reduction of important virulence determinants by bacteria such as biofilm and capsule formation, we focused on its influence on fungal urease enzyme release. Urease facilitates invasion and dissemination of *Cn* cells across the blood–brain barrier through the hydrolysis of urea into ammonia (Fu et al., 2018; Singh et al., 2013), increasing pH levels and allowing their transmigration in Trojan Horse mechanism (Santiago-Tirado et al., 2017; Sorrell et al., 2016). We therefore co-incubated both fungal and bacterial cultures into Urea broth, a medium that promotes the visualization of the release of urease by color alteration. Interaction with *Sm* demonstrated significant reduction on enzyme secretion (Fig. 2D), confirming the capacity of competing bacteria in disarming multiple virulence determinants in yeasts. Furthermore, it can be seen that viability of Cn decreases drastically when co-cultivated in a medium which induces production of urease with Sm in relation to the pure culture (Fig. 2E).

### 3.7. C. neoformans' *colony is predated and engulfed by* S. marcescens

Another form of microbial organization found in nature is colony biofilms. The study of these systems allows the spatial characterization and evaluation of eco-evolutionary dynamics (Nadell et al., 2016), including the multi-species interactions. The colonies can serve as a protection strategy against harmful agents. To verify the antagonism from another perspective between *Cn* and *Sm*, we performed a real time scanner-based time-lapse to explore interspecies interactions by growing colonies onto solid medium.

Fungal and bacterial prewashed monocultures were inoculated side by side and a scanner registered the entire event for 48 h. Upon first contact, the bacteria began to expand around the fungal colony (Fig. 4). This engulfment became apparent between 12 h and 24 h of inoculation but *Cn* continued to grow despite the apparent predation of the bacteria (Movie S1). Previous studies demonstrated that the antagonistic behavior could be changed by neighboring colonies (Kinkel et al., 2014; Rosenberg et al., 2016). We repeated the experiment using the mutant *H99F* to detect only *Cn*. Colonies in direct contact and fungi-bacteria mixture were cultivated for 48 h. As shown in Fig. 5, no yeast was detected in the mixed colony (Fig. 5D) but in contact, there was a higher concentration of *Cn* cells opposed to the neighboring colony (Fig. 5E). Moreover, when the colonies were cut with a coverslip, cryptococcal cells (left side) can be seen meeting the surface of bacterial colony (right side) in Fig. S2.

Supplementary data related to this article can be found at https://doi.org/10.1016/j.funbio.2020.03.004.

For another complex and spatial perspective of the colonies, we analyzed the antagonistic interaction by scanning electron microscopy. Bacterial and fungal strains were cultivated at the same conditions as described above. As expected, the microorganisms were clearly distinguished from each other. Surprisingly, it was possible to identify both of them in the center of the fungal colony (Fig. 6A–B) but only *Sm* was detected in the edge of the colony interaction, opposite side of the Sm colony; clearly engulfing *Cn* (Fig. 6C–D).

### 3.8. *The percentage of survival of* S. marcescens *increases faster than* C. neoformans

Microbial proliferation is extremely necessary in the competition for limited space and nutrients in the wild. To compare whether the competition affects cell viability, a CFU counting of the

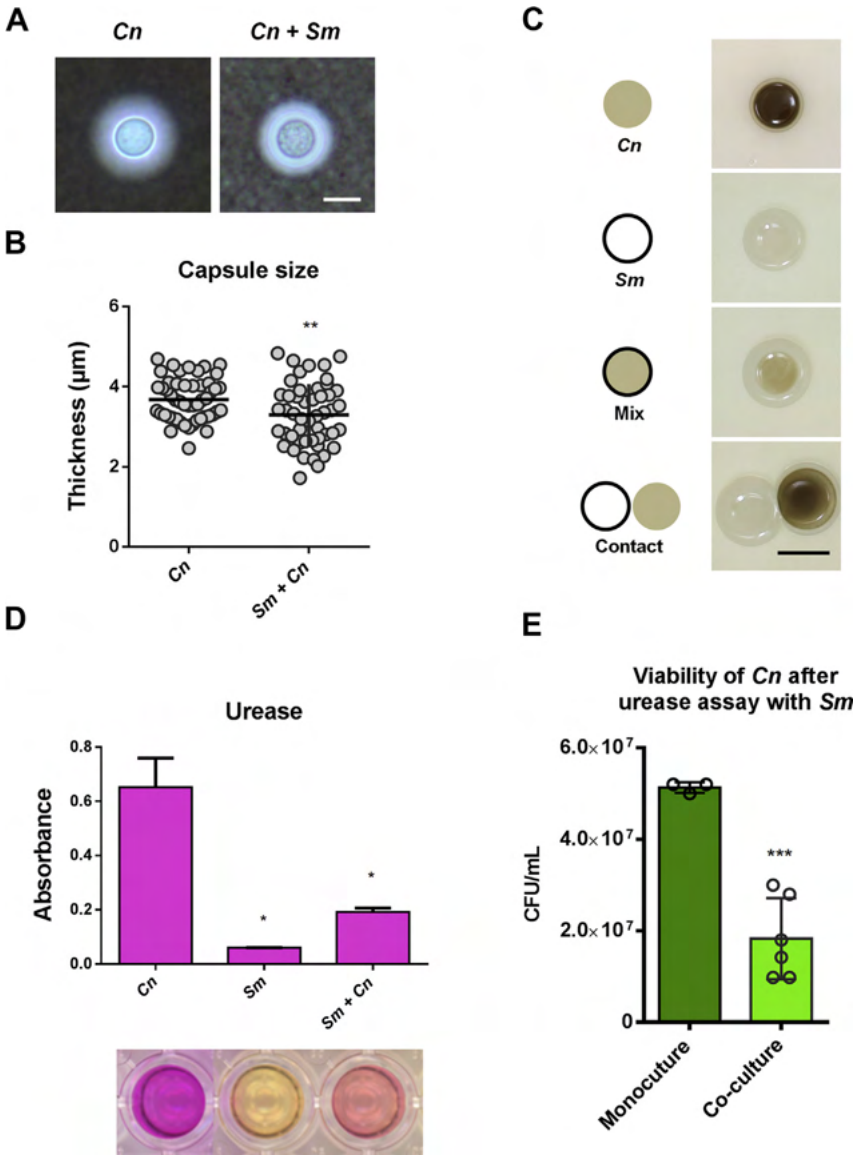


**Fig. 2.** Modulation of virulence determinants of the pathogen *Cn* by *Sm*. (A) Light microscopy of *Cn* strain H99 cells after co-cultivation with *Sm*. Evaluation of bacterial effect on yeast polysaccharide capsule formation. Bacterial and fungal cultures were incubated alone or mixed in fetal calf serum at 30 °C for 72 h. Scale bar 5 μm. (B) Fungal cell capsule thickness measurements. Fifty cells at each condition were analyzed. *P*-value significance was calculated by Student's *t*-test. (C) Antimelanization effect resulted from antagonistic interaction of fungal and bacterial strains. Cultures of *C. neoformans* strain H99 were grown mixed or aside to the competing colony in L-DOPA agar in order to stimulate melanin production (D) Quantification of *Cn* urease production isolated or co-incubated with *Sm* (1:1) in Urea broth. After 6 h of shaking at 37 °C, the absorbance at $OD_{560\ nm}$ was read. Pink color represented the product of urea hydrolysis, indicating urease production. (E) Cell viability of C. neoformans in monoculture and after interaction with the bacteria. Scale bar 0.5 cm. $^{**}P < 0.01$; $^{*}P < 0.05$. (For interpretation of the references to color/colour in this figure legend, the reader is referred to the Web version of this article.)

fungal and bacterial cultures co-cultivated with each other was performed (Abdulkareem et al., 2015). Our results demonstrated that *Sm* displayed higher survival percentage than *Cn*, suggesting that Sm, in addition to predating the competing cells, proliferates faster after 2 h of bacterial–fungal interaction in comparison to the monocultures (Fig. 7). In summary, the dual-species interaction enhances drastically *Sm* replication (Shatzkes et al., 2016).

## 4. Discussion

Microbial communities are commonly found in nature as biofilms. The polysaccharide matrix of biofilms is responsible for community coalescence and protection from antimicrobial agents and also from the host immune system (Beloin et al., 2014). Previous studies have shown that biofilms are responsible for 80% of infectious diseases in animals and humans (Abdullahi et al., 2016). In addition, about 61% of biofilm infections in humans are transmitted by animals, highlighting the importance of their study in medicine (Garcia and Percival, 2011). The social interactions between microorganisms in these systems are related to intercellular communication (Flemming et al., 2016) and consequently increase the metabolic flexibility of the community and its structure. It is possible to classify these interplays from their phenotypic effect on the population. Microorganisms are capable of altering the virulence determinants of pathogen and can thus influence the functions of the community they inhabit (Dhamgaye et al., 2015). Many studies have shown the occurrence of competitive behavior in interactive multi-species communities. These interactions can lead to evolutionary strategies such as rapid proliferation and

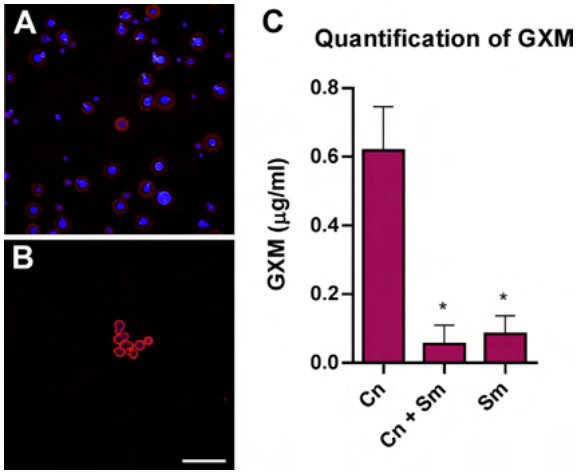


**Fig. 3.** Evaluation of the cell wall of *C. neoformans*. (A) Confocal microscopic images of *C. neoformans* strain H99 cells. Samples and inoculated $1 \times 10^6$ cells/mL in FCS and incubated for 48 h at 37 °C. The plate was incubated with 5 µg/mL of WGA, followed by 5 µg/mL of calcofluor and 10 µg/mL of 18B7 at 37 °C for 30 min. Then it was incubated with secondary antibody IgG and placed on a microscope slide. The red color represents the production of capsule of C. neoformans, whereas the blue color represents the cell wall. (B) Reduction of capsule after interaction with *Sm* and cell wall production. (C) Quantification of GXM by ELISA. Cells were incubated in fetal calf serum (FCS) at $2 \times 10^7$ cells/mL for 48 h. Concentration of GXM in each condition was normalized by the number of cells. Scale bar 40 µm. $^{**}P < 0.01$. P-value significance was calculated by Student's *t*-test. (For interpretation of the references to color/colour in this figure legend, the reader is referred to the Web version of this article.)

metabolites that negatively affect competitor strains (Ghannoum, 2016). Dealing with these competitive strategies is extremely necessary.

*Cn* is an encapsulated pathogen that causes life-threatening meningoencephalitis worldwide. In the wild, it can be found linked to pigeon excreta, however, the animal is not affected by yeast. This statement suggests that the gastrointestinal tract of pigeons may have fungicidal activity (Mayer and Kronstad, 2019a). Also, it was already reported that avian macrophages its higher body temperature can suppress the growth of cryptococcal cells (Johnston et al., 2016). An important aspect to be explored would be the importance of interactions of avian microbiota in cryptococcosis.

In this paper, we approach this perspective of fungal–bacterial associations of components found in the same medium. For this, we isolated bacteria from pigeon excreta in Porto Alegre, RS, Brazil, for exploratory studies of polymicrobial interactions with *Cn*. One bacterium stood out for its antagonistic behavior with the fungus, as demonstrated in the colony interaction and virulence determinant modulation experiments. The bacteria *Sm* is usually found in the environment, but can be considered an opportunistic pathogen in cases of nosocomial infections (Szewzyk et al., 1993). In this study, an anticryptococcal activity on the interactions between these two microorganisms was observed; this emphasizes the concept that specialized avian microbiota can protect bird against pathogen infections.

Light microscopy demonstrated that the bacteria caused morphological changes in several *Cn* cells, so that they appeared to be degraded. However, the percent cell survival experiment revealed that there was no change in the number of fungal cells after interaction. Experiments were performed to verify whether some virulence determinants of pathogenic yeast would be altered during co-cultivation with *Sm*. Among them, biofilm formation, urease secretion, capsule formation and melanization were evaluated. The results showed that the bacteria were able to drastically reduce all the tested virulence determinants of *Cn*. In fact, the integrity of the cell wall was verified and it was compromised. The inhibition of biofilm caused by the interaction could be due to the bacterial blockage by the fungus on adhering to the substrate or even by the secretion of antifungal molecules (James et al., 1995). These findings evidence that competition in co-cultures can result in dominance by one species, while the competing group persists in the medium.

Interactions with colonies in solid medium were also performed. Real time scanner-based time lapse displayed the engulfment of fungal colony by bacterial colony and its retraction

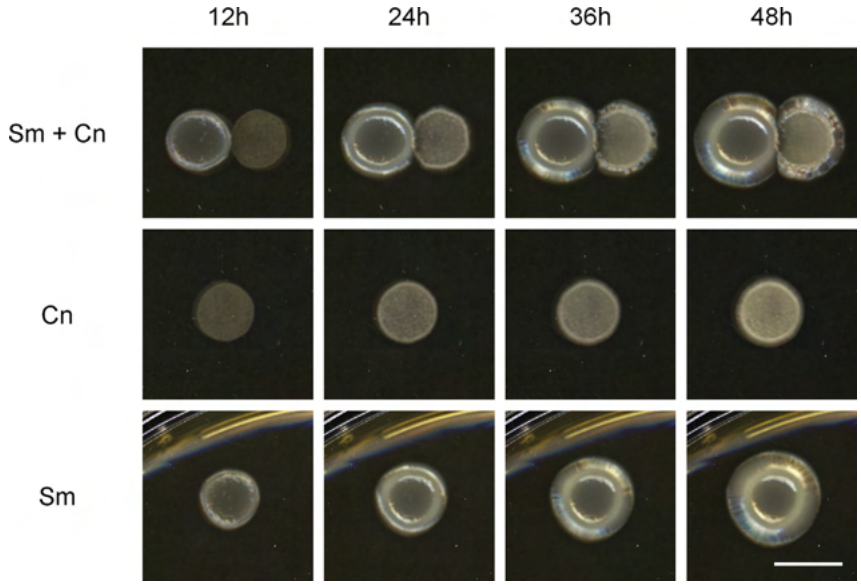


**Fig. 4.** Isolated and in contact colonies of *C. neoformans* and *S. marcescens* onto YPD agar. Real time scanner-based time lapse showed fungal colony engulfment by bacteria after 12 h of inoculation and yeast remoteness to the opposite side of contact zone between 24 and 48 h. Scale bar 0.5 cm.

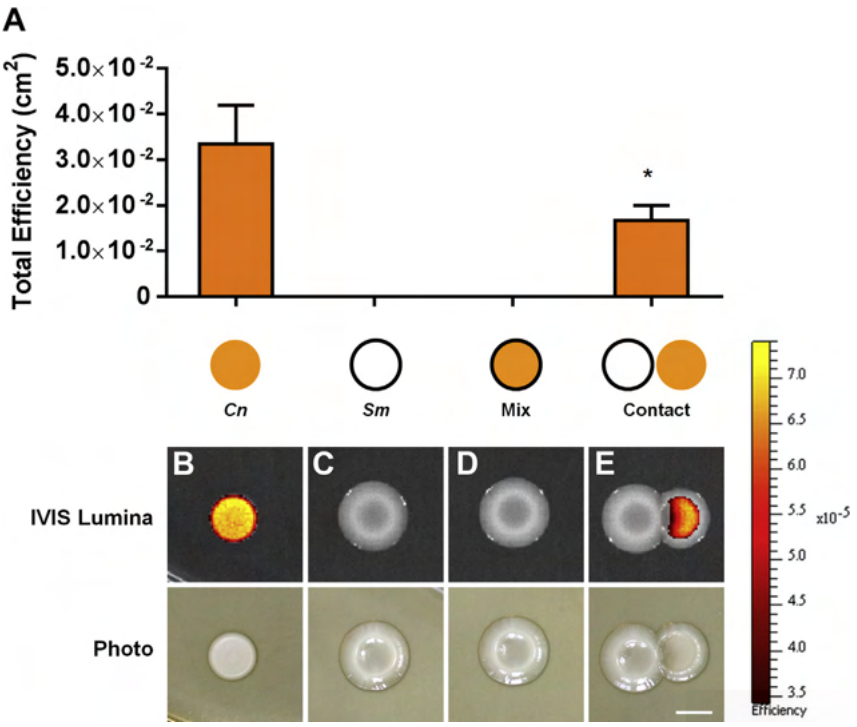


**Fig. 5.** *Cn* detection using the fluorescent mutant *H99F* after cultivation with *Sm* (A) Quantification of colonies fluorescence. (B–E) Pictures taken by IVIS Lumina of antagonistic interaction onto YPD medium after 48 h of incubation. (B) *Cn* monoculture. (C) *Sm* monoculture. (D) Bacterial and yeast colonies in contact, respectively. Scale bar 0.5 cm. $*P < 0.05$. *P*-value significance was calculated by Student's *t*-test.

to the other side. Although this antagonistic phenotype was present, *Cn* colony was resistant to the threat. For this, analyzes were performed using fluorescent mutant to detect yeast and scanning electron microscopy to visualize the interaction in more detail.

In conclusion, this research allowed the physiological characterization of the antagonist interaction between two pigeon droppings cohabiting microorganisms. Understanding mechanisms of competition assist in the determination of the morphology and functions of a community. Studies on multi-species interactions may provide new strategies for antifungal therapy and development of probiotics to treat infections. Our results evidence the complexity of interspecies interactions, especially when it comes to competition with a pathogen.

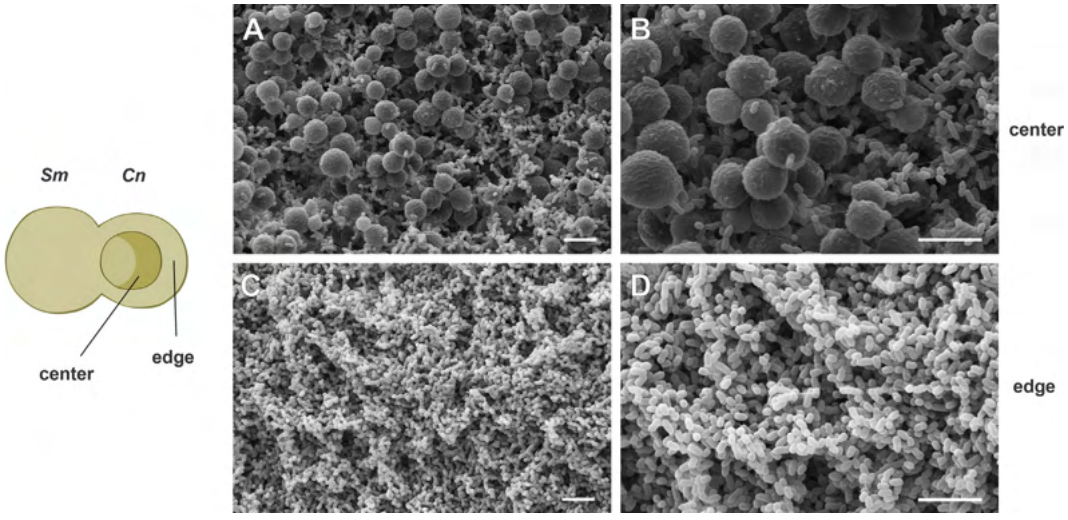


**Fig. 6.** Images of scanning electron microscopy showing details of *Cn* colony at the center and edge after interaction with *S. marcescens*. Colonies were grown at 37 °C for 48 h. (A–B) Center of the yeast colony showing the presence of both species. (C–D) Colony edge indicating only the presence of bacteria. Scale bar 0.5 μm.

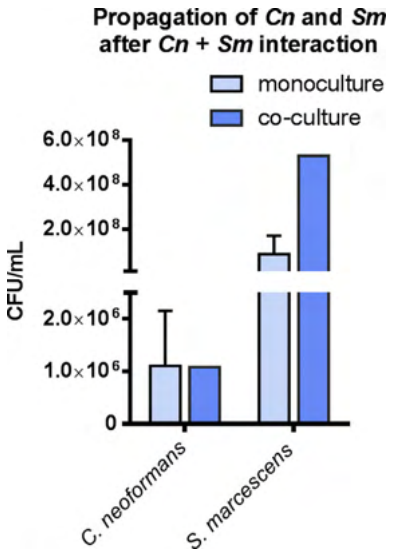


**Fig. 7.** Cell viability of *Sm* was higher than *C. neoformans* after co-cultivation. Percent survival was determined by incubating mixed cultures for 2 h following CFU counting. Monocultures were used as controls. Experiment was performed three times independently. $^{**}P < 0.01$. *P*-value significance was calculated by Student's *t*-test.

## Conflicts of interest

The authors declare no conflict of interest.

## Acknowledgments

We thank Arturo Casadevall for providing the antibody to GXM (MAb 18B7). This research was funded by grants from the Brazilian agencies Conselho Nacional de Desenvolvimento Científico e Tecnológico (CNPq) and Coordenação de Aperfeiçoamento de Pessoal do Ensino Superior (CAPES). WL, AS and MHV have been supported by CNPq grants 142287/2017-2, 302637/2017-6 and 307191/2016-8, respectively.

## Appendix A. Supplementary data

Supplementary data to this article can be found online at https://doi.org/10.1016/j.funbio.2020.03.004.

## References

Abdulkareem, A.F., Lee, H.H., Ahmadi, M., Martinez, L.R., 2015. Fungal serotype-specific differences in bacterial–yeast interactions. Virulence 6, 652–657.
Abdullahi, U.F., Igwenagu, E., Mu'azu, A., Aliyu, S., Umar, M.I., 2016. Intrigues of biofilm: a perspective in veterinary medicine. Vet. World 9, 12–18.
Araújo, G.R., Fontes, G.N., Leão, D., Rocha, G.M., Pontes, B., Sant'Anna, C., de Souza, W., Frases, S., 2016. *Cryptococcus neoformans* capsular polysaccharides form branched and complex filamentous networks viewed by high-resolution microscopy. J. Struct. Biol. 193, 75–82.
Beloin, C., Renard, S., Ghigo, J.M., Lebeaux, D., 2014. Novel approaches to combat bacterial biofilms. Curr. Opin. Pharmacol. 18, 61–68.
Camacho, E., Casadevall, A., 2018. Cryptococcal traits mediating adherence to biotic and abiotic surfaces. J. Fungi (Basel) 4.
Chitty, J.L., Edwards, D.J., Robertson, A.A.B., Butler, M.S., Duley, J.A., Cooper, M.A., Fraser, J.A., 2019. Quantitation of Purines from pigeon guano and implications for *Cryptococcus neoformans* survival during infection. Mycopathologia 184 (2), 273–281.
Christensen, G.J., Scholz, C.F., Enghild, J., Rohde, H., Kilian, M., Thürmer, A., Brzuszkiewicz, E., Lomholt, H.B., Brüggemann, H., 2016. Antagonism between *Staphylococcus epidermidis* and *Propionibacterium acnes* and its genomic basis. BMC Genom. 17, 152.
Clatworthy, A.E., Pierson, E., Hung, D.T., 2007. Targeting virulence: a new paradigm for antimicrobial therapy. Nat. Chem. Biol. 3, 541–548.
Cordero, R.J.B., Robert, V., Cardinali, G., Arinze, E.S., Thon, S.M., Casadevall, A., 2018. Impact of yeast pigmentation on heat capture and latitudinal distribution. Curr. Biol. 28, 2657–2664 e2653.
Cordero, R.J.B., Vij, R., Casadevall, A., 2017. Microbial melanins for radioprotection and bioremediation. Microb. Biotechnol. 10, 1186–1190.
Dhamgaye, S., Murray, G.L., Peleg, A.Y., 2015. The influence of bacterial interaction on the virulence of *Cryptococcus neoformans*. Virulence 6, 677–678.
Flemming, H.C., Wingender, J., Szewzyk, U., Steinberg, P., Rice, S.A., Kjelleberg, S., 2016. Biofilms: an emergent form of bacterial life. Nat. Rev. Microbiol. 14, 563–575.
Friedman, J., Gore, J., 2017. Ecological systems biology: the dynamics of interacting populations. Curr. Opin. Syst. Biol. 1, 114–121.
Fu, M.S., Coelho, C., De Leon-Rodriguez, C.M., Rossi, D.C.P., Camacho, E., Jung, E.H., Kulkarni, M., Casadevall, A., 2018. *Cryptococcus neoformans* urease affects the outcome of intracellular pathogenesis by modulating phagolysosomal pH. PLoS Pathog. 14, e1007144.
Garcia, A.B., Percival, S.L., 2011. Zoonotic infections: the role of biofilms. Biofilms Vet. Med. 69–110.
Ghannoum, M., 2016. Cooperative evolutionary strategy between the bacteriome and mycobiome. mBio 7.
James, G.A., Beaudette, L., Costerton, J.W., 1995. Interspecies bacterial interactions in biofilms. J. Ind. Microbiol. 15, 257–262.
Johnston, S.A., Voelz, K., May, R.C., 2016. *Cryptococcus neoformans* thermotolerance to avian body temperature is sufficient for extracellular growth but not intracellular survival in macrophages. Sci. Rep. 6, 20977.
Kinkel, L.L., Schlatter, D.C., Xiao, K., Baines, A.D., 2014. Sympatric inhibition and niche differentiation suggest alternative coevolutionary trajectories among *Streptomycetes*. ISME J. 8, 249–256.
Kong, E.F., Tsui, C., Kucharíková, S., Andes, D., Van Dijck, P., Jabra-Rizk, M.A., 2016. Commensal protection of *Staphylococcus aureus* against antimicrobials by *Candida albicans* biofilm matrix. mBio 7.
Krasowska, A., Murzyn, A., Dyjankiewicz, A., Łukaszewicz, M., Dziadkowiec, D., 2009. The antagonistic effect of *Saccharomyces boulardii* on *Candida albicans* filamentation, adhesion and biofilm formation. FEMS Yeast Res. 9, 1312–1321.
Kwon-Chung, K.J., Rhodes, J.C., 1986. Encapsulation and melanin formation as indicators of virulence in *Cryptococcus neoformans*. Infect. Immun. 51, 218–223.
Lopes, William, Vainstein, M.H., De Sousa Araujo, G.R., Frases, S., Staats, C.C., de Almeida, R.M.C., Schrank, A., Kmetzsch, L., Vainstein, M.H., 2017. Geometrical distribution of *Cryptococcus neoformans* mediates flower-like biofilm development. Frontiers in Microbiology 8, 1–13. https://doi.org/10.3389/fmicb.2017.02534, 2534. In this issue.
Mahlen, S.D., 2011. Serratia infections: from military experiments to current practice. Clin. Microbiol. Rev. 24, 755–791.
Martinez, L.R., Casadevall, A., 2015. Biofilm formation by *Cryptococcus neoformans*. Microbiol. Spectr. 3.
Mayer, F.L., Kronstad, J.W., 2017. Disarming fungal pathogens: *Bacillus safensis* inhibits virulence factor production and biofilm formation by *Cryptococcus neoformans* and *Candida albicans*. mBio 8.
Mayer, F.L., Kronstad, J.W., 2019a. The spectrum of interactions between *Cryptococcus neoformans* and bacteria. J. Fungi 5, 31.
Mayer, F.L., Kronstad, J.W., 2019b. The spectrum of interactions between *Cryptococcus neoformans* and bacteria. J. Fungi (Basel) 5.
McCully, L.M., Bitzer, A.S., Seaton, S.C., Smith, L.M., Silby, M.W., 2019. Interspecies social spreading: interaction between two sessile soil bacteria leads to emergence of surface motility. mSphere 4.
Moradigaravand, D., Boinett, C.J., Martin, V., Peacock, S.J., Parkhill, J., 2016. Recent independent emergence of multiple multidrug-resistant Serratia marcescens clones within the United Kingdom and Ireland. Genome Res. 26, 1101–1109.
Mulet, M., Gomila, M., Lemaitre, B., Lalucat, J., García-Valdés, E., 2012. Taxonomic characterisation of *Pseudomonas* strain L48 and formal proposal of *Pseudomonas entomophila* sp. nov. Syst. Appl. Microbiol. 35, 145–149.
Nadell, C.D., Drescher, K., Foster, K.R., 2016. Spatial structure, cooperation and competition in biofilms. Nat. Rev. Microbiol. 14, 589–600.
Nai, C., Meyer, V., 2018. From axenic to mixed cultures: technological advances accelerating a paradigm shift in microbiology. Trends Microbiol. 26, 538–554.
Nielsen, K., De Obaldia, A.L., Heitman, J., 2007. *Cryptococcus neoformans* mates on pigeon guano: implications for the realized ecological niche and globalization. Eukaryot. Cell 6, 949–959.
O'Meara, T.R., Alspaugh, J.A., 2012. The *Cryptococcus neoformans* capsule: a sword and a shield. Clin. Microbiol. Rev. 25, 387–408.
Patel, R., 2019. A moldy application of MALDI: MALDI-ToF mass spectrometry for fungal identification. J. Fungi (Basel) 5.
Pavlovic, M., Konrad, R., Iwobi, A.N., Sing, A., Busch, U., Huber, I., 2012. A dual approach employing MALDI-TOF MS and real-time PCR for fast species identification within the *Enterobacter cloacae* complex. FEMS Microbiol. Lett. 328, 46–53.
Rajasingham, R., Smith, R.M., Park, B.J., Jarvis, J.N., Govender, N.P., Chiller, T.M., Denning, D.W., Loyse, A., Boulware, D.R., 2017. Global burden of disease of HIV-associated cryptococcal meningitis: an updated analysis. Lancet Infect. Dis. 17, 873–881.
Ravi, S., Pierce, C., Witt, C., Wormley, F.L., 2009. Biofilm formation by *Cryptococcus neoformans* under distinct environmental conditions. Mycopathologia 167, 307–314.

Rella, A., Yang, M.W., Gruber, J., Montagna, M.T., Luberto, C., Zhang, Y.M., Del Poeta, M., 2012. *Pseudomonas aeruginosa* inhibits the growth of *Cryptococcus* species. Mycopathologia 173, 451–461.

Rosenberg, G., Steinberg, N., Oppenheimer-Shaanan, Y., Olender, T., Doron, S., Ben-Ari, J., Sirota-Madi, A., Bloom-Ackermann, Z., Kolodkin-Gal, I., 2016. Not so simple, not so subtle: the interspecies competition between *Bacillus simplex* and *Bacillus subtilis* and its impact on the evolution of biofilms. NPJ Biofilms Microbiomes 2, 15027.

Røder, H.L., Sørensen, S.J., Burmølle, M., 2016. Studying bacterial multispecies biofilms: where to start? Trends Microbiol. 24, 503–513.

Saito, F., Ikeda, R., 2005. Killing of *Cryptococcus neoformans* by *Staphylococcus aureus*: the role of cryptococcal capsular polysaccharide in the fungal–bacteria interaction. Med. Mycol. 43, 603–612.

Santiago-Tirado, F.H., Onken, M.D., Cooper, J.A., Klein, R.S., Doering, T.L., 2017. Trojan horse transit contributes to blood–brain barrier crossing of a eukaryotic pathogen. mBio 8.

Shatzkes, K., Singleton, E., Tang, C., Zuena, M., Shukla, S., Gupta, S., Dharani, S., Onyile, O., Rinaggio, J., Connell, N.D., Kadouri, D.E., 2016. Predatory bacteria attenuate *Klebsiella pneumoniae* burden in rat lungs. mBio 7.

Singh, A., Panting, R.J., Varma, A., Saijo, T., Waldron, K.J., Jong, A., Ngamskulrungroj, P., Chang, Y.C., Rutherford, J.C., Kwon-Chung, K.J., 2013. Factors required for activation of urease as a virulence determinant in *Cryptococcus neoformans*. mBio 4 e00220-00213.

Sorrell, T.C., Juillard, P.G., Djordjevic, J.T., Kaufman-Francis, K., Dietmann, A., Milonig, A., Combes, V., Grau, G.E., 2016. Cryptococcal transmigration across a model brain blood-barrier: evidence of the Trojan horse mechanism and differences between *Cryptococcus neoformans* var. *grubii* strain H99 and *Cryptococcus gattii* strain R265. Microbes Infect. 18, 57–67.

Szewzyk, U., Szewzyk, R., Stenström, T.A., 1993. Growth and survival of *Serratia marcescens* under aerobic and anaerobic conditions in the presence of materials from blood bags. J. Clin. Microbiol. 31, 1826–1830.

Toffaletti, D.L., Rude, T.H., Johnston, S.A., Durack, D.T., Perfect, J.R., 1993 Mar. Gene transfer in Cryptococcus neoformans by use of biolistic delivery of DNA. J. Bacteriol. 175 (5), 1405–1411.

Tomičić, Z., Zupan, J., Matos, T., Raspor, P., 2016. Probiotic yeast *Saccharomyces boulardii* (nom. nud.) modulates adhesive properties of *Candida glabrata*. Med. Mycol. 54, 835–845.

Vecchiarelli, A., 2000. Immunoregulation by capsular components of *Cryptococcus neoformans*. Med. Mycol. 38, 407–417.

## **3.4 Capítulo IV:** Allee effects underly multistability in the nasal microcosm.

Manuscrito em preparação, referente ao período sanduíche no GoreLab.

Participação no Trabalho: Concepção do estudo, desenho experimental, execução dos experimentos, análise interpretação de dados e redação da primeira versão do manuscrito.

# 4 DISCUSSÃO GERAL

A complexidade dos sistemas microbianos pode ser comparada mediante dois parâmetros principais: a composição da comunidade e a estrutura do meio ambiente. Isto é, se o número de espécies na comunidade aumenta, a rede de interações torna–se mais complexa. Também, conforme a complexidade do meio ambiente aumenta, o sistema pode gerar padrões de interação antes inexistentes[55]. Na prática, isso significa dizer que a complexidade das interações aumenta de ambientes líquidos para ambientes sólidos, bem como de monoculturas para comunidades mistas. De fato, quando dois microrganismos competem em meio sólido, como quando ágar é um componente, padrões de segregação populacional na colônia mista podem observados [56]. Essa classificação de complexidade é o ponto de partida para discutir a cronologia dos estudos desta tese.

Em *Cryptococcus* spp., a presença de comunicação celular pode ser mediada por fatores como: vesículas extracelulares[57], moléculas *quorum sensing*[58], componentes capsulares[59] e proteínas secretadas[60]. Como consequência, há possibilidade de heterogeneidade funcional, incluindo: dormência, plasticidade fenotípica, formação de biofilme, entre outros.

As populações clonais estão entre os sistemas mais simples que podem ser explorados. Ainda assim, são governadas por uma miríade de fatores que impactam a dinâmica intraespecífica, tanto em biofilmes quanto em suspensão. A formação de

biofilme por *C. neoformans* demonstra padrões de interação coletiva bastante ordenados, demonstrados no capítulo I. Esses padrões foram identificados em fases distintas: (*i*) no início, em que a distribuição geométrica das células em superfície é importante para as etapas subsequentes da formação de biofilme, (*ii*) na maturação, em que a ultraestrutura *flower–like,* foi observada em associação com as células formadoras (células adjacentes ao *cluster*, por exemplo) e (*iii*) na dispersão, em que a motilidade passiva em *C. neoformans* foi demonstrada na comunidade. É importante destacar que a motilidade passiva em comunidades é um padrão evolutivo de interação que emerge como solução à ausência de motilidade ativa ou às dificuldades impostas por elevadas densidades populacionais em um sistema[6].

Populações clonais também podem apresentar alterações morfológicas, embora sejam menos exploradas pela dificuldade de detecção e consequentemente análises estatísticas. As principais alterações morfológicas descritas em *Cryptococcus* spp. incluem: alterações de superfície celular e alterações no tamanho da célula. No capítulo II, a detecção de diferentes morfotipos foi aprofundada mediante a utilização de microscopia eletrônica de varredura de alta resolução. Foram observados 4 morfotipos frequentemente distribuídos entre os 11 isolados analisados. A implementação de uma *pipeline* de análise de imagem automatizada permitiu a classificação automatizada desses morfotipos alternativos em *Cryptococcus* e também a seleção de características importantes para essa

diferenciação. Os mecanismos que regulam essas alterações são conhecidos apenas parcialmente e em morfotipos estudados há mais tempo, como células Titãs[61, 62].

Além das alterações observadas em comunidades clonais, fenótipos competitivos podem estar presentes em colônias de microrganismos. De fato, a surpreendente capacidade de *S. marcescens* migrar sob a colônia de *C. neoformans* e causar dano é uma clara demonstração de um fenótipo competitivo, como demonstrado no capítulo III. Presumidamente, essa interação deveria promover a coexistência dos dois microrganismos pois coabitam o mesmo nicho; o que não acontece. Assumindo o resultado encontrado, a pergunta poderia ser: porque essa competição ocorre? Ou porque *S. marcescens* é mais agressiva que *C. neoformans*? As forças por trás das interações competitivas são manifestadas em três situações principais: (*i*) quando as espécies têm preferência por nutrientes similares; (*ii*) quanto as espécies estão misturadas em um mesmo ambiente onde nutrientes e metabólitos são compartilhados e (*iii*) quando a densidade celular é maior do que a disponibilidade de recursos[56].

Ainda que *C. neoformans* seja inibido por *S. marcescens* isso não significa que em um ambiente colonizado por múltiplas espécies isso seja regra. Na presença outras espécies, forças estabilizadoras podem surgir em algumas interações[63]. Por exemplo, se em um mesmo ambiente *C. neoformans* coexistir com uma espécie que exclua *S. marcescens*, a chance de *Cryptococcus* colonizar o ambiente é aumentada

(Figura 4). Essa rede de interações tem grande relevância em ambientes onde patógenos e comensais estão frequentemente em contato.

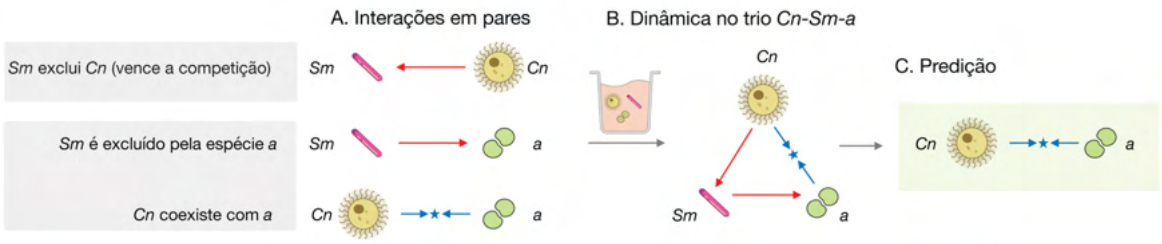


**Figura 5**| Demonstração esquemática da interação *Serratia marcescens–Cryptococcus neoformans* (*Sm–Cn*) na presença de um invasor *a.* (A) Interações em pares de espécies resulta em regimes distintos. (B) Topologia do trio composto por *Cn–Sm–a.* (C) A predição da comunidade resulta em coexistência entre *Cn–a.* Essa predição é fundamentada em regras de montagem de comunidades anteriormente publicadas[28].

A microbiota de humanos e outros hospedeiros é composta por diversos microrganismos pertencentes a distintos reinos, e a complexidade de interações nesses ambientes pode determinar trajetória e montagem de comunidades. Por exemplo, no intestino infantil foi demostrado que a microbiota é estabelecida a partir da colonização pioneira por alguns microrganismos. Também foi demonstrado que interações diretas entre diferentes reinos fundamenta a dinâmica nesse sistema. Destaca-se que o gênero *Cryptococcus* foi o mais abundante em 5% das amostras analisadas[64].

A motivação do estudo apresentado no capítulo IV foi entender como ocorre a regulação e dinâmica de comunidades microbianas relevantes para o sistema respiratório, especificamente a cavidade nasal. Esse ambiente foi escolhido por ser

o sítio anatômico primário de invasão, ou ambiente de latência, do modelo escolhido nesse estudo. Dessa forma, a hipótese considera que interações podem ser determinantes na exclusão ou colonização de *C. neoformans* no microcosmo nasal. Também foram estudados os efeitos de variações de pH, dentro da faixa fisiológica, na transição de regimes de interação. Esse capítulo adicionou uma substancial complexidade em relação ao estudo anterior: a dinâmica de comunidades foi explorada a partir de 8 microrganismos, que corresponderam a 28 pares propagados em diferentes condições até o equilíbrio.

Os resultados demostraram a existência de comunidades que são governadas por dois mecanismos distintos: (*i*) resposta a modificações ambientais, em que diferentes comunidades são geradas a partir de mudanças de pH, como no par *Burkholderia cenocepacia – Klebsiella pneumoniae*; e (*ii*) multiestabilidade, em que uma comunidade pode adotar composições diferentes na mesma condição ambiental (Figura 6). Comunidades com estados alternativos foram observados entre o subgrupo formado por: *Moraxella catarrhalis*, *Staphylococcus aureus*, *Staphylococcus epidermidis* e *C. neoformans*.

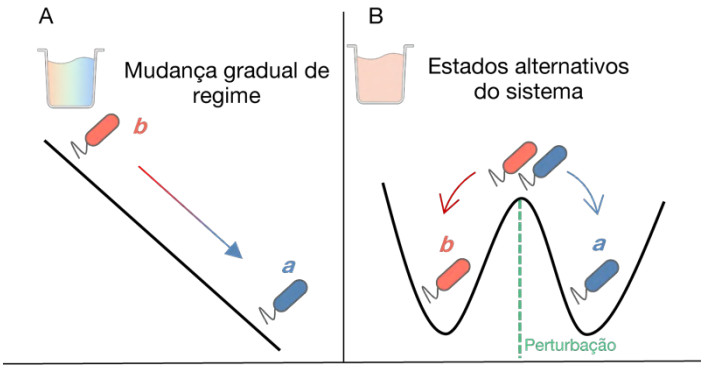


**Figura 6**| Transições em sistemas microbianos. Diferentes tipos de comunidades podem ser gerados a partir de (A) mudanças lineares, como as causadas por gradientes em um sistema; ou ainda transições que geram estados alternativos de equilíbrio que são de difícil reversão (B). Estados alternativos de equilíbrio incluem bistabilidade (em pares de espécies) ou multiestabilidade em sistemas com maior número de espécies .

Os resultados desse estudo demonstram que efeitos Allee e mudança de pH pelas espécies são direcionadores de estados de equilíbrio alternativos no subgrupo de espécies selecionado e podem explicar diversidade tanto no hospedeiro humano quanto na natureza. Destaca-se a interação no trio *C. neoformans, Staphylococcus epidermidis e Moraxella catarrhalis*, em que a presença de *S. epidermidis* como residente facilita a invasão de *M. catarrhalis* mesmo na presença de seu competidor *C. neoformans*.

A descoberta de multistabilidade em comunidades clinicamente relevantes, pode trazer luz à questionamentos com respostas ainda incompletas, como: Porque indivíduos saudáveis apresentam maior susceptibilidade a processos infeciosos do que outros? Se uma comunidade microbiana é multiestável, as forças de interação podem ser determinantes e as diferenças entre fatores ambientais e genéticos em

hospedeiros têm menor impacto, pois o estado de equilíbrio da comunidade pode ser consequência de eventos passados e não necessariamente de diferenças entre hospedeiros [65]. Isso porque uma das propriedades de multistabilidade é histerese: a tendência de um sistema conservar as suas propriedades após uma perturbação, ou ainda, preservar uma deformação estrutural[66]. A prova de conceito de estados alternativos (bistabilitade) em humanos foi demonstrada no sistema intestinal em um estudo com mais de 1000 adultos. Os autores identificaram distribuições bimodais na microbiota que não estão relacionadas com mudanças da dieta a curto prazo[67].

Dessa forma, elucidar os mecanismos que governam diferentes tipos de comunidades, bem como identificar microrganismos que interagem fortemente gerando estados alternativos constituem tópicos promissores em microbiologia integrativa.

# 5 CONCLUSÃO

Microrganismos demonstram fenótipos cooperativos e competitivos que permitem a colonização na natureza e no hospedeiro. O comportamento de uma célula pode impactar a divisão e sobrevivência de células adjacentes, em uma demonstração de traços sociais dentro da perspectiva evolutiva. Nesse contexto, o patógeno *Cryptococcus* spp. é um modelo de estudo que permite explorar comportamentos sociais orquestrados para garantir sua sobrevivência em diferentes ambientes: de comunidades clonais estruturadas a redes de interações intraespecíficas.

Este estudo demonstrou que a organização espacial de células é uma etapa importante para a formação de biofilme. Também, demonstramos morfotipos celulares presentes em uma mesma população clonal e implementamos uma *pipeline* automatizada que pode auxiliar estudos futuros na identificação e caracterização funcional dessas populações. Por fim, elucidamos a dinâmica que regula a montagem de comunidades associadas à microbiota nasal e o impacto de gradientes fisiológicos nessas populações.

# 6 REFERÊNCIAS


1. West SA, Griffin AS, Gardner A, Diggle SP. Social evolution theory for microorganisms. *Nat Rev Microbiol*. Aug 2006;4(8):597-607. doi:10.1038/nrmicro1461

2. Ratzke C, Gore J. Shaping the Crowd: The Social Life of Cells. *Cell Syst*. Nov 25 2015;1(5):310-2. doi:10.1016/j.cels.2015.11.005

3. Cornforth DM, Foster KR. Competition sensing: the social side of bacterial stress responses. *Nat Rev Microbiol*. 04 2013;11(4):285-93. doi:10.1038/nrmicro2977

4. Ratzke C, Gore J. Modifying and reacting to the environmental pH can drive bacterial interactions. *PLoS Biol*. 03 2018;16(3):e2004248. doi:10.1371/journal.pbio.2004248

5. Estrela S, Libby E, Van Cleve J, et al. Environmentally Mediated Social Dilemmas. *Trends Ecol Evol*. 01 2019;34(1):6-18. doi:10.1016/j.tree.2018.10.004

6. Meacock OJ, Doostmohammadi A, Foster KR, Yeomans JM, Durham WM. Bacteria solve the problem of crowding by moving slowly. *Nature Physics*. 2021/02/01 2021;17(2):205-210. doi:10.1038/s41567-020-01070-6

7. Greig D, Travisano M. The Prisoner's Dilemma and polymorphism in yeast SUC genes. *Proc Biol Sci*. Feb 07 2004;271 Suppl 3:S25-6. doi:10.1098/rsbl.2003.0083

8. Gore J, Youk H, van Oudenaarden A. Snowdrift game dynamics and facultative cheating in yeast. *Nature*. May 14 2009;459(7244):253-6. doi:10.1038/nature07921

9. Becskei A, Séraphin B, Serrano L. Positive feedback in eukaryotic gene networks: cell differentiation by graded to binary response conversion. *EMBO J*. May 15 2001;20(10):2528-35. doi:10.1093/emboj/20.10.2528

10. Dubnau D, Losick R. Bistability in bacteria. *Mol Microbiol*. Aug 2006;61(3):564-72. doi:10.1111/j.1365-2958.2006.05249.x

11. Shoemaker WR, Lennon JT. Evolution with a seed bank: The population genetic consequences of microbial dormancy. *Evol Appl*. 01 2018;11(1):60-75. doi:10.1111/eva.12557

12. Diard M, Garcia V, Maier L, et al. Stabilization of cooperative virulence by the expression of an avirulent phenotype. *Nature*. Feb 21 2013;494(7437):353-6. doi:10.1038/nature11913

13. Balaban NQ, Merrin J, Chait R, Kowalik L, Leibler S. Bacterial persistence as a phenotypic switch. *Science*. Sep 10 2004;305(5690):1622-5. doi:10.1126/science.1099390

14. Van den Bergh B, Fauvart M, Michiels J. Formation, physiology, ecology, evolution and clinical importance of bacterial persisters. *FEMS Microbiol Rev*. 05 01 2017;41(3):219-251. doi:10.1093/femsre/fux001

15. Guzmán-Soto I, McTiernan C, Gonzalez-Gomez M, et al. Mimicking biofilm formation and development: Recent progress in. *iScience*. May 21 2021;24(5):102443. doi:10.1016/j.isci.2021.102443

16. Flemming HC, Wingender J. The biofilm matrix. *Nat Rev Microbiol*. Sep 2010;8(9):623-33. doi:10.1038/nrmicro2415

17. Donlan RM. Biofilms: microbial life on surfaces. *Emerg Infect Dis*. Sep 2002;8(9):881-90. doi:10.3201/eid0809.020063

18. Costerton JW, Lewandowski Z, Caldwell DE, Korber DR, Lappin-Scott HM. Microbial biofilms. *Annu Rev Microbiol*. 1995;49:711-45. doi:10.1146/annurev.mi.49.100195.003431

19. Lewis K. Multidrug tolerance of biofilms and persister cells. *Curr Top Microbiol Immunol*. 2008;322:107-31.

20. Drescher K, Nadell CD, Stone HA, Wingreen NS, Bassler BL. Solutions to the public goods dilemma in bacterial biofilms. *Curr Biol*. Jan 06 2014;24(1):50-55. doi:10.1016/j.cub.2013.10.030

21. Secchi E, Vitale A, Miño GL, et al. The effect of flow on swimming bacteria controls the initial colonization of curved surfaces. *Nat Commun*. 06 05 2020;11(1):2851. doi:10.1038/s41467-020-16620-y

22. Wilking JN, Zaburdaev V, De Volder M, Losick R, Brenner MP, Weitz DA. Liquid transport facilitated by channels in Bacillus subtilis biofilms. *Proc Natl Acad Sci U S A*. Jan 2013;110(3):848-52. doi:10.1073/pnas.1216376110

23. Foster KR, Schluter J, Coyte KZ, Rakoff-Nahoum S. The evolution of the host microbiome as an ecosystem on a leash. *Nature*. 08 02 2017;548(7665):43-51. doi:10.1038/nature23292

24. Man WH, de Steenhuijsen Piters WA, Bogaert D. The microbiota of the respiratory tract: gatekeeper to respiratory health. *Nat Rev Microbiol*. 05 2017;15(5):259-270. doi:10.1038/nrmicro.2017.14

25. Blaser MJ. The microbiome revolution. *J Clin Invest*. Oct 2014;124(10):4162-5. doi:10.1172/JCI78366

26. Faust K, Raes J. Microbial interactions: from networks to models. *Nat Rev Microbiol*. Jul 16 2012;10(8):538-50. doi:10.1038/nrmicro2832

27. Wright ES, Vetsigian KH. Inhibitory interactions promote frequent bistability among competing bacteria. *Nat Commun*. Apr 21 2016;7:11274. doi:10.1038/ncomms11274

28. Friedman J, Higgins LM, Gore J. Community structure follows simple assembly rules in microbial microcosms. *Nat Ecol Evol*. Mar 27 2017;1(5):109. doi:10.1038/s41559-017-0109

29. Smith R, Tan C, Srimani JK, et al. Programmed Allee effect in bacteria causes a tradeoff between population spread and survival. *Proc Natl Acad Sci U S A*. Feb 04 2014;111(5):1969-74. doi:10.1073/pnas.1315954111

30. Enaud R, Vandenborght LE, Coron N, et al. The Mycobiome: A Neglected Component in the Microbiota-Gut-Brain Axis. *Microorganisms*. Mar 9 2018;6(1)doi:10.3390/microorganisms6010022

31. Silva DL, Lima CM, Magalhães VCR, et al. Fungal and bacterial coinfections increase mortality of severely ill COVID-19 patients. *J Hosp Infect*. Jul 2021;113:145-154. doi:10.1016/j.jhin.2021.04.001

32. Kalan L, Loesche M, Hodkinson BP, et al. Redefining the Chronic-Wound Microbiome: Fungal Communities Are Prevalent, Dynamic, and Associated with Delayed Healing. *MBio*. Sep 6 2016;7(5)doi:10.1128/mBio.01058-16

33. Ghannoum M. Cooperative Evolutionary Strategy between the Bacteriome and Mycobiome. *MBio*. Nov 15 2016;7(6)doi:10.1128/mBio.01951-16

34. Oever JT, Netea MG. The bacteriome-mycobiome interaction and antifungal host defense. *Eur J Immunol*. Nov 2014;44(11):3182-91. doi:10.1002/eji.201344405

35. Peleg AY, Hogan DA, Mylonakis E. Medically important bacterial-fungal interactions. *Nat Rev Microbiol*. May 2010;8(5):340-9. doi:10.1038/nrmicro2313

36. Nogueira F, Sharghi S, Kuchler K, Lion T. Pathogenetic Impact of Bacterial-Fungal Interactions. *Microorganisms*. Oct 16 2019;7(10)doi:10.3390/microorganisms7100459

37. Mayer FL, Kronstad JW. The Spectrum of Interactions between. *J Fungi (Basel)*. Apr 12 2019;5(2)doi:10.3390/jof5020031

38. May RC, Stone NR, Wiesner DL, Bicanic T, Nielsen K. Cryptococcus: from environmental saprophyte to global pathogen. Research Support, N.I.H., Extramural
Research Support, Non-U.S. Gov't
Review. *Nat Rev Microbiol*. Feb 2016;14(2):106-17. doi:10.1038/nrmicro.2015.6

39. Perfect JR. Cryptococcosis: a model for the understanding of infectious diseases. *J Clin Invest*. May 1 2014;124(5):1893-5. doi:10.1172/jci75241

40. Rajasingham R, Smith RM, Park BJ, et al. Global burden of disease of HIV-associated cryptococcal meningitis: an updated analysis. *Lancet Infect Dis*. May 05 2017;doi:10.1016/S1473-3099(17)30243-8

41. Fernandes KE, Brockway A, Haverkamp M, et al. Phenotypic Variability Correlates with Clinical Outcome in Cryptococcus Isolates Obtained from Botswanan HIV/AIDS Patients. *mBio*. 10 23 2018;9(5)doi:10.1128/mBio.02016-18

42. Cherian J, Atmar RL, Gopinath SP. Shunting in cryptococcal meningitis. *J Neurosurg*. Jul 2016;125(1):177-86. doi:10.3171/2015.4.JNS15255

43. Liu L, Zhang R, Tang Y, Lu H. The use of ventriculoperitoneal shunts for uncontrollable intracranial hypertension in patients with HIV-associated cryptococcal meningitis with or without hydrocephalus. *Biosci Trends*. Dec 2014;8(6):327-32. doi:10.5582/bst.2014.01070

44. Walsh TJ, Schlegel R, Moody MM, Costerton JW, Salcman M. Ventriculoatrial shunt infection due to Cryptococcus neoformans: an ultrastructural and quantitative microbiological study. *Neurosurgery*. Mar 1986;18(3):373-5.

45. Braun DK, Janssen DA, Marcus JR, Kauffman CA. Cryptococcal infection of a prosthetic dialysis fistula. *Am J Kidney Dis*. Nov 1994;24(5):864-7.

46. Banerjee U, Gupta K, Venugopal P. A case of prosthetic valve endocarditis caused by Cryptococcus neoformans var. neoformans. *J Med Vet Mycol*. 1997 Mar-Apr 1997;35(2):139-41.

47. Shah NB, Shoham S, Nayak S. Cryptococcus neoformans prosthetic joint infection: case report and review of the literature. *Mycopathologia*. Apr 2015;179(3-4):275-8. doi:10.1007/s11046-014-9847-0

48. Johannsson B, Callaghan JJ. Prosthetic hip infection due to Cryptococcus neoformans: case report. *Diagn Microbiol Infect Dis*. May 2009;64(1):76-9. doi:10.1016/j.diagmicrobio.2009.01.005

49. Aslanyan L, Sanchez D, Valdebenito S, Eugenin E, Ramos R, Martinez L. The Crucial Role of Biofilms in Cryptococcus neoformans Survival within Macrophages and Colonization of the Central Nervous System. In: Sanchez D, editor. Journal of Fungi2017. p. 10.

50. Tuon FF, Morales HM, Penteado-Filho SR, da-Silva MM, Quadros I, El Hamoui A. Central venous catheter-related bloodstream infection and Cryptococcus neoformans. *Braz J Infect Dis*. Aug 2009;13(4):317-8.

51. Katsiari M, Laskou M, Provatas I, et al. A Fatal Case of Misdiagnosed Cryptococcal Epididymo-Orchitis and Leg Cellulitis in a HIV-Negative Patient. Case Reports. *4*. 2013-01-08 2013;doi:https://www.journalmc.org/index.php/JMC/article/view/1119

52. John MA, Coovadia Y. Meningitis due to a combined infection with Cryptococcus neoformans and Streptococcus pneumoniae in an AIDS patient. *J Infect*. Mar 1998;36(2):231-2.

53. Muranda AZ, Greeff L, Sathekge MM, Lengano T, Karusseit VOL. Cryptococcoma of a transplanted kidney in a patient presenting with recurrent

urinary tract infection: a case report. *BMC Nephrol*. Apr 23 2018;19(1):94. doi:10.1186/s12882-018-0891-8

54. Saleem F, Fasih N, Zafar A. Cryptococcus neoformans and Streptococcus pneumoniae co-infection in post-traumatic meningitis in a patient with unknown HIV status. *J Pak Med Assoc*. Oct 2015;65(10):1122-4.

55. Rodríguez Amor D, Dal Bello M. Bottom-Up Approaches to Synthetic Cooperation in Microbial Communities. *Life (Basel)*. Feb 26 2019;9(1)doi:10.3390/life9010022

56. Ghoul M, Mitri S. The Ecology and Evolution of Microbial Competition. *Trends Microbiol*. Oct 2016;24(10):833-845. doi:10.1016/j.tim.2016.06.011

57. Bielska E, Sisquella MA, Aldeieg M, Birch C, O'Donoghue EJ, May RC. Pathogen-derived extracellular vesicles mediate virulence in the fatal human pathogen Cryptococcus gattii. *Nat Commun*. 04 19 2018;9(1):1556. doi:10.1038/s41467-018-03991-6

58. Albuquerque P, Nicola AM, Nieves E, et al. Quorum sensing-mediated, cell density-dependent regulation of growth and virulence in Cryptococcus neoformans. *MBio*. Dec 2013;5(1):e00986-13. doi:10.1128/mBio.00986-13

59. Cordero RJ, Liedke SC, de S Araújo GR, et al. Enhanced virulence of Histoplasma capsulatum through transfer and surface incorporation of glycans from Cryptococcus neoformans during co-infection. *Sci Rep*. Feb 24 2016;6:21765. doi:10.1038/srep21765

60. Wang L, Tian X, Gyawali R, Lin X. Fungal adhesion protein guides community behaviors and autoinduction in a paracrine manner. *Proc Natl Acad Sci U S A*. Jul 2013;110(28):11571-6. doi:10.1073/pnas.1308173110

61. Hommel B, Mukaremera L, Cordero RJB, et al. Titan cells formation in Cryptococcus neoformans is finely tuned by environmental conditions and modulated by positive and negative genetic regulators. *PLoS Pathog*. May 2018;14(5):e1006982. doi:10.1371/journal.ppat.1006982

62. Dambuza IM, Drake T, Chapuis A, et al. The Cryptococcus neoformans Titan cell is an inducible and regulated morphotype underlying pathogenesis. *PLoS Pathog*. May 2018;14(5):e1006978. doi:10.1371/journal.ppat.1006978

63. Ratzke C, Barrere J, Gore J. Strength of species interactions determines biodiversity and stability in microbial communities. *Nat Ecol Evol*. 03 2020;4(3):376-383. doi:10.1038/s41559-020-1099-4

64. Rao C, Coyte KZ, Bainter W, Geha RS, Martin CR, Rakoff-Nahoum S. Multi-kingdom ecological drivers of microbiota assembly in preterm infants. *Nature*. Mar 2021;591(7851):633-638. doi:10.1038/s41586-021-03241-8

65. Gonze D, Lahti L, Raes J, Faust K. Multi-stability and the origin of microbial community types. *ISME J*. 10 2017;11(10):2159-2166. doi:10.1038/ismej.2017.60

66. Khazaei T, Williams RL, Bogatyrev SR, Doyle JC, Henry CS, Ismagilov RF. Metabolic multistability and hysteresis in a model aerobe-anaerobe microbiome community. *Sci Adv*. Aug 2020;6(33):eaba0353. doi:10.1126/sciadv.aba0353

67. Lahti L, Salojärvi J, Salonen A, Scheffer M, de Vos WM. Tipping elements in the human intestinal ecosystem. *Nat Commun*. 07 08 2014;5:4344. doi:10.1038/ncomms5344

# 7 CURRICULUM VITAE

Resumido

Av. Bento Gonçalves, 9500. Porto Alegre, RS
Setor 4, Prédio 43421, Lab. 220
+55 51 3308.6074
lopeswlm@gmail.com

## LOPES, W.

William Lopes

### FORMAÇÃO

2017 — Presente UNIVERSIDADE FEDERAL DO RIO GRANDE DO SUL
Doutorando em Biologia Celular e Molecular
Porto Alegre, RS, Brasil

2019 — 2020 MASSACHUSETTS INSTITUTE OF TECHNOLOGY (GORE LAB)
Estudante visitante
Cambridge, MA, Estados Unidos

2010 — 2017 UNIVERSIDADE FEDERAL DO RIO GRANDE DO SUL
Bacharel em Farmácia
Porto Alegre, RS, Brasil

2005 — 2009 FUNDAÇÃO ESCOLA TÉCNICA LIBERATO SALZANO VIEIRA DA CUNHA
Técnico em Química
Novo Hamburgo, RS, Brasil

### PRÊMIOS E DISTINÇÕES

2020 IX PRÊMIO FOTOGRAFIA, CIÊNCIA & ARTE — Imagem "Beleza que mata"
Conselho Nacional de Desenvolvimento Científico e Tecnológico (CNPq)

2019 PUBLICAÇÃO EM CAPA DE PERIÓDICO
Clinical Microbiology and Infection Vol. 25 Iss. 2

2019 VENCEDOR NO 4° CONCURSO CIÊNCIA POR IMAGENS
Categoria Microscopia Eletrônica de Varredura
Centro de Microscopia e Microanálise da UFRGS

2018 VENCEDOR NO 3° CONCURSO CIÊNCIA POR IMAGENS

Categorias Microscopia Eletrônica de Varredura e Microscopia Eletrônica de Transmissão
Centro de Microscopia e Microanálise da UFRGS

2018 PUBLICAÇÃO EM CAPA DE PERIÓDICO
Clinical Microbiology and Infection Vol. 24 Iss. 10

2017 PUBLICAÇÃO EM CAPA DE PERIÓDICO
Clinical Microbiology and Infection Vol. 23 Iss. 12

2016 VENCEDOR NO 2° CONCURSO CIÊNCIA POR IMAGENS
Categorias Microscopia Eletrônica de Varredura e Microscopia Eletrônica de Transmissão
Centro de Microscopia e Microanálise da UFRGS

2016 PRIMEIRO LUGAR — XXXVII CONCURSO ACADÊMICO DE PESQUISA CIENTÍFICA
Faculdade de Farmácia da UFRGS

2011 CERTIFICATE OF APPRECIATION
Simultaneous Interpreter of Portuguese
Society for Science and the Public and Intel ISEF, San Diego, USA

2010 INTERNATIONAL PRIZE
European Union Contest for Young Scientists
Directorate General for Research, European Comission, Lisbon, PT

2010 GOOGLE SPECIAL AWARD
Intel International Science & Engineering Fair, San Jose, USA

2010 NATIONAL COLLEGIATE INVENTORS AND INNOVATORS ALLIANCE PRIZE
The Lemelson Foundation, San Jose, USA

2010 PRÊMIO JOVEM CIENTISTA
Assembléia Legislativa do Estado do Rio Grande do Sul, Porto alegre, Brasil.

## EXPERIÊNCIA PROFISSIONAL

2012 — 2017 ASSOCIAÇÃO BRASILEIRA DE INCENTIVO À CIÊNCIA
Diretor — Co-Fundador de ONG
São Paulo, SP, Brasil
Líder de grupo em um projeto nacional para promoção da educação científica entre jovens no Brasil, alcançando mais de 10 mil pessoas.

2009 HOSPITAL REGINA, LABORATÓRIO DE MICROBIOLOGIA
Porto Alegre, RS, Brasil

## ATIVIDADE EDITORIAL

2021 — Presente Revisor em *mSystems*
American Society for Microbiology Publications

2021 — Presente Revisor em *Scientific Reports*
Nature Research

2019 — Presente Revisor em *Science of the Total Environment*
Elsevier

2018 — Presente Revisor em *Clinical Microbiology and Infection*
Elsevier

## PARTICIPAÇÃO EM BANCAS

2019 BANCA DE RODRIGO SARDAGNA
Graduação em Engenharia de Bioprocessos e Biotecnologia
"Preparação de biocatalisador por células íntegras de *Rhizopus oryzae* e nanopartículas magnéticas para a síntese de ésteres de aroma e sabor."
Universidade Estadual do Rio Grande do Sul, Porto Alegre, RS.

2018 BANCA DE PAOLA GUASSELLI
Graduação em Engenharia de Bioprocessos e Biotecnologia
"Remoção de ácido acetilsalicílico em soluções aquosas empregando biofilmes microbianos desenvolvidos em diferentes suportes."
Universidade Estadual do Rio Grande do Sul, Porto Alegre, RS.

## CONVITE PARA PALESTRA

2021 28º CONGRESSO DA SOCIEDADE BRASILEIRA DE MICROSCOPIA E MICROANÁLISE
Automated identification of cell morphotypes in Scanning Electron Microscopy
*On-line*

## PUBLICAÇÕES

Desai, G., Koroneos, N., Hamed, M., Jain, N., Cordero, R., Rodriguez, C., **Lopes, W.,** Nosanchuk, J., Vainstein, M., Martinez, L. (2021). Thermosensitivity and reduced expression of Heat-shock protein 60 determine the cutaneous tropism exhibited by *Cryptococcus deneoformans* strains. *In revision*

Silva, N. M., Gentz, C. B., Reginatto, P., Fernandes, T., Kaminski, T., **Lopes, W.**, Quatrin, P. M., Vainstein, M. H., Abegg, M. A., Lopes, M. S., Fuentefria, A. M., & de Andrade, S. F. (2021). 8-Hydroxyquinoline 1,2,3-triazole derivatives with promising and selective antifungal activity. *Medical mycology*, *59*(5), 431–440.

Machado, G., Pippi, B., Berlitz, S., Diedrich, D., Defferrari, D., **Lopes, W.**, Gnoatto, S., Kulkamp-Guerreiro, I. C., Vainstein, M. H., Jean, M., Van de Weghe, P., de Andrade, S. F., & Fuentefria, A. M. (2021). *Ex vivo* potential of a quinoline-derivative nail lacquer as a new alternative for dermatophytic onychomycosis treatment. *Journal of medical microbiology*, *70*(3).

Ehrhardt, A., Mandelli, J., Bérgamo, V., **Lopes, W.**, Donato, R. K., Zanette, R. A., & Fuentefria, A. M. (2021). Glass ionomer cement modified by a imidazolium salt: adding antifungal properties to a biomaterial. *Brazilian journal of microbiology* (in press).

Haleva, L.*, **Lopes, W.***, Barcellos, V. A., Schrank, A., & Vainstein, M. H. (2020). The contest of microbial pigeon neighbors: Interspecies competition between Serratia marcescens and the human pathogen *Cryptococcus neoformans*. *Fungal biology*, *124*(7), 629–638.

Pippi, B., Joaquim, A. R., **Lopes, W.**, Machado, G., Bergamo, V. Z., Giuliani, L. M., Abegg, M. A., Cruz, L., Vainstein, M. H., Fuentefria, A. M., & de Andrade, S. F. (2020). 8-Hydroxyquinoline-5-sulfonamides are promising antifungal candidates for the topical treatment of dermatomycosis. *Journal of applied microbiology*, *128*(4), 1038–1049.

**Lopes, W.***, Cruz, G.*, Rodrigues, M. L., Vainstein, M. H., Kmetzsch, L., Staats, C. C., Vainstein, M. H., & Schrank, A. (2020). Scanning electron microscopy and machine learning reveal heterogeneity in capsular morphotypes of the human pathogen *Cryptococcus* spp. *Scientific reports*, *10*(1), 2362.

Dalla Lana, D. F., Neiva Lavorato, S., Minussi Giuliani, L., Cruz, L., **Lopes, W.**, Henning Vainstein, M., Camargo Fontana, I., Rigon Zimmer, A., de Araújo Freitas, M., de Andrade, S. F., José Alves, R., & Meneghello Fuentefria, A. (2020). Discovery of a novel and selective fungicide that targets fungal cell wall to treat dermatomycoses: 1,3-bis(3,4-dichlorophenoxy)propan-2-aminium chloride. *Mycoses*, *63*(2), 197–211.

Bazana, L. C. G., Carvalho, Â. R., Silveira, G. P., Oliveira, L. F. S., Teixeira, M. L., **Lopes, W.**, Vainstein, M. H., Barbosa, F. A. R., Russo, T. V. C., Sá, M. M., Canto, R. F. S. & Fuentefria, A. M. (2020). Allylic Selenocyanates as Antifungal Agents Against Pathogenic *Candida* Species. *ChemistrySelect*, *5*, 10495.

Krummenauer, M. E.*, **Lopes, W.***, Garcia, A., Schrank, A., Gnoatto, S., Kawano, D. F., & Vainstein, M. H. (2019). A Highly Active Triterpene Derivative Capable ׀of Biofilm Damage to Control *Cryptococcus* spp. *Biomolecules*, *9*(12), 831.

Dalla Lana, D. F., Batista, B. G., da Rosa Machado, G., Teixeira, M. L., de Oliveira, L., Machado, M. M., de Andrade, S. F., **Lopes, W.**, Vainstein, M. H., de Abreu Lima, A. P., Pandolfi, E., Silva, E. E., Fuentefria, A. M., & Silveira, G. P. (2019). Design, synthesis, and evaluation of novel 2-substituted 1,4-benzenediol library as antimicrobial agents against clinically relevant pathogens. *Saudi pharmaceutical journal*, *27*(8), 1064–1074.

Pereira, E., Napp, A. P., Allebrandt, S., Barbosa, R., Reuwsaat, J., **Lopes, W.**, Kmetzsch, L., Staats, C. C., Schrank, A., Dallegrave, A., Peralba, M. C., Passaglia, L. M. P., Bento, F. M., & Vainstein, M. H. (2019). Biodegradation of aliphatic and polycyclic aromatic hydrocarbons in seawater by autochthonous microorganisms. *International Biodeterioration & Biodegradation. 145, 104789.*

**Lopes, W.**, Vainstein, M. H., & Schrank, A. (2019). Revealing colonial characteristics of Candida tropicalis by high-resolution scanning electron microscopy. *Clinical microbiology and infection: the official publication of the European Society of Clinical Microbiology and Infectious Diseases*, *25*(2), 188–189.

Quatrin, P. M, Dalla Lana, D. F., Bazana, L. C. G., Oliveira, L. F. S., Teixeira, M. L., Silva, E. E., **Lopes, W.**, Canto, R. F. S., Silveira, G. P., & Fuentefria, A. M. (2019) 3-Selenocyanate-indoles as new agents for the treatment of superficial and mucocutaneous infections. *New Journal of Chemistry 43 (2),* 926-933.

Pippi, B., **Lopes, W.**, Reginatto, P., Silva, F., Joaquim, A. R., Alves, R. J., Silveira, G. P., Vainstein, M. H., Andrade, S. F., & Fuentefria, A. M. (2019). New insights into the mechanism of antifungal action of 8-hydroxyquinolines. *Saudi pharmaceutical journal*, *27*(1), 41–48.

**Lopes, W.**, Reuwsaat, J., Henning Vainstein, M., Staats, C., Kmetzsch, L., Schrank, A., & Henning Vainstein, M. (2018). The duality of a deadly pathogen. *Clinical microbiology and infection: the official publication of the European Society of Clinical Microbiology and Infectious Diseases*, *24*(10), 1064–1065.

Danielli, L. J., Pippi, B., Duarte, J. A., Maciel, A. J., **Lopes, W.**, Machado, M. M., Oliveira, L., Vainstein, M. H., Teixeira, M. L., Bordignon, S., Fuentefria, A. M., & Apel, M. A. (2018). Antifungal mechanism of action of *Schinus lentiscifolius* Marchand essential oil and its synergistic effect in vitro with terbinafine and ciclopirox against dermatophytes. *The Journal of pharmacy and pharmacology*, *70*(9), 1216–1227.

Reuwsaat, J., Motta, H., Garcia, A., Vasconcelos, C. B., Marques, B. M., Oliveira, N. K., Rodrigues, J., Ferrareze, P., Frases, S., **Lopes, W.**, Barcellos, V. A., Squizani, E. D., Horta, J. A., Schrank, A., Rodrigues, M. L., Staats, C. C., Vainstein, M. H., & Kmetzsch, L. (2018). A Predicted Mannoprotein Participates in *Cryptococcus gattii* Capsular Structure. *mSphere*, *3*(2), e00023-18.

Squizani, E. D., Oliveira, N. K., Reuwsaat, J., Marques, B. M., **Lopes, W.**, Gerber, A. L., de Vasconcelos, A., Lev, S., Djordjevic, J. T., Schrank, A., Vainstein, M. H., Staats, C. C., & Kmetzsch, L. (2018). Cryptococcal dissemination to the central nervous system requires the vacuolar calcium transporter Pmc1. *Cellular microbiology*, *20*(2).

Dalla Lana, D. F., Giuliani, L. M., Reolon, J. B., **Lopes, W.**, Vainstein, M. H., Danielli, L. J., Bergamo, V. Z., Pippi, B., Apel, M. A., Teixeira, M. L., Oliveira, L. F. S., Machado, M. M., Andrade,
S. F., Sá, M. M., Ferreira, M., Munaretto, L. S., Cruz, L., Silveira, G. P., Elayne, E. & Fuentefria, A.M. (2018). Nanoemulsion improves the antifungal activity of allylic thiocyanates against yeasts and filamentous pathogenic fungi. *ChemistrySelect, 3, 11663.*

**Lopes, W.***, Vainstein, M. H.*, De Sousa Araujo, G. R., Frases, S., Staats, C. C., de Almeida, R., Schrank, A., Kmetzsch, L., & Vainstein, M. H. (2017). Geometrical Distribution of *Cryptococcus neoformans* Mediates Flower-Like Biofilm Development. *Frontiers in microbiology*, *8*, 2534.

Batista, B. G., Lana, D. F. D., Silveira, G. P., Sá, M. M., Ferreira, M., Russo, T. V. C., Canto, R. F. S., Barbosa, F. A. R., Braga, A. L., Kaminski, T. F. A., Oliveira, L. F. S., Machado, M. M., **Lopes, W.**, Vainstein, M. H., Teixeira, M. L., Andrade, S. F., Fuentefria, A. M. (2017). Allylic Selenocyanates as New Agents to Combat *Fusarium* Species Involved with Human Infections. *ChemistrySelect*, *2*, 11926.

Danielli, L. J., **Lopes, W.**, Vainstein, M. H., Fuentefria, A. M., & Apel, M. A. (2017). Biofilm formation by Microsporum canis. *Clinical microbiology and infection: the*

*official publication of the European Society of Clinical Microbiology and Infectious Diseases*, *23*(12), 941–942.

Lando, G. A., Marconatto, L., Kessler, F., **Lopes, W.**, Schrank, A., Vainstein, M. H., & Weibel, D. E. (2017). UV-Surface Treatment of Fungal Resistant Polyether Polyurethane Film-Induced Growth of Entomopathogenic Fungi. *International journal of molecular sciences*, *18*(7), 1536.

Joffe, L. S., Schneider, R., **Lopes, W.**, Azevedo, R., Staats, C. C., Kmetzsch, L., Schrank, A., Del Poeta, M., Vainstein, M. H., & Rodrigues, M. L. (2017). The Anti-helminthic Compound Mebendazole Has Multiple Antifungal Effects against *Cryptococcus neoformans*. *Frontiers in microbiology*, *8*, 535.

Bergamo, V. Z., Donato, R. K., Nemitz, M. C., Acasigua, G. A., Selukar, B. S., **Lopes, W.**, Dalla Lana, D. F., Teixeira, M. L., Teixeira, H. F., Schrekker, H. S., & Fuentefria, A. M. (2016). Assessing an imidazolium salt's performance as antifungal agent on a mouthwash formulation. *Journal of applied microbiology*, *121*(6), 1558–1567.

de Souza, I. O., Schrekker, C. M., **Lopes, W.**, Orru, R. V., Hranjec, M., Perin, N., Machado, M., Oliveira, L. F., Donato, R. K., Stefani, V., Fuentefria, A. M., & Schrekker, H. S. (2016). Bifunctional fluorescent benzimidazo[1,2-$\alpha$]quinolines for Candida spp. biofilm detection and biocidal activity. *Journal of photochemistry and photobiology. B, Biology*, *163*, 319–326.

Schrekker, C. M., Sokolovicz, Y. C., Raucci, M. G., Selukar, B. S., Klitzke, J. S., **Lopes, W.**, Leal, C. A., de Souza, I. O., Galland, G. B., Dos Santos, J. H., Mauler, R. S., Kol, M., Dagorne, S., Ambrosio, L., Teixeira, M. L., Morais, J., Landers, R., Fuentefria, A. M., & Schrekker, H. S. (2016). Multitask Imidazolium Salt Additives for Innovative Poly(l-lactide) Biomaterials: Morphology Control, Candida spp. Biofilm Inhibition, Human Mesenchymal Stem Cell Biocompatibility, and Skin Tolerance. *ACS applied materials & interfaces*, *8*(33), 21163–21176.

*primeira autoria compartilhada

## PRODUÇÃO CIENTÍFICA – ARTÍSTICA

Entre 2018 e 2019, destacam-se premiações em concursos promovidos pela ArtBio nos projetos "Mostra de Arte Científica Brasileira" e "Ciência e Arte Para Todos". As imagens premiadas fizeram parte de exposições na cidade do Rio de

Janeiro, no Museu da Maré, Museu do Amanhã, Aeroporto Internacional Tom Jobim, Instituto Butantan e rede pública de escolas do Rio de Janeiro. Em paralelo, foram publicados dois livros com distribuição gratuita com o objetivo de potencializar o debate científico na sociedade através da conexão entre duas linguagens: ciência e arte. As imagens também tiveram alcance internacional através de matéria jornalística publicada na "BBC News".

Adicionalmente, foi criada a exposição "Beleza que mata": Composta por imagens de microscopia eletrônica dos patógenos humanos *Cryptococcus gattii* e *Cryptococcus neoformans*. A exibição ocorreu na reitoria e no instituto de física da UFRGS, além da Faculdade de Farmácia da USP.